The Development and Validation of a First Generation X-Ray Scatter Computed Tomography Algorithm for the Reconstruction of Electron Density Breast Images Using Monte Carlo Simulation

by

Jorge Edmundo Alpuche Aviles

A Thesis submitted to the Faculty of Graduate Studies of

The University of Manitoba

in partial fulfillment of the requirements of the degree of

DOCTOR OF PHILOSOPY

Department of Physics and Astronomy

University of Manitoba

Winnipeg, Manitoba

ABSTRACT

Breast CT is a promising modality whose inherent scatter could be used to reconstruct electron density (ρ_e) images. This has led us to investigate the benefits of reconstructing linear attenuation coefficient (μ) and ρ_e images of the breast. First generation CT provides a cost-effective and simple approach to reconstruct ρ_e images in a laboratory but is limited by the anisotropic probability of scatter, attenuation, noise and contaminating scatter (coherent and multiple scatter).

These issues were investigated using Monte Carlo (MC) simulations of a 1st generation breast scatter enhanced CT (B-SECT) system. A reconstruction algorithm was developed for the B-SECT system and is based on a ring of detectors which eliminates the scatter dependence on the relative position of the scattering centre. The algorithm incorporates an attenuation correction based on the μ image and was tested against analytical and MC simulations. MC simulations were also used to quantify the dose per scan.

The ring measures a fraction of the total single incoherent scatter which is proportional to ray integrals of ρ_e and can be quantified even when electron binding is non negligible. The algorithm typically reconstructs accurate ρ_e images using a single correction for attenuation but has the capability for multiple iterations if required. MC simulations show that the dose coefficients are similar to those of cone beam breast CT. Coherent and multiple scatter can not be directly related to ρ_e and lead to capping artifacts and overestimated ρ_e by a factor greater than 2. This issue can be addressed using empirical corrections based on the radiological path of the incident beam and result

in ρ_e images of breast soft tissue with 1% accuracy, 3% precision and a mean glandular dose of 4 mGy for a 3D scan. The reconstructed ρ_e image was more accurate than the ρ_e estimate derived from the μ image. An alternative correction based on the thickness of breast traversed by the beam provides an enhanced contrast image reflecting the breast scatter properties. These results demonstrate the feasibility of detecting small ρ_e changes in the intact breast and shows that further experimental evaluation of this technique is warranted.

ACKNOWLEDGMENTS

First, I would like to thank my supervisor Dr. Stephen Pistorius for taking me as his student. This dissertation would not have been possible without his guidance, input, patience, dedication and encouragement. It is his vision that stimulated the development of this exciting project.

I would like to thank the members of my committee for guiding the development of the thesis. The committee included Dr. Stephen Pistorius, Dr. Idris A. Elbakri, Dr. Jason Fiege, Dr. Sherif Sherif and Dr. Richard Gordon.

I would also like to thank the entire Division of Medical Physics, particularly, the members of the Imaging group: Dr. Daniel Rickey, Dr. Harry Ingleby and Dr. Congwu Cui. Thanks to the summer students that worked in this project which include Eric Recksiedler, Bashir Ahmad and Paul Oramasionwu.

I am grateful to my fellow students in Medical Physics. Through these years we have shared many experiences which I will always treasure. I look forwards for many years of collaboration with my colleagues Eric Van Uytven, Peter Potrebko, David Niven, Krista Chytyk, Niranjan Venugopal, Jim Wu, Jenna King, Tamar Chighvinadze, Ganiyu Asuni, Fazal Ur-Rehman, Nava Paudel, Troy Teo, Mike Hebb, Heather Champion, Peter McCowan, Manjinder Chahal and Hongyan Sun.

I would like to thank my family that even though they were (geographically) away they never felt far. Thanks also to my many friends with whom I have shared wonderful years during my studies. Thanks to Dafnne Zamorano for her unconditional support during good and bad times. Finally, I would like to acknowledge the sources of funding that I had over the years. This project was funded by the Manitoba Health

Research Council, CancerCare Manitoba Foundation, the University of Manitoba Graduate Fellowship and the Mexican Ministry of Public Education (known as SEP in Spanish).

To all my family

LIST OF ABREVIATIONS

AN	Analytical
ACF	Attenuation correction factor
B-SECT	Breast scatter enhanced CT
BCT	Breast CT
BS	Breast size
CNR	Contrast-to-noise ratio
CS	Coherent scatter
CSCT	Coherent scatter CT
CT	Computed Tomography
FBP	Filtered back projection
FOV	Field of view
FXCT	Fluorescent x-ray CT
HU	Hounsfield unit
IAM	Independent atomic model
IDC	Infiltrating duct carcioma
ISCT	Incoherent scatter CT
KN	Klein-Nishina
MC	Monte Carlo
MCC	Microcalcification
MGD	Mean glandular dose

MRI	Magnetic Resonance Imaging
MRSD	Mean relative square deviation
MS	Multiple scatter
PET	Positron emission tomography
ROI	Region of interest
SDD	Source to detector distance
SICR	Scatter increase correction ratio
SID	Source to isocentre distance
SNR	Signal-to-noise ratio
SPECT	Single photon emission computed tomography
US	Ultrasound

LIST OF PHYSICAL CONSTANTS

h	Planck's constant	6.626×10^{-34} J s
c	Speed of light in vacuum	2.998×10^{8} m s^{-1}
m_0	Electron rest mass	9.109×10^{-31} kg
r_0	Classical electron radius	2.818×10^{-15} m
N_A	Avogadro constant	6.022×10^{23} mol^{-1}

LIST OF SYMBOLS

a	Area of a scatter detector
$F(q,Z)$	Atomic form factor

Z	Atomic number
A	Atomic weight
θ	CT projection angle
δ	Detector central angle (see Figure 4.2)
$d\sigma / d\Omega$	Differential cross section
$\overline{Z}$	Effective atomic number
ρ_e	Electron density
E	Energy
E_0	Energy of the incident beam
E_S	Energy of the scattered photon
f_x	Fraction by weight of a material x to a mixture of materials
w_i	Fraction by weight of element i to a mixture of elements
F	Fraction of single incoherently scattered photons from an infinitesimally small point at a given location measured by the ring
Φ_0	Incident fluence
$S(q,Z)$	Incoherent scatter function
$d_e\sigma_{KN} / d\Omega$	KN Differential cross section per electron
${}_e\sigma_{KN}$	KN total cross section per electron
μ	Linear attenuation coefficient
μ/ρ	Mass attenuation coefficient
μ_{en}/ρ	Mass energy absorption coefficient
L	Material thickness

$\overline{F}$	Mean value of F over the field of view
q	Momentum transfer
n_e	Number of electrons per unit area
N_0	Number of incident photons
N_{SI}	Number of single incoherently scattered photons measured by a detector
ρ	Physical density
μL	Radiological path
φ	Scattering angle
$\Delta\Omega$	Solid angle
${}_a\sigma$	Total cross section per atom
$N_{Tot,\,Incoh}$	Total number of photons undergoing single incoherent scatter

TABLE OF CONTENTS

LIST OF FIGURES

LIST OF TABLES

1. Rationale

Cancer is a family of diseases of the cell and is the major cause of death in Canada [1]. Groups of malfunctioning cells can organize into clusters called tumors which can be benign or malignant, with the later being associated with increased potential risk to life. Tumors can spread to other parts of the body and are typically named according to the location where the tumor originated from. Breast Cancer is the most common type of cancer among Canadian women (excluding non-melanoma skin cancer) [2]. It is expected that one in every nine women will develop breast cancer during her lifetime. According to the Canadian Cancer Society about 23,300 women will be diagnosed with this disease in 2010 and 5,300 will die from it.

The burden of breast cancer has lead to the implementation of large, population based screening programs. The aim of these programs is to detect cancer at an early stage. Screening programs that detect malignancies at an early stage improve survival and provide more treatment options. Some screening programs have also been attributed with the partial reduction in breast cancer mortality [3-5]. X-ray mammography is the most common screening technique and detected about 6,900 cancers in Canada between 2003 and 2004 [6]. Despite the benefits of mammography, its limited sensitivity (the ability of a system to detect the presence of disease) and specificity (the ability of the system to detect the absence of disease) lead to both missed cancers and false positives. False positives resulted in unnecessary follow up, cost to the health system and stress for more than 3,500 women in Manitoba between 2006 and 2007 [3].

The current limitations of x-ray mammography have lead to the development of alternative modalities but to date their role remains limited to specific applications [7]. Among these modalities, breast CT (BCT) and breast tomosynthesis have shown potential to replace planar mammography [8]. These techniques take multiple x-ray projections in order to reconstruct 3D images of the breast. Specifically, breast tomosynthesis consist of limited angle BCT and hence has limited accuracy compared with BCT.

BCT is capable of reconstructing 3D images of the breast using doses similar to those used in mammography [9]. The reconstructed image depicts a map of the linear attenuation coefficient (μ) which has been shown to be characteristic for different breast tissue [10]. This μ image can potentially be used for quantitative imaging, reducing subjective diagnosis and improving tissue characterization. A clinical study by Lindfors *et al*. [11] has shown that overall BCT performs equivalently to mammography in the detection of breast lesions. More specifically, Lindfors *et al*. found that BCT outperformed mammography in the detection of masses and was more comfortable for the patient. Traditional mammography outperformed BCT in the visualization of microcalcifications (MCC) which can be an important cancer indicator [12, 13]. An additional limitation of BCT is that the μ is insufficient to completely characterize a material. This is because the μ is inherently dependent, even for a fixed energy, on the atomic number (Z) and electron density (ρ_e). Hence, materials with different ρ_e and Z can still combine to yield the same value of μ. Recently, Chen *et al.* found that the μ may not be able to differentiate between fibrous tissue and tumors [14] even for energies

where the μ has large contrast. The current limitations of BCT must be overcome before it can be used as an alternative to mammography.

The particular introduction of either ρ_e or Z holds great promise in BCT. Given that the μ is dependent on ρ_e and Z, any of these parameters will reduce the uncertainty in material characterization and complement the μ image. Electron density images can be reconstructed by measuring incoherently scattered photons [15-35]. This makes scatter radiation a source of latent information that can potentially improve medical diagnosis. The ρ_e images may show information otherwise indistinguishable in a μ image [36-38]. In addition, Ryan *et al*. have shown that the difference in ρ_e between adipose tissue and malignancy is statistically significant [39]. Ryan *et al*. also found statistically significant differences comparing adipose tissue with fibrocystic change, malignancy with fibroradenoma and fibroadenoma with fibrocystic change. Al-Bahri *et al.* measured the ρ_e of adipose, tumor and glandular tissue samples [40]. Their results indicate that the difference in ρ_e between tumor and adipose tissue is of 3% while that between tumor and glandular tissue is of 2%. Ryan *et al*. re-measured the ρ_e of breast tissue since the ones from Al-Bahri *et al*. had a wide range of values even for the same tissue [39]. The results from Ryan *et al.* show that the malignant tissue has a difference in ρ_e of 8% with adipose tissue, 6% with fibroadenoma and 3% with fibrocystic change. A follow-up paper showed that using ρ_e, in conjunction with the atomic form factor, can improve the specificity of breast tissue diagnosis [41]. More recently, Antoniassi *et al.* designed a mono-energetic x-ray system to measure the ρ_e of breast tissue [42]. Their results indicate differences between the ρ_e of malignancy and adipose tissue of 10%, malignancy and fibrous tissue of 2% and malignancy and fibroadenoma of 4%. Simulation studies from

Van Uytven *et al.* [16] also show that *in vivo* ρ_e imaging has the potential to detect MCC lesions, an area that remains one of the main challenges in BCT. The scatter levels of BCT are such [43, 44] that, along with the potential for improved diagnosis, makes BCT a perfect candidate for the incorporation of ρ_e images.

There exists enough motivation to incorporate ρ_e images into BCT but the clinical benefit of such incorporation remains unknown. For this reason a breast scatter enhanced CT (B-SECT) system has been designed (Figure 1.1). The purpose of the B-SECT system is to evaluate the benefits, if any, of simultaneously reconstructing ρ_e and μ images of the breast *in vivo*. The experiments that will be conducted with the B-SECT will demonstrate whether ρ_e imaging of the breast has any role to play and hence, whether it is worth pursuing its clinical implementation. B-SECT will be used to reconstruct images of breast phantoms, tissue samples, mastectomies and, potentially, volunteers. To achieve this goal, this thesis developed a reconstruction algorithm suitable for *in vivo* ρ_e images of the breast using the B-SECT system. This was pursued while limiting the dose to that of a two view mammography study to be consistent with the development of BCT. The ρ_e image should allow discrimination between malignant and non malignant lesions. As mentioned above, this difference can be as small as 2% and sets the desirable accuracy and precision of the ρ_e image. These conditions set the frame for the hypothesis of this thesis which can be summarized as follows

The scattered x-rays of the B-SECT system can be used to reconstruct ρ_e images using the algorithm presented in this thesis with an accuracy of 1%, precision of 1% and using a dose comparable to mammographic studies.

The following two chapters of this thesis consist of bibliographic research and the necessary physics background. Chapter 4 introduces the proposed algorithm and tests its performance by reconstructing images out of single Klein-Nishina (KN) scatter sinograms. The algorithm is novel in its ability to reconstruct ρ_e images of objects with breast sizes using 1st generation incoherent scatter CT. Chapter 5 presents the results when the simplifying assumptions of Chapter 4 are removed in a comprehensive simulation of the B-SECT system using the Monte Carlo (MC) technique. This study consists of a realistic simulation of the B-SECT system and demonstrates its feasibility for ρ_e imaging. The final chapter summarizes the conclusions of this work and identifies future areas of research.

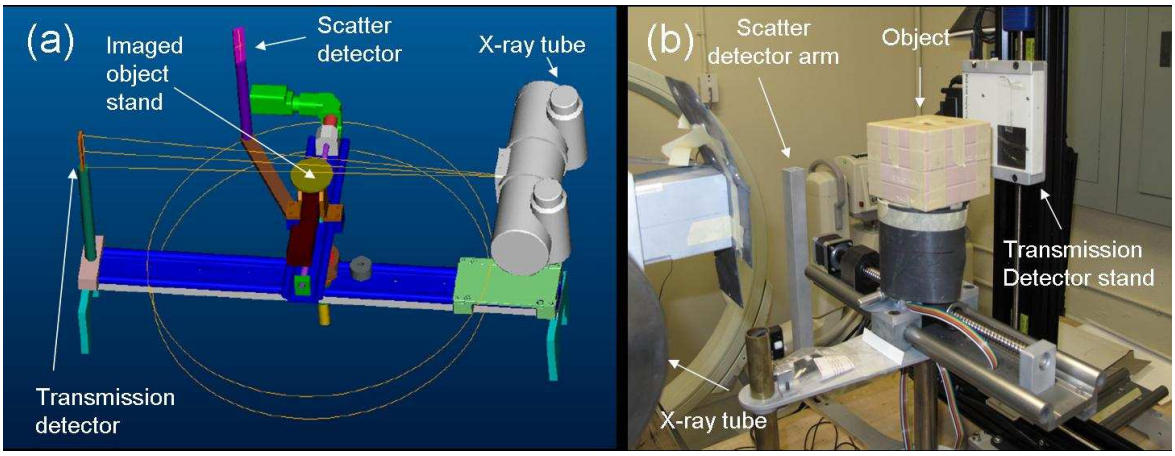

Figure 1.1. Computer design (a) and picture (b) of the B-SECT system that will be used to conduct bench top studies. This system will mimic the ring of detectors of Figure 4.4 by rotating a single scatter detector.

2. Introduction

2.1. *Breast imaging*

Breast imaging is used in the prevention, diagnosis and treatment of breast cancer as well as in the evaluation of breast implants. X-ray planar mammography is the imaging technique most commonly used to image the breast and it will be discussed in section 2.2. In addition to mammography, other imaging modalities exist which are either routinely used or in developing stage. Breast Ultrasound (US) is a diagnostic tool used to differentiate cysts from solid tumors and a recent study showed increased sensitivity when used in conjunction with mammography [45]. Despite this improvement in sensitivity, this study showed an increase in false positives which, coupled with increased imaging time, may limit its ability to be used as a screening tool. An additional limitation of current breast US is the lack of studies comparing its individual performance against mammography [46, 47]. Magnetic resonance imaging (MRI) is an important diagnostic tool for breast cancer [48]. Studies show that it has the largest sensitivity of all other modalities but it also has reduced specificity which results in higher call-back rates [49]. This reduced specificity, similarly to US, is the main reason why the screening role of MRI remains limited to women with high risk of developing cancer [50]. Nuclear medicine is also used in breast imaging and covers modalities like scintigraphy, single photon emission computed tomography (SPECT) and positron emission tomography (PET). Its uses include the characterization of palpable lesions that are undetermined with

mammography and the study of breast cancer recurrence. However their current role remain as adjuncts to mammography due to their low sensitivity, specially for small tumors (<1 cm) [51]. Aside from the conventional modalities mentioned above, there is ongoing research in new and innovative techniques. Techniques like microwave imaging, diffraction enhanced imaging and optical imaging are being investigated but more research is needed before they can be translated into the clinic [47].

X-ray volumetric techniques, such as breast tomosynthesis [52] and breast CT (BCT) [9], have shown potential to replace planar mammography [8]. Both techniques consist of taking x-rays projections at different angles which are used to reconstruct 3D images of the breast. Volumetric images reduce the overlap of structure inherent in 2D projections, which is one of the most important factors limiting breast lesion detection [53]. Volumetric techniques have significantly outperformed mammography in the detection of 5 mm lesions [54].

Breast tomosynthesis can be regarded as limited angle CT since it takes fewer projections over a limited angular range. The incomplete data acquisition results in reduced dose than CT but also in reduced resolution and blur along the direction of the beam which could limit the detection of small abnormalities. The lack of data acquisition over the entire object is the reason why tomosynthesis can not reconstruct accurate images of the μ [55]. A recent study showed that there is a linear relationship between breast density and the value of the reconstructed tomosynthesis voxel [56]. This can potentially result in quantitative breast diagnosis but tomosynthesis remains physically dependent on the μ. Since the purpose of this study is to evaluate the benefit of simultaneously reconstructing images of μ and ρ_e, BCT

was selected as it allows more accurate reconstruction of the μ. Further background on BCT will be given in section 2.3.

2.2. *X-ray mammography*

Mammography could potentially refer to any technique used to image the breast. However the term mammography commonly refers to x-ray radiographs of the breast used to detect abnormalities. Mammography is the current gold standard for breast imaging due to its high sensitivity and resolution for relatively low dose, cost and complexity [57]. It is used both for diagnosis and large population breast screening. A typical mammography study consists of one or more x-ray radiographs of a compressed breast. Breast compression is specific to mammography and is used for many reasons. Breast compression reduces the overlap of structures and amount of radiated material. By reducing the thickness of radiated breast, the dose is reduced. The reduction of breast thickness also reduces contaminating scatter that can potentially reduce contrast. The drawback of breast compression is that it is an uncomfortable procedure and can prevent women from participating in a screening test.

Figure 2.1 shows the variation of the μ for different materials in the breast as a function of energy. This figure shows the challenge faced by mammography since the subject contrast, given by the differences between the μ of normal (fat and fibrous tissues of Figure 2.1) and malignant tissue (such as IDC in Figure 2.1), is smaller than 6% at an energy of 20 keV [10]. It can also be observed that the contrast reduces to less than 2% as the energy increases. This is the reason why mammography x-ray tubes operate at lower energies. Reducing the energy

leads to large x-ray absorption which can potentially result in higher dose. It has been shown that the majority of photons with energy less than 10 keV are absorbed in the first 2 cm of the breast [58] and are unlikely to contribute to image formation but to dose only. Consequently mammography tubes have undergone refinements over the years to optimize the trade-off between breast dose and contrast. Among the most common target/filter combinations are Mo/Mo, Rh/Rh, Mo/Rh and W/Al. The selection of the target material, with the exception of W, is driven by the energy of the K-edges of the corresponding element (20.00 keV for Mo and 23.22 keV for Rh). The produced spectrum is then filtered by a material which allows the output of characteristic x-rays while absorbing bremsstrahlung photons. The W/Al combination gained interest with the advent of digital mammography [59].

MCC are important indicators of certain types of cancer (e.g. ductal carcinoma in situ [13]). This implies that mammography systems must have a spatial resolution that enables the detection of objects as small as 100 microns [60]. This high resolution is not typically required in other radiological studies and led to the development of tubes with small focal spots [61]. Apart from the x-ray source, the detector also plays an important role in the resolution of the system. Mammography systems can be either film-screen based or digital. Film-screen systems have higher spatial resolution than digital systems (20 lp/mm vs 10 lp/mm [7], where lp stands for line pairs). However digital systems have larger detective quantum efficiency, larger contrast display and are readily available for image processing. In addition, studies show that digital systems can perform equally or even better than film-screen for breast screening [62]. Given the current trends it can be envisioned that digital systems will become standard in mammography [47].

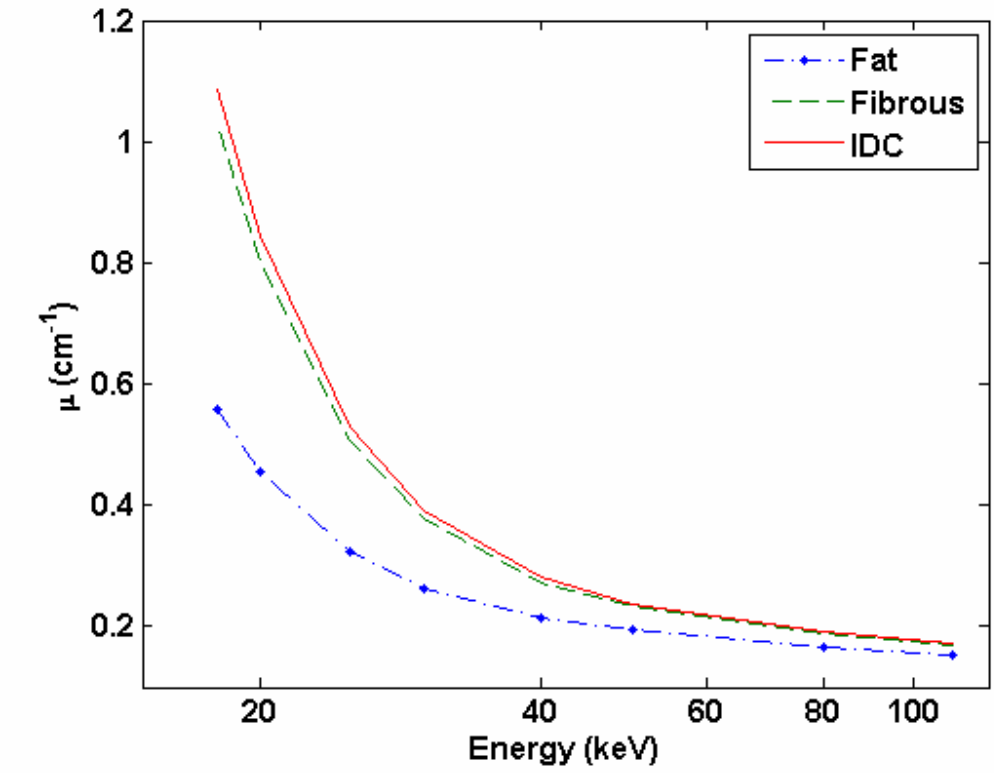

Figure 2.1. Variation of the μ as a function of energy for different breast tissues: fat, fibrous and infiltrating duct carcinoma (IDC) [10].

Projection images are based on the assumption that photons travel along a line defined by the x-ray source and the detector. Scattered photons, by definition, undergo a change of their original direction and carry information away from the site of the original line. In the case of mammography, it is well known that scatter results in reduced contrast [63, 64]. Many factors affect the distribution of scatter and among the more dominant ones is breast thickness with energy and composition being less dominant [65]. One of the most common

correction approaches consists on the use of anti-scatter grids [63]. Anti-scatter grids consist of strips of highly attenuating material which are designed to absorb x-rays that do not come from the source. These grids effectively reduce scatter but at the expense of reducing primary photons and a corresponding dose penalty. Breast compression reduces the thickness of breast traversed by the beam which has the additional benefit of reducing scatter as indicated in the first paragraph of this section. Another approach consists of increasing the air gap between the breast and the detector but the finite size of the x-ray source leads to image blur. Consequently, air gaps result in reduced resolution [66] and this approach is usually limited to specific magnification studies. An alternative solution consists of using slot-scanning devices which use narrow beams to scan the breast. Slot-scanning systems can reduce scatter by as much as a factor of 14 [65] but this reduction comes at the expense of increased tube loading and imaging time. In summary, scatter reduces the contrast in mammography studies and there exist multiple techniques to reduce it. These approaches come at the expense of dose, exposure time, patient discomfort and decreased resolution.

X-ray examinations increase the risk of developing a complication as a result of exposure to radiation. This risk should be out-weighted by the benefit of the examination and becomes particularly important in screening, where large groups of asymptomatic women are examined over a few years. Different quantities have been proposed to quantify mamographic dose but the mean glandular dose (*MGD*) is currently accepted as the standard. The *MGD* provides a measure of the overall dose deposited in the breast tissue where cancer is more likely to develop. The *MGD* is dependent on the kVp and filtration of the beam as welll as breast thickness and composition [67, 68]. Currently, the American College of

Radiology recommends that the *MGD* of a mammography study should not exceed 3 mGy per view for a 4.2 cm breast with equal composition by weight of adipose and glandular tissues [58]. The use of a standard *MGD* allows control of the population dose and facilitates the comparison between different imaging studies. Typical values of the *MGD* range from 1.5 mGy to 2 mGy per view [7]. As a consequence, BCT studies have adopted a *MGD* corresponding to a typical 2-view mammography study [9, 69]. This 4 mGy dose has been adopted in this dissertation to be consistent with the standard development of breast imaging.

Even though mammography has undergone many improvements, its diagnostic capabilities are limited by the following issues. Mammography is a projection technique which creates a two dimensional (2D) image of three dimensional (3D) objects. The resulting projection represents the integral of absorption through different structures in the direction of the incoming beam and hence does not provide depth information. It has been suggested that the structural overlap can combine in such a way that the lesion visualization may be obscured [70]. Mammography requires breast compression to reduce dose, scatter and improve image quality but this procedure can be uncomfortable for the patient. Diagnosis is based on the visual inspection of the mammogram by looking for qualitative differences between normal tissue anatomy and abnormalities. Although mammograms are inspected by experienced radiologists, their diagnosis can vary significantly depending on the interpreter [71-73]. It has been estimated that as many as 25% of radiographically visible cancers can be missed due to the subjective nature of mammography [74]. This in turn results in variations in both sensitivity and specificity that can lead to misdiagnosis.

The overall performance of mammography, and many imaging systems, is evaluated by its specificity and sensitivity. Specificity refers to the ability of a system to detect the absence of disease and 100% specificity implies that false positives are zero. Current studies indicate that the specificity of mammography ranges from 94% to 97% [5]. This limited specificity can result in false positive which consequently lead to unnecessary follow up and stress to the patient. For example, the Manitoba Breast Screening Program reported that 90% of cases (screened from January of 2006 and December of 2007) initially called as abnormal turned out to be benign [3]. These patients underwent a variety of tests including diagnostic mammograms, biopsy studies, US and surgical consultations that could have been avoided by a more specific diagnostic test. Sensitivity refers to the ability to detect the presence of disease and 100% sensitivity implies that all abnormal tissues are detected. Current mammography systems have sensitivities that range from 71% to 98% (when screening is performed at a 1 year interval) or from 53% to 86% (when screening is performed at 2 years intervals) [5]. This limited sensitivity results in cancers that are potentially missed by mammography.

Despite its limitations, mammography detected as many as 6,900 cancers in Canada between 2003 and 2004 [6]. In Manitoba alone, it has been reported that about 300 cases were detected in a 2 year period. This report also suggested that the screening program reduced mortality from breast cancer in the province by 24% [3]. The reduction in mortality has been reported by other studies but there is still an ongoing debate on the effect of mammography in the reduction of breast cancer mortality [75]. Whether this debate is resolved, and independently of its outcome, one thing is clear: the limitations of mammography need to be

addressed if improvements in sensitivity and specificity are to be obtained. One approach of doing so is to develop alternative imaging modalities which overcome these limitations.

2.3. *Breast CT*

The first CT studies of the breast were performed using whole-body scanners by having the patient lying in prone position. This configuration has the advantages of imaging deeper into the body (specifically into the chest) while using scanners currently available in the clinic. However the x-ray beam has to penetrate through the thorax which usually requires large doses and energy, which in turn can decrease contrast [70]. The recent development of flat panel imagers has created new interest in dedicated BCT. The term BCT will refer to dedicated systems as opposed to studies conducted with whole-body scanners. Figure 2.2 shows the schematic of most BCT systems [9, 69, 76-78]. The systems consist of a 2D flat panel detector and an x-ray tube which rotate around the breast acquiring multiple cone beam projections. The breast is scanned while the patient lies in prone position on a couch which has an opening for the breast. BCT systems are currently being investigated by the academic groups listed in Table 2.1. Clinical studies [11, 79] have also been conducted and show that the overall performance of BCT is equivalent to mammography. The implementation of commercial BCT systems has also been reported elsewhere [80].

Figure 2.2 shows that current BCT configurations expose the breast while sparing the thorax. By avoiding radiation to the rest of the body, it is possible to perform BCT using the same dose as two view mammography [9]. Thorax sparing allows the use of an energy lower than

that typical of CT (as large as 150 kVp) and hence, as shown in Figure 2.1, increases the difference between the μ of breast tissues.

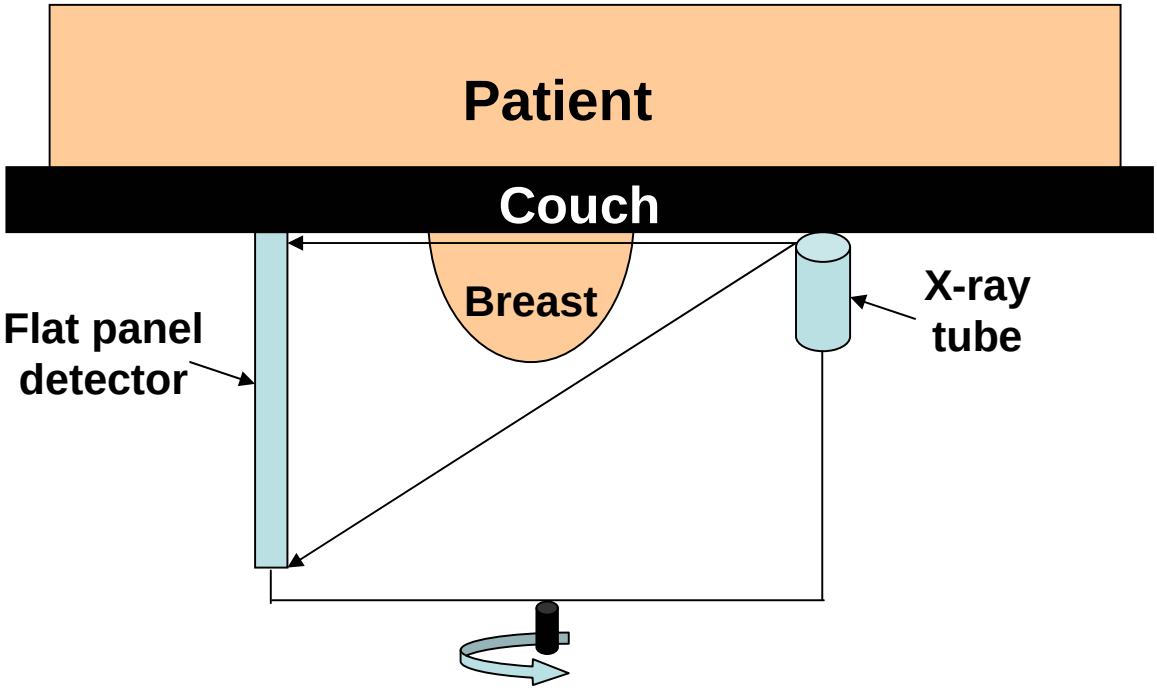

Figure 2.2. Schematic of the proposed dedicated BCT using flat panel imagers.

BCT is under development and the impact that system parameters can have on image quality is still under investigation. These parameters include x-ray beam, geometry, detector, material scintilator, image acquisition and reconstruction algorithm. Many parameters are still being optimized and a summary of those used by different groups is listed in Table 2.1. Table 2.1 shows similarities over different designs with the exception of the one from the group at Duke University. The design from Duke University uses quasi-monoenergetic beams, can describe any scan orbit and uses an iterative reconstruction algorithm [76, 81, 82]. In addition to these differences, all systems use tungsten (W) anode tubes, CsI(Tl)

scintilator and flat panel detectors with similar characteristics. In terms of geometric configurations there are different combinations of source to image distance (SID) and source to detector distance (SDD) which result in magnification factors ranging from 1.3 to 1.9. It can also be observed that the tube potentials are higher than those typically used in mammography (between 24 and 35 kVp [7]). The group at the University of California has investigated beams produced by changing the potential from 30 kVp to 130 kVp [83] and including a bow-tie filter. The bow-tie filter is used to shape the incident beam to the cylindrical geometry of the breast. More recent studies have reported that 80 kVp is the potential most typically used for breast scanning [11, 84] but can range from 60 kVp to 100 kVp[85]. Glick *et al.* (from the University of Massachusetts) investigated the effect of different x-ray spectra on the detection of a 5 mm to 10 mm tumor mass using as a metric the ideal observer signal-to-noise ratio (SNR) [86]. Their results demonstrated that the SNR of BCT is strongly dependent on the combination of kVp as well as filter Z and thickness. Based on these results, it was concluded that the optimal tube potential ranges from 40 kVp to 70 kVp for filter materials with Z ranging from 57 to 65. McKinley *et al.* (Duke University group) investigated the effect of filter selection in order to produce quasi-monoeergetic beams out of tungsten anodes [82]. Their results found that filtering the beam with materials whose Z range from 57 to 63 produced quasi-monoenergetic beams with maximal SNR per dose and exposure for potentials from 40 kVp to 70 kVp. Aside from the x-ray tube based studies, Pani *et al.* has also investigated BCT using synchrotron generated monoenergetic beams with energy from 20 keV to 28 keV [87]. Despite the efforts to optimize the energy of BCT, there is still no general consensus on the x-ray beam that provides its optimal performance.

Table 2.1. Summary of system parameters used by different BCT groups. These groups correspond to the University of California at Davis (UC Davis), University of Rochester (U Roch), University of Massachusetts (U Mass), University of Texas (U Texas) and Duke.

Parameter	Group				
	UC Davis	U Roch	U Mass	U Texas	Duke
X-ray beam					
Anode	W[a)]	W	W	W	W
kVp	30-130	40-70	30-100	60-100	40-100
filter	Teflon (bow-tie)	---	Z=10 to 70	Z=13(Al)	Z=51 to 65
Geometry					
SID[b)] (cm)	45.9	65.0	60.0	75.0	35.0
SDD[c)] (cm)	87.8	103.8	80.0-86.0	100.0	55.0
Magnification	1.91	1.58	1.33-1.43	1.33	1.57
Detector					
Dimension (cm)	30 x 40	---	19.5 x 24	30 x 40	---
Pitch (μm)	194	194	127	194	127
Scintilator	CsI(Tl)	CsI(Tl)	CsI(Tl)	CsI(Tl)	CsI(Tl)
Data acquisition					
Orbit	Circular	Circular	Circular	Circular	Multiple
# of projections	500-1000	300	---	300	240
Image Reconstruction					
Algorithm	FDK[d)]	FDK	FDK	FDK	OSTR[e)]
Voxel size[f)] (μm)	162-324	100-244	100	145	125

[a)]W = Tungsten, [b)]SID = Source to isocenter distance, [c)]SDD = Source to detector distance, [d)]FDK = Feldkamp algorithm, [e)]OSTR = Ordered subsets transmission algorithm and [f)] Voxel size corresponds to the slice in the coronal plane.

One of the main motivations of BCT is the visualization of the breast in 3D while reducing the overlap of structures. Mammography consists of a 2D projection technique; hence its image represents the superposition of multiple structures along the direction of the beam. This results in structural noise (i.e. anatomic variation where an abnormality can reside) that can limit disease diagnosis within normal breast anatomy [70]. The pioneering work of Boone *et al.* showed that for an 11 cm breast, the tomographic nature of BCT can reduce the volume of over and underlying tissue by a factor of ~100 [9]. Using BCT, Boone *et al.* were able to differentiate ductal structures that were not observable in projection images. This pioneering study also simulated the SNR of BCT and showed that lesions as small as 2 mm can potentially be detected. Detecting lesions of these size is expected to effectively reduce mortality and has been recommended as the target for any screening modality [88]. As a comparison, the size of lesions currently detected with mammography ranges from 11 mm to 16 mm. Gong *et al.* found that BCT can detect 5 mm lesions with significantly higher confidence than mammography [54]. According to the review paper by Glick [70], the detection of 5 mm lesions could increase breast cancer survival by as much as 10% with respect to the survival associated with the sizes currently detected by mammography. As mentioned above, MCCs are often associated with cancer and their physical and morphological patterns are commonly inspected by radiologists in order to make diagnosis. The compression and 2D nature of mammography can potentially deform MCC clusters. In the contrary, simulations studies suggest that BCT can detect MCC as small as 175 μm with minimal deformation of the breast [89].

An additional benefit of BCT is the lack of breast compression. In the clinical study of Lindfords *et al.*, 82 women were asked to compare BCT comfort with respect to that of mammography by ranking on a scale from 1 to 10 (where 10 indicated a clear preference to BCT). Two-thirds of women answered 10, indicating a statistically significant preference to BCT comfort over mammography [11].A typical breast compression of 120 N results in breast pain in many patients and can prevent women from participating in mammography studies [90, 91]. The absence of pain related to BCT could potentially encourage more women to participate in screening programs, thereby increasing their targeted volumes as well as retention rates [92].

The use of a breast holder in BCT has been suggested to stabilize the pendant breast and separate it from the chest wall. The holder could also reduce cone beam artifacts and improve uniformity of the x-ray beams through the breast by shaping it as a cylinder [93]. Although this would require a slight pressure, this would be gentle and would not require the compression used in mammography [9]. Another potential advantage of BCT is that it reconstructs images of the linear attenuation coefficient μ. The difference between the μ of malignant and normal breast tissues is statistically significant for energies lower than 40 keV [82]. This indicates that the μ can be used to discriminate between breast tissues and can potentially be used to quantify them. Quantitative BCT is a topic that remains unexplored but could ultimately improve tissue characterization [56, 94, 95]. In addition, quantitative imaging can be used as a complementary tool that can help reduce the subjective limitation of qualitative diagnosis [96].

Despite the encouraging results of BCT, the technique suffers from a number of challenges. The μ may be insufficient to specify tissues due to its inherent dependence on other physical properties: the energy, Z and ρ_e. Even if the energy of the beam is experimentally fixed, it is still possible to have materials with different Z and ρ_e that combine to yield similar μ. Anikonow *et al.* have compiled a comprehensive list of pairs of materials whose visualization may be limited with the use of CT alone [97]. Furthermore, Chen *et al.* were unable to find differences between the μ of fibrous tissue and tumors at energies from 15 keV to 26 keV [14]. This implies that the μ may not be sufficient to differentiate between these two tissues, contrary to the widely acknowledged results of Yaffe *et al.* [10]

BCT diagnosis may also be limited by the non ideal reconstructions resulting from noise and scatter [43, 44, 98, 99]. Cone beam reconstructions are prone to artifacts but these can be reduced to negligible levels even for large breasts [99]. BCT image noise varies as a function of system design parameters, reconstruction technique and scatter [100, 101]. Ultimately, dose constraints result in non-negligible noise and is therefore desirable to investigate noise reduction techniques without incurring in additional dose [102]. Scatter contamination remains as one of the most challenging problems of cone beam CT [98]. Studies show that the scatter-to-primary ratio of BCT can be as large as 0.5 for a typical breast [43, 44]. These levels of scatter can result in image artifacts and increased noise that can limit the accuracy of the μ image. Current approaches to handle scatter consist of post-reconstruction corrections for symmetric cupping artifacts based on the spatial variation of adipose tissue [98].

Perhaps the most limiting challenge of BCT is its limited visualization of MCC. Despite the encouraging simulations of Gong *et al.*[89], experimental studies show that MCC detection is dependent on tube voltage and radiation dose and may require doses as large as 24 mGy to resolve MCC of 300 μm [103]. The clinical study of Lindfors *et al.* also found that BCT was outperformed by mammography in the detection of MCC. While the role of BCT remains to be determined (either as diagnostic or screening tool), its current limitations must be addressed before it can be used in the clinic.

2.4. *Scatter imaging*

The fundamental contrast of BCT is based on the difference between μ for different breast tissues. These differences may not be sufficient to completely characterize tissue and, as such, the information from any other physical characteristic (e.g. ρ_e and Z) may show additional information [36] that can aid in tissue diagnosis. Electron density images could also be useful in radiation therapy planning [32] and measurement of bone mineral content [33]. The use of ρ_e for breast diagnosis has been studied by Al Bahri *et al.* [40], Ryan *et al.* [39, 41] and Van Uytven *et al.*[15, 16]. Their results indicate that ρ_e has the potential to provide tissue information that can increase specificity in breast diagnosis.

Electron density images can be reconstructed using incoherently scattered photons. The number of single incoherent scattered photons is linearly dependent on the ρ_e of a small volume. This dependence makes it trivial to extract the ρ_e of small samples but, for larger

objects, the complex contribution of multiple factors can limit the ability to reconstruct an ρ_e image. These factors include the attenuation experienced by photons, anisotropic probability of scattering and detection, and contaminating scatter. A number of different approaches have been attempted over the years to overcome these issues and are summarized below.

It is widely acknowledged that Lale was the first to explore the use of incoherent scatter for imaging applications [35]. This author devised a system based on a high energy (^{192}Ir source with energy varying from 300 keV to 600 keV) pencil beam and a collimated detector, which limited the detection of scattered photons to a volume defined by the collimator acceptance angle and beam thickness. Farmer and Collins expanded this idea by replacing the collimator with an energy sensitive detector [34]. The relationship between energy of the scattered photon and its scattering angle allowed them to image a single line of the patient using a single beam as opposed to a small volume as done by Lale. This approach was limited by the detection of multiple scatter and photon attenuation. Clarke and Van Dyk [33] followed with a densitometer system where attenuation correction was achieved using transmission measurements. For each point in the body, pairs of transmission and scatter measurements were taken by ensuring that the attenuation of the scattered photons was equal to the attenuation of the transmission beams. These measurements result in a set of equations that can be solved for the ρ_e but the pair of attenuation measurements per point makes the system dose inefficient. Battista *et al*. adapted Clarke's densitometer using a collimator to collect the scatter of small volume and scanning a patient on a point-by-point basis [104, 105]. The scan from a previous point was used to correct for attenuation while multiple scatter was corrected based on empirical observations. The system was found to be accurate to within ±4% and

was used to develop calibration curves to convert CT numbers into relative electron densities. However the potential of scatter imaging was believed to be limited based on the ability to obtain relatively accurate ρ_e using transmission CT, as well as its faster acquisition time, convenience and lower dose [32]. A commercial Compton scanner (the ComScan [30]) was implemented for superficial imaging but was mostly used for non-destructive imaging [26].

The approaches previously described relied on either collimation or energy discrimination to determine the location of scattering centre and its corresponding ρ_e. Other authors have relied on solving optimization problems using computer algorithms. Optimization reconstruction approaches use an ρ_e estimate to predict the distribution of scatter measured by the system. This "forward problem" is compared with actual scatter measurements and the ρ_e is adjusted until the difference between the two is minimized. Prettyman *et al.* were the first to apply optimization approaches to reconstruct ρ_e images using constrained least squares [106]. Their system proposed the simultaneous use of transmission CT with scatter imaging, where the former was used to correct for attenuation. Arendtsz and Hussein formulated the forward problem of scatter by including the energy of the detected photons and explicitly stating the non-linearity of the problem introduced by attenuation. The system was inverted using a successive approximation process that did not require a set of transmission measurements but its convergence was constrained to thin objects [27, 28]. Khetabi *et al.* used a system based on a pencil beam that followed a raster scan and detected photons scattered in orthogonal directions [18]. This system was used to reconstruct a 3D image of the head using a single projection and dose lower than CT [107]. However, the system requires high energies (300 kV to 450 kV) to provide acceptable measurements and to simplify the mathematical model

used in the reconstruction [108]. Busono and Hussein attempted to recover the linearity of scatter imaging by using simultaneous CT measurements and including the μ values in the forward model. This approach reconstructed accurate images of ρ_e out of MC simulated data but no experimental results have been reported [24]. Arsenault and Hussein followed with a single-projection fan beam reconstruction approach that avoided the tedious measurement of multiple transmission projections [17].

Optimization approaches are computationally expensive, complex and require the selection of regularization parameters that can affect the inversion of ill-posed problems such as scatter imaging. This lead Norton to develop an analytical algorithm that, based on the relationship between the energies of the incident and scattered photons, back project the scatter measurement along circular paths [29]. This approach is similar to the filtered back projection (FBP) algorithm, commonly used in commercial CT scanners [109], and could provide a computationally efficient scatter imaging algorithm. The model proved to be directly applicable to scatter measurements [110] but was not tested against MC simulations nor measurements.

Incoherent scatter CT (ISCT) has also been investigated using first generation CT. First generation CT consists of using a narrow x-ray pencil beam that is scanned along an object. Once the beam translation is finished, it is rotated and the scan is repeated. First generation CT was used in the early days of CT but is no longer used due to its long acquisition times. Instead, first generation CT is used in selected applications like coherent scatter (CSCT), ICST and fluorescent x-ray CT (FXCT) [111]. These systems are suitable for laboratory

measurements where time is not usually an issue. The small beam size results in primary measurements with reduced scatter contamination [112], which if not corrected, can lead to μ images with reduced contrast, image artifacts and inaccurate CT numbers [113, 114]. In addition, these systems can be easily assembled by using a turntable which rotates and translates the object while the source and detector remain stationary. This reduces the mechanical and electrical challenges of clinical designs. This has the added benefit of providing a cost effective system to experimentally prove a hypothesis[*]. First generation CT also limits the measurement of any given quantity to a single line along the object, resulting in independent measurements of ray integrals.

The use of scatter for breast diagnosis has been mainly limited to coherent scatter. Studies show that the diffraction patterns of breast tissue (such as peak height, location and area) may be used to characterize tissue [115-120]. It can be envisioned that CSCT [121] can be used to reconstruct breast images of the atomic form factor. Imaging of the breast using incoherent scattered photons was achieved by Van Uytven *et al*.[15, 16]. Their results showed that it is feasible to reconstruct ρ_e breast images using the same dose as mammography and incoherent scatter. Their results also showed potential for MCC detection which remains one of the main challenges in BCT. Their system however is based on detectors that measure the energy of the scattered photons with a resolution of 200 eV. This energy resolution can be achieved with room temperature semiconductors for mammographic energies but not at higher energies [122]. This limits the technique to a particular range of energy unless cryogenic detectors are used, making it unpractical and expensive.

[*] For example, it is expected that a photo multiplier tube can be used for the initial measurements of the B-SECT system (see Chapter 5).

The ultimate benefits of reconstructing simultaneous images of breast ρ_e and μ may not be completely identified until more measurements are made. These measurements should first be conducted using laboratory systems to image breast phantoms, samples, mastectomies and, if possible, volunteers. As such, first generation B-SECT provides a practical technique, in terms of simplicity and cost-effectiveness, to conduct the desired experiments. Before the B-SECT system is used, it is necessary to develop a reconstruction algorithm for accurate ρ_e imaging of the breast for doses typically used in mammography. The reconstruction algorithm is the purpose of this thesis and is developed from simplistic (and fundamental) simulations of single KN scatter (Chapter 4). The algorithm is novel in its ability to simultaneously correct for attenuation and the anisotropic probability of scatter and detection. The algorithm also provides a good trade-off between reconstruction accuracy, simplicity and computer power. This reconstruction algorithm was then tested against the simulation of the B-SECT system using the MC method and including all types of scatter (Chapter 5). This was the next logical step towards the incorporation of realistic issues and is used to test the hypothesis of this thesis (as stated at the end of Chapter 1).

3. Physics background

This chapter describes the fundamental physics that were used in this thesis. These concepts, equations and methods are not original to this work. The novel contributions of this thesis are developed in chapters 4 and 5.

3.1. *Photon interactions*

As a beam of x-rays travels through matter it can interact by three different processes (for energies lower than 1 MeV). These processes are the photo-electric effect, incoherent (also called Compton) scatter and coherent (also called Rayleigh) scatter. As a result of these interactions, the number of incident photons (N_0) is reduced according to

$$N_t = N_0 \, e^{-\int_0^L \mu(l)dl}, \qquad (3.1)$$

where N_t is the number of transmitted (or non-interacting photons) and μ is the linear attenuation coefficient of the material with thickness L. The μ of the object can be decomposed into the individual contributions from each process as

$$\mu = \mu_{photo} + \mu_{incoh} + \mu_{coh} \qquad (3.2)$$

where μ_{photo}, μ_{incoh} and μ_{coh} are μ corresponding to each interaction process. An equivalent equation can be written for the mass attenuation coefficient (μ/ρ), defined as the ratio of the μ and material density ρ. There is no equation that can exactly predict the behavior of μ for all energies and materials. However approximate models can be derived. For example, coherent scatter can be assumed to be negligible for materials with small Z at high energies. Assuming that the contribution of coherent scatter is negligible, with respect to the other two, the mass attenuation coefficient can be approximated by [123]

$$\frac{\mu}{\rho} \approx a\left(\frac{Z}{E}\right)^n + N_A\left(\frac{Z}{A}\right)_e\sigma(E) \qquad (3.3)$$

where E is the energy of the incoming photon, N_A is Avogadro's constant (6.022 x 10^{23} per mole) and A is the atomic weight of the element with atomic number Z. The parameter a is a proportionality constant while the exponent n is dependent on both on material and energy [124]. The ${}_e\sigma(E)$ term is the total incoherent scatter cross section in cm^2/electron. The product of $N_A(Z/A)$ represents the number of electrons per gram and is related to the ρ_e by

$$\rho_e = \rho N_A\left(\frac{Z}{A}\right), \qquad (3.4)$$

where the units of ρ_e are electrons/cm^3. These equations show the explicit dependence of the μ on ρ_e, Z and energy and the challenge to characterize a material based on the μ only. Even

if the energy of the beam were constant (monoenergetic sources), there is still the possibility that two materials with different Z and ρ_e have the same μ.

3.1.1. Materials mixtures

The above equations can be easily calculated for elemental materials but most tissues consist of mixtures of elements. In addition, there are cases in which one is interested in calculating the physical properties of mixtures of materials. In this dissertation, for example, different combinations of adipose tissue, glandular tissue and MCC were investigated. For this reason it is important to have a method to calculate the μ, ρ_e and elemental composition of mixtures (needed for computer simulations). In the following paragraphs the index h will denote a material (e.g. adipose tissue) whereas i will be used to denote elements (e.g. Hydrogen). The following paragraphs describe the procedure used to calculate the physical properties of a mixture given:

(i) The fractions by volume v_h of each material h to the mixture,

(ii) The density ρ_h of each material h and

(iii) The corresponding fraction by weight $w_{h,i}$ of element i in material h.

Let us consider a voxel with volume V made of a mixture of different materials. The total mass of material h is given by

$$m_h = \rho_h v_h V \quad (3.5)$$

and can be used to calculate the total mass of the voxel according to

$$M = \sum_h m_h . \quad (3.6)$$

Using equations (3.5) and (3.6) one can calculate the density of the mixture as

$$\rho_{mix} = \frac{M}{V} = \frac{\sum_h m_h}{V} = \sum_h \rho_h v_h , \qquad (3.7)$$

where the summation is over all materials in the mixture. The relationship between the fractions by weight and volume is obtained by recalling that, by definition, w_h is given by (3.8)

$$w_h \equiv \frac{m_h}{M} . \qquad (3.8)$$

Substituting equations (3.5) and (3.6) results in

$$w_h = \frac{\rho_h v_h}{\rho_{mix}} , \quad (3.9)$$

where Equation (3.7) was also used. Recalling that each material *h* has a fraction by weight of element *i* ($w_{h,i}$), one can calculate the fraction by weight of each element to the mixture as

$$w_i = \frac{\sum_h w_{h,i}\, m_h}{M} = \sum_h w_{h,i}\, w_h\,, \qquad (3.10)$$

where Equation (3.8) was used. Equations (3.7) and (3.10) give the density and elemental compositions needed to simulated an object by means of the MC code described in section 3.4.2.

The mass attenuation coefficient of a mixture of elements can be calculated using Bragg's rule [123]

$$\left(\frac{\mu}{\rho}\right)_{mix} = \sum_i \left(\frac{\mu}{\rho}\right)_i w_i\,, \quad (3.11)$$

where the summation is over all elements i of the mixture and assumes a weighted contribution from its constituents [125]. The μ is obtained by multiplying equations (3.7) and (3.11). To calculate the ρ_e one first needs to calculate the number of atoms per element ($N_{a,i}$) according to [126]

$$N_{a,i} = m_i \frac{N_A}{A_i} = w_i \rho_{mix} V \frac{N_A}{A_i}\,, \qquad (3.12)$$

where A_i is the atomic weight of element i. Finally, the ρ_e is obtained by multiplying by the number of electrons per atom, summing over all elements and dividing by the volume as

$$\rho_{e,mix} = \sum_i \frac{N_{a,i} Z_i}{V} = \rho_{mix} N_A \sum_i w_i \frac{Z_i}{A_i} \qquad (3.13)$$

Figure 3.1 is a graph of the ρ_e as a function of μ at 65 keV for different mixtures of adipose tissue, glandular tissue and MCC. This energy was selected because it will be used in Chapter 5 of this dissertation. The graph emphasizes the range covering points of 100% adipose tissue and 100% glandular tissue (soft tissue changes). Any point along this line represents a combination of adipose and glandular tissue. The point that represents 100% MCC is found at coordinates (μ = 1.1158 cm^{-1}, ρ_e = 9.47 x 10^{23} electrons/cm^3). The dashed line represents combinations of adipose tissue and MCC while the dashed-dotted line represents combinations of glandular tissue and MCC. Any combination of adipose tissue, glandular tissue and MCC is represented by a point inside the area surrounded by the three lines. This figure shows that there are combinations of mixtures that can have the same μ but different ρ_e. For example, consider the point that corresponds to 100% glandular tissue and point "A", which is a mixture of adipose tissue and MCC. The μ of these two materials is virtually the same but their ρ_e differ by about 5% (3.45 x 10^{23} electrons/cm^3 vs 3.28 x 10^{23} electrons/cm^3). A similar argument can be made for mixtures with the same ρ_e but different μ, suggesting potential benefits of combined ρ_e and μ imaging of the breast.

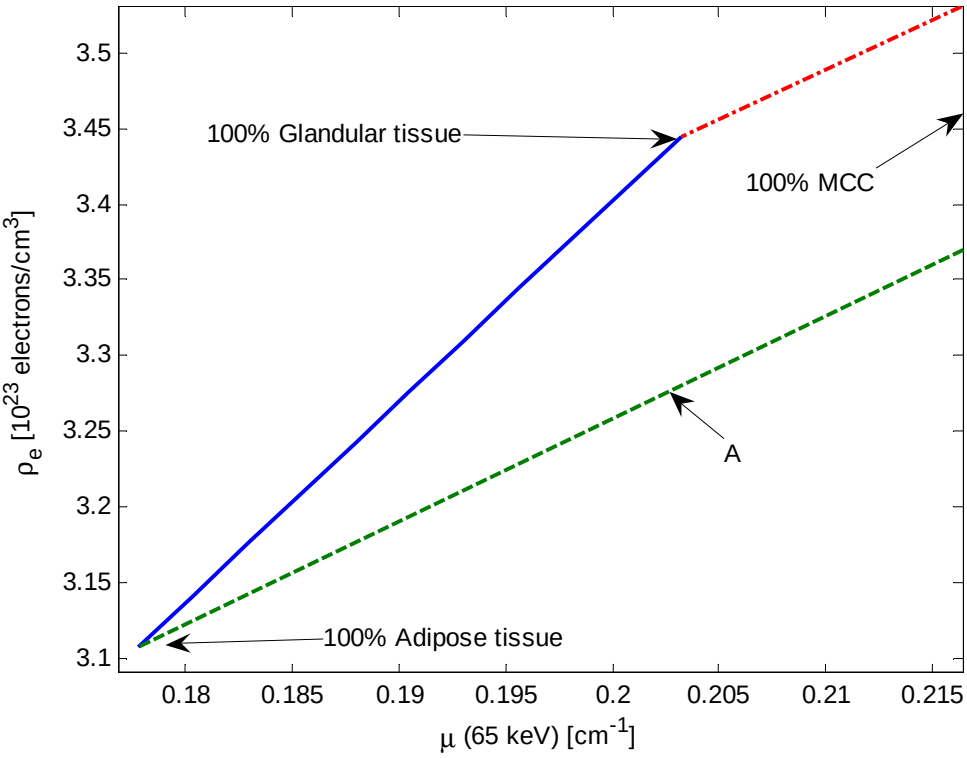

Figure 3.1. Variation of the ρ_e as a function of the μ at 65 keV for different combinations of adipose tissue, glandular tissue and MCC.

3.2. *Physics of scattering*

The general equation of scattering is based on the assumption that the number of scattered particles (N_s) is directly proportional to the number of incident particles (N_0), the density of scattering centres and the probabilities of scattering and detection. This is summarized in the scattering equation which is valid for any scattering process [127]

$$N_s = N_0 n_{S.C.} \frac{d\sigma}{d\Omega} \Delta\Omega \qquad (3.14)$$

where $n_{s.c.}$ is the number of scattering centres per unit area of an infinitesimally thin slab of material. $d\sigma/d\Omega$ is the differential cross section per scattering centre and accounts for the probability of an incident particle being scattered by an angle φ. $\Delta\Omega$ is the solid angle subtended by a detector that measures the scattered radiation and accounts for the probability of detection.

3.2.1. Incoherent scatter

Incoherent scatter is the result of the interaction of a photon with an electron. As a result of this interaction some of the incident photon energy is transmitted to the electron while the photon is scattered through an angle φ with energy E_s. The energy of the scattered photon is given by the Compton relationship

$$E_s = \frac{E_0}{1 + \left(E_0 / m_0 c^2\right)\left(1 - \cos\varphi\right)} \qquad (3.15)$$

where m_0 is the electron rest mass and c is the speed of light in vacuum. Equation (3.14) can be modified to calculate the number of single incoherently scattered photons ($N_{s,incoh}$) reaching a detector located at an angle φ as

$$N_{s,incoh} = N_0 n_e \frac{d_e\sigma_{KN}}{d\Omega}\Delta\Omega \qquad (3.16)$$

where n_e is the number of electrons per unit area of the material and $d_e\sigma_{KN}/d\Omega$ is the KN cross section per electron which is dependent on the energy of the incident photon and scattering angle. The KN differential cross section can be explicitly calculated using

$$\frac{d_e\sigma_{KN}}{d\Omega}(\varphi, E_0) = \frac{r_0^2}{2}\left(\frac{E_s}{E_o}\right)^2\left(\frac{E_0}{E_s} + \frac{E_s}{E_0} - \sin^2\varphi\right), \qquad (3.17)$$

where r_0 is the classical electron radius and has a value of 2.818 x 10^{-13} cm. The KN differential cross section assumes that the electron is free and stationary. This approximation is valid for both large E_0 and φ but breaks down for small values of momentum transfer q. Momentum transfer is defined as

$$q = \frac{E_0}{hc}\sin(\varphi/2), \qquad (3.18)$$

where h is Planck's constant. A common approach to deal with electron binding effects is by introducing the incoherent scatter function $S(q,Z)$ to modify the probability of scattering of Equation (3.16) [128]. Using Equation (3.4) and that $n_e = \rho_e L$, Equation (3.16) can be rewritten as

$$N_{s,incoh} = N_0 \rho N_A L \frac{S(q,Z)}{A} \frac{d_e \sigma_{KN}}{d\Omega} \Delta\Omega \qquad (3.19)$$

where $S(q,Z)/A$ has replaced the (Z/A) term and approaches 0.5 for large values of q in the same way as Z/A does. Hubbell *et al*. have tabulated values of $S_i(q,Z)$ for most elements in the periodic table [129]. In the case of mixtures, the weighted contribution from each element can be used to calculate $(S/A)_{mix}$ according to [117]

$$\left(\frac{S}{A}\right)_{mix} = \sum_i \frac{S_i(q,Z)}{A} w_i \qquad (3.20)$$

The final form of the Equation (3.14) for incoherent scatter is given by

$$N_{s,incoh} = N_0 \rho_{mix} N_A L \left(\frac{S}{A}\right)_{mix} \frac{d_e \sigma_{KN}}{d\Omega} \Delta\Omega \qquad (3.21)$$

3.2.2. Coherent scatter

Coherent scatter is a photon interaction with the atom. In this type of scatter the interaction takes place with the whole atom and can not be directly related to the electron density. Equation (3.14) becomes

$$N_{s,coh} = N_0 \left[\rho \frac{N_A}{A} L \right] \frac{d_a \sigma_{coh}}{d\Omega} \Delta\Omega \qquad (3.22)$$

where the term in square brackets is the number of atoms per cm^2 and the differential cross section per atom is explicitly given by

$$\frac{d_a\sigma_{coh}}{d\Omega} = \left[\frac{r_0^2}{2}\left(1+\cos^2\varphi\right)\right]F^2\left(q,Z\right), \quad (3.23)$$

where the term in square brackets is the Thomson differential cross section and *F(q,Z)* is the atomic form factor. Hubbell *et al.* [129] have also tabulated elemental form factors [$F_i(q,Z)$] that can be used to calculate the form factor of mixtures according to [117]

$$\left(\frac{F^2}{A}\right)_{mix} = \sum_i\left[\left(\frac{w_i}{A_i}\right)F_i^2\left(q,Z\right)\right] \quad (3.24)$$

The dependence of (3.23) on the atomic form factor has lead investigators to use CSCT to reconstruct images of the atomic form factor [121].

3.3. *Computed Tomography*

X-ray computed tomography (CT) is an imaging modality that reconstructs slices of μ by measuring the attenuation of an object at different angles. The attenuation of an object can be derived from transmission measurements by rearranging Equation (3.1) into

$$p \equiv \ln\left(\frac{N_0}{N_t}\right) = \int_0^L \mu(l)\,dl\,. \qquad (3.25)$$

Equation (3.25) defines a "ray integral" (p) of μ along a line of material. Figure 3.2 illustrates the typical geometry of first generation CT. In this figure, the object is represented by the $\mu(x,y)$ function and is being traversed by several parallel pencil beams where x and y are the coordinates of the fixed reference frame. A second reference frame, the t-s frame, rotates around the fixed reference frame by angle θ in a way such that the s axis is parallel to the beams. In accordance with Figure 3.2, Equation (3.25) can be rewritten as

$$p_\theta(t) = \int_{-\infty}^{\infty}\int_{-\infty}^{\infty} \mu(x,y)\,\delta(x\cos\theta + y\sin\theta - t)\,dx\,dy\,, \quad (3.26)$$

where δ is the Dirac delta function and t is the coordinate along the axis of the rotated reference frame that is perpendicular to the beam. Equation (3.26) defines the Radon transform of the $\mu(x,y)$ function. Evaluation of a set of ray integrals for different values of t defines a *projection*, and a set of projections taken at different angles θ can be stacked together in order to generate a *sinogram*. This sinogram can then be reconstructed by means of the filtered back projection (FBP) algorithm [130] according to

$$\mu(x,y) = \int_0^{\pi}\int_{-\infty}^{\infty} P_\theta(\kappa)\,|\kappa|\,e^{i2\pi\kappa t}\,d\kappa\,d\gamma \qquad (3.27)$$

where $P_\theta(\kappa)$ is the Fourier transform of $p_\theta(t)$ and κ is the radial direction of the κ-γ polar system in frequency space. It is important to note that Equation (3.27) can be used to invert any quantity that takes the form of Equation (3.25). That is, ray integrals are not exclusive to the μ and can be used to reconstruct ρ_e images as shown in section 4.2.1. In this study a commercial version of the FBP was used, the iradon function implemented in MATLAB (The MathWorks, Inc., Natick, MA).

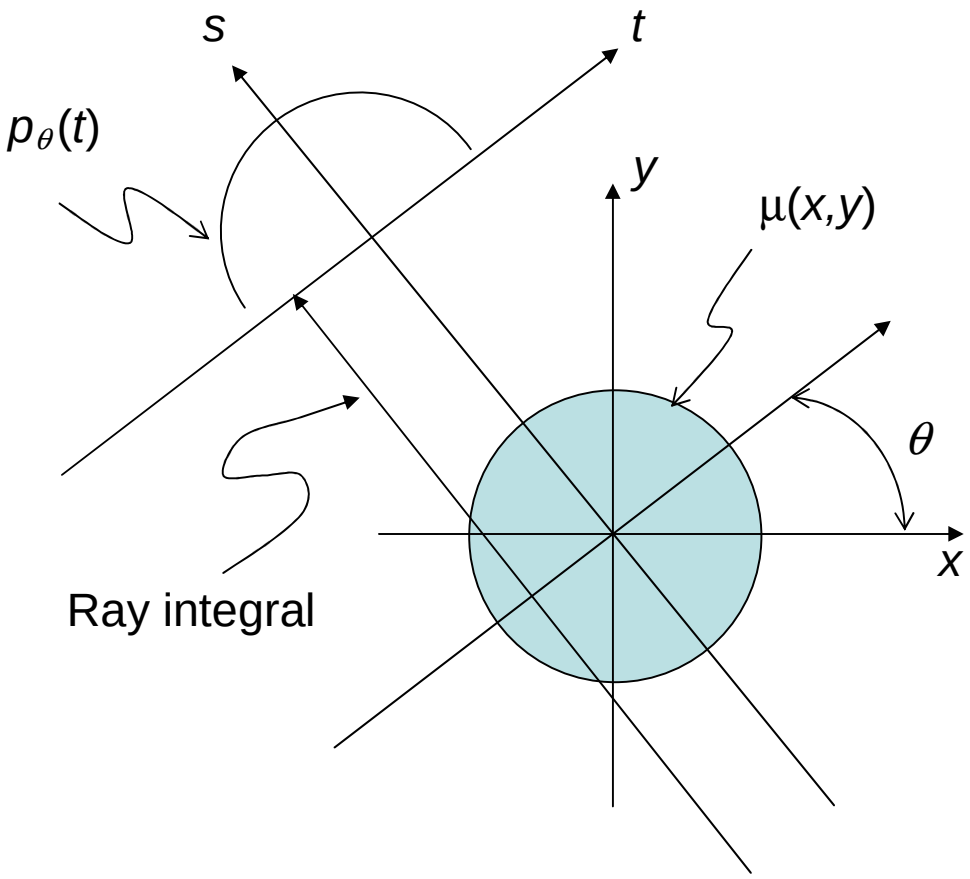

Figure 3.2. Geometry of first generation CT.

The number of projections and beam translations can affect the quality of a CT reconstruction. In transmission first generation CT the size of a ray is defined by the size of the transmission detector (Δ). The transmission detector is used to sample $p_\theta(t)$ and its usually selected to satisfy the sampling criterion of Nyquist frequency. The number of translations is then determined by the ratio of the object FOV and Δ. The number of projections should be selected to be roughly the same as the number of translations and a common approach to reconstruct a matrix of N by N pixels is to use approximately N number of translations and N number of projections [131].

3.4. *Computer simulations: Analytical and Monte Carlo*

This dissertation describes a study conducted using computer simulations. Two types of computer simulations were selected to investigate the viability of the B-SECT system before its practical use: Analytical (AN) and Monte Carlo (MC). The following sections describe the methodology used to simulate the B-SECT system by each method. The detectors were assumed to be ideal in both types of simulations.

3.4.1. Analytical simulations

Analytical simulations use Equation (3.16) to calculate the number of photons measured by an arbitrary scatter detector. AN simulations are faster than MC simulations (to simulate a complete scan of the breast took ~2 weeks with MC and one day with AN) and are free from

the inherent stochastic noise of photon statistics. AN simulations were also used as a set of independent calculations to validate the implementation of the MC simulation. The main limitations of AN simulations are their inability to model multiple scatter and for this reason MC simulations were implemented. The AN simulation was implemented in MATLAB and the process is summarized in the following paragraph. It is assumed that the geometry, number of incident photons (N_0) and energy (E_0) of the incident beam is known *a priori*.

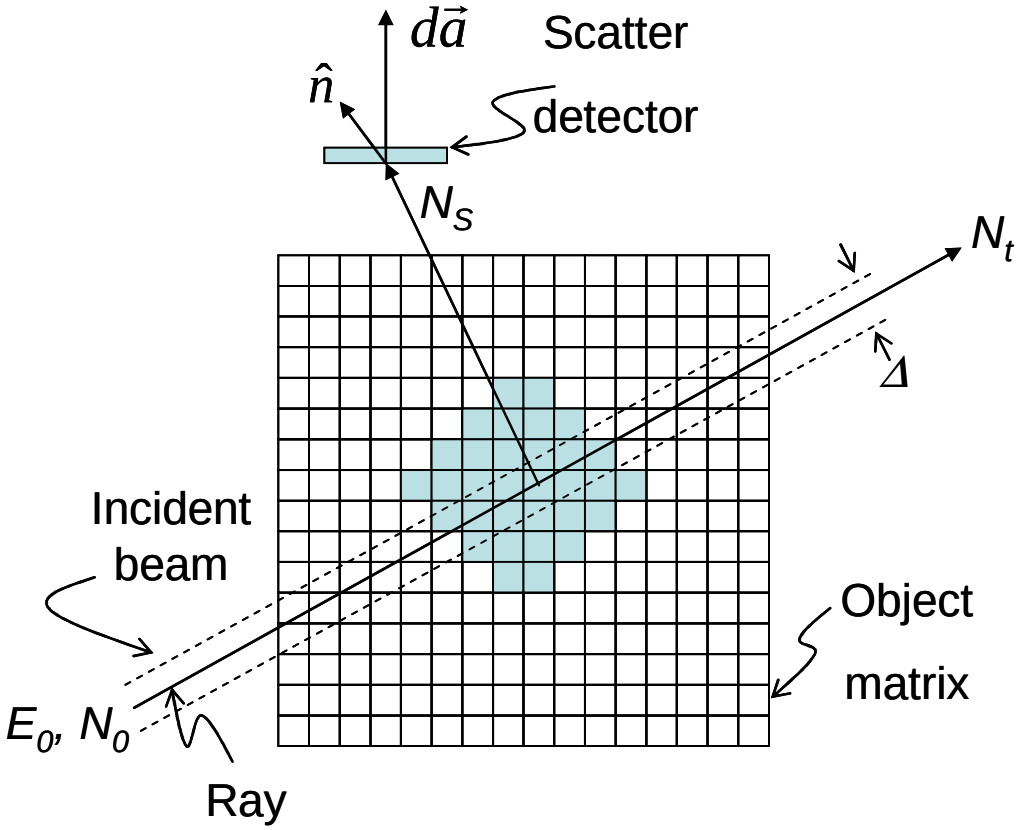

Figure 3.3. Representation of the different elements used in the AN simulation.

Figure 3.3 shows the discretization of the object into voxels where the interaction is assumed to take place. This process was implemented by defining matrices in MATLAB whose elements represent the ρ_e of the voxels. A matrix of the μ was also defined to calculate photon attenuation using Equation (3.1). The figure shows an incident beam with thickness Δ which is then collapsed to a single ray. The ray tracing algorithm of Siddon [132] was used to identify the voxels traversed by the ray along with their corresponding intersection lengths [*dl* in Equation (3.1)]. The point of scatter was assumed to take place half-way between the intersection of the ray with the voxel. The number of incident photons at each voxel was calculated using Equation (3.1) where the integral is taken over the preceding voxels. Siddon's algorithm was also used to identify the voxels intercepted by the scattered photons by tracing a ray from the scattering point to the centre of the scatter detector. These voxels represent the attenuation from the point of scatter to the detector known as the post-scatter attenuation. The post-scatter attenuation was calculated by computing the μ for each material at energy E_s of the scattered photon. The scatter detectors were simulated as squares of area A whose solid angle can be calculated according to [133]

$$\Delta\Omega = \int \frac{\hat{n} \bullet d\vec{a}}{R_d^{\,2}} \qquad (3.28)$$

where $\hat{n}$ is the unitary vector in the direction of the scattered photon, $d\vec{a}$ is the vector area normal to the detector surface and R_d is the distance from the scattering point to the centre of the detector.

3.4.2. Monte Carlo simulations

MC simulations predict physical processes based on random number generators and probability density functions. Since photon interactions are inherently stochastic, MC is a suitable method for the simulation of photon transport. EGSnrc is a MC software that simulates the transport of photons and electrons and has been used in a variety of applications including radiation therapy [134] and medical imaging [135]. It is currently acknowledged that EGSnrc can be used confidently for energies ranging from 1 keV to 10 GeV and the EGSnrc documentation describe in detail the process by which EGSnrc simulates photon interactions [136].

The EGSnrc code must be called by a "user code" to define the simulation materials, geometry and output of the results. DOSXYZnrc is a user code based on EGSnrc used to calculate the dose deposited in rectilinear phantoms [137]. These phantoms are made of parallelepiped voxels similar to those used in the analytical simulation described in section 3.4.1. The typical output of a DOSXZYnrc run consists of the dose deposited in the voxelized phantom. In this study, the DOSXYZnrc main code (named dosxyznrc.mortran) was modified to define the geometry and score the number of photons reaching the geometrical location of the scatter detectors. DOSRZnrc [138], another user code useful in the simulation of cylindrical geometries, was used to score the dose in cylindrical phantoms without any modification (Chapter 5).

The definition of the simulated object is achieved by creating a “CT array” defined in a file with extension .egsphant. This file includes the number of materials that make up the phantom, the materials labels, index array and density array. The label of the material is used to call PEGS4, the preprocessor that generates the data needed by EGSnrc. DOSXYZnrc has a built in list of materials available for simulation and more materials can be added as long as the elemental composition by weight and density of the material are known. These properties were taken from the literature when available or derived from fractions by volume following the procedure described in section 3.1.1.

The DOSXYZnrc user code includes a list of sources available to simulate the incident beam of radiation. First generation CT uses an x-ray pencil beam that was simulated using one of the sources available in DOSXYZnrc (ISOURCE = 1). This source consists of a parallelepid whose coordinates of incoming direction can be modified to emulate the CT scan. The energy of the beam was simulated in two different ways: (i) mono-energetically and (ii) by providing an incident spectrum. The definition of the incoming beam also requires the number of histories to be selected.

EGSnrc incorporates options that enable the user to control some of the physical processes in the simulation. For example, the user can choose different data to calculate photon cross sections. These options have default settings which are intended to provide the most accurate simulation and were left unchanged except for the following cases:

1. Bound Compton scattering. Bound Compton scattering is set as “on” by default and is intended to include electron binding effects. However the reconstruction algorithm

was developed from the simplistic KN approximation and neglects the effects of electron binding. In Chapter 4 the bound Compton scattering option was turned “off” to simulate KN driven incoherent scatter, simplifying the development of the reconstruction algorithm presented below. In Chapter 5 bound incoherent scattering was turned “on” to enable more realistic simulations to be conducted.

2. Rayleigh scattering. The Rayleigh scattering option was turned off at the initial stage of development of the reconstruction algorithm (Chapter 4). The most realistic simulations of the B-SECT system turned “on” this option to include coherent scatter and evaluate its effect in ρ_e reconstructions (Chapter 5).

Note that it is recommended to turn on Rayleigh scattering and bound Compton scattering simultaneously. Failure to do so will result in an overestimation of incoherent scatter since its probability of occurrence should decrease as the probability of coherent scatter increases. These criteria were used in Chapter 5 of this dissertation.

4. A novel hybrid (analytic-iterative) reconstruction algorithm for accurate ρ_e reconstruction of large objects using first generation incoherent scatter CT

The material in this chapter has been reprinted and adapted from the *Journal of X-Ray Science & Technology*, Vol 19(1), Jorge E. Alpuche Aviles, Stephen Pistorius, Richard Gordon and Idris A. Elbakri, A novel hybrid reconstruction algorithm for first generation incoherent scatter CT (ISCT) of large objects with potential medical imaging applications, pp 35-56, Copyright (2011), with permission from IOS Press.

4.1. *Introduction*

Chapters 1 and 2 stated that the purpose of this thesis is to develop a reconstruction algorithm for the B-SECT system. This algorithm falls within the family of first generation ISCT algorithms and in order to prove the hypothesis of this thesis, it is essential that the algorithm is capable of reconstructing *quantitatively* correct images of ρ_e using clinically acceptable doses for objects with *clinically relevant breast sizes*. This chapter addresses the first step towards the development of the algorithm: the reconstruction of ρ_e images from single KN

scatter while neglecting other types of scatter. This is a fundamental and simplistic step of the inverse problem. Generalization of the algorithm to handle more realistic scatter conditions is left for the next chapter of this thesis.

First generation ISCT measures the scatter from an entire line of the object using a non-collimated detector. This results in the detection of single KN scattered photons which is not only dependent on ρ_e, but also on (i) the anisotropic probability of scattering and detection, and (ii) attenuation of photons. These effects can cause scatter variations irrespective of ρ_e changes which can limit the ability to quantify ρ_e. As noted in Chapter 1, previous studies used energy sensitive detectors [16, 27, 29, 34] or collimation [30, 35, 104] in order to image small volumes. However these approaches can suffer from slow scanning times and the detection of small number of photons.

Bratteman *et al*. were the first to employ first generation ISCT to reconstruct qualitatively good images of ρ_e but their results were not quantified [31]. First generation ISCT has also been attempted using conjugant gradient [24], least squares [25], algebraic reconstruction techniques [19, 139] and maximum likelihood expectation maximization [139]. These approaches addressed scatter imaging by casting it as an optimization problem. Scatter imaging however is an ill-posed problem which requires multiple iterations and usually longer computation times [24, 27]. It also requires the careful selection of reconstruction parameters, such as the regularization parameters [24, 27] and the order of projection angles [19], which can affect the solution. As stated in Chapter 2, analytic techniques on the other

hand are directly related to the measurements, can potentially provide faster computation times and avoid the need to invert an ill-posed problem [29].

Hogan and Golosio investigated the use of the FBP algorithm to reconstruct images using a mean attenuation correction [23, 140]. This method provides a good trade-off between practicality and image quality but its accuracy is limited by incomplete attenuation correction [139]. Furthermore, it ignores variations of the scattering probability with location of the scattering centre with respect to the detector caused by the KN cross section and solid angle. This issue is irrelevant for small samples but can lead to scatter variations for large objects with the same ρ_e. For example, consider an 80 keV incident beam traversing a homogeneous object with a 10 cm field of view (FOV) (Figure 4.2). The number photons scattered into a detector normal to the pencil beam and located 35 cm away can change by 7% between the entrance and exit points of the beam. LaRiviere [141] proposed another analytical reconstruction based on the exponential Radon transform and the approximation that the detection probability of emitted photons is constant along the FOV. This approximation also ignores the change in scattering probability as a function of position which is likely to occur in large objects (e.g. larger than 10 cm).

The inability of an algorithm to correct for the variation of scatter with location will cause inaccuracies in the ρ_e reconstruction. In order to address this issue one can assume an "ideal model" of scatter by neglecting attenuation and conceptualizing a 4π detector. This ideal model relates scatter measurements to ray integrals of ρ_e independent of the relative position of the scattering centre with respect to the detector. The impracticality of the 4π detector is

overcome by using an array of individual detectors arranged in a ring configuration. It will be shown in this chapter that the ring approximates the 4π detector by a constant fraction, allowing FBP to be used.

Any successful attempt to reconstruct images of ρ_e must also correct for attenuation. This correction is done by calculating the attenuation that photons experience on their way from the source to the detector. This results in attenuation correction factors (ACFs) that convert the measurements at each detector to those of the ideal model. The attenuation correction is applied iteratively but does not require the formulation of an objective function or selection of reconstruction parameters. Unlike conventional iterative algorithms (where the number of iterations range from 8 to more than 2000 [19, 24, 139]), the attenuation correction applied in this way converges rapidly (7 was the maximum required in this study). The final result is a hybrid (analytic-iterative) reconstruction algorithm for first generation ISCT that corrects for attenuation and quantifies ρ_e of large objects.

As a practical example, the algorithm is used to reconstruct objects with sizes of typical breasts [142]. The desire to keep the dose similar to that of mammography provides a benchmark for the dose performance of the algorithm. The results of this chapter show that the algorithm is capable of reconstructing images of ρ_e in the presence of multiple scatter even while no attempt (in this chapter) to correct for it is pursued.

4.2. *Methods*

4.2.1. Theory

Section 3.2.1. describes the basic physics that will be used to develop the formalism of ρ_e ray integrals. Equation (3.16) relates the number of single incoherent scattered photons measured by a detector (N_{SI}) when a pencil beam traverses a thin slab of material. Figure 4.1 shows a diagram of the beam with cross sectional area S, N_0 incident photons and energy E_0. The figure also shows the slab as defined by its thickness dy, traverse sectional area A (such that $A>S$ and dy can be regarded as infinitesimally small) and the scattering angle φ. Based on this geometry Equation (3.16) can be rewritten as

$$N_{SI} = N_0 n_e \frac{d_e \sigma_{KN}}{d\Omega}(E_0, \varphi)\Delta\Omega(\varphi), \tag{4.1}$$

where the dependence of $d\sigma/d\Omega$ and $\Delta\Omega$ on E_0 and φ is explicitly stated. For large energies and large scattering angles the electrons can be assumed to be at rest and the differential cross section is approximated by the KN cross section [Equation (3.17)]. In the case of low momentum transfer q, where q is given by Equation (3.18), the electron binding effects must be considered by including the incoherent scatter function.

Now, instead of an infinitesimally thin slab, assume that there is a line of material of thickness *L*, then the number of photons scattered by this line into a detector located at an angle δ (Figure 4.2) is given by

$$N_{SI}(\delta) = \int_0^L N_0 \, \rho_e(y) \frac{d_e \sigma_{KN}}{d\Omega} [E_0, \varphi(\delta, y)] \Delta\Omega(\delta, y) dy \,, \tag{4.2}$$

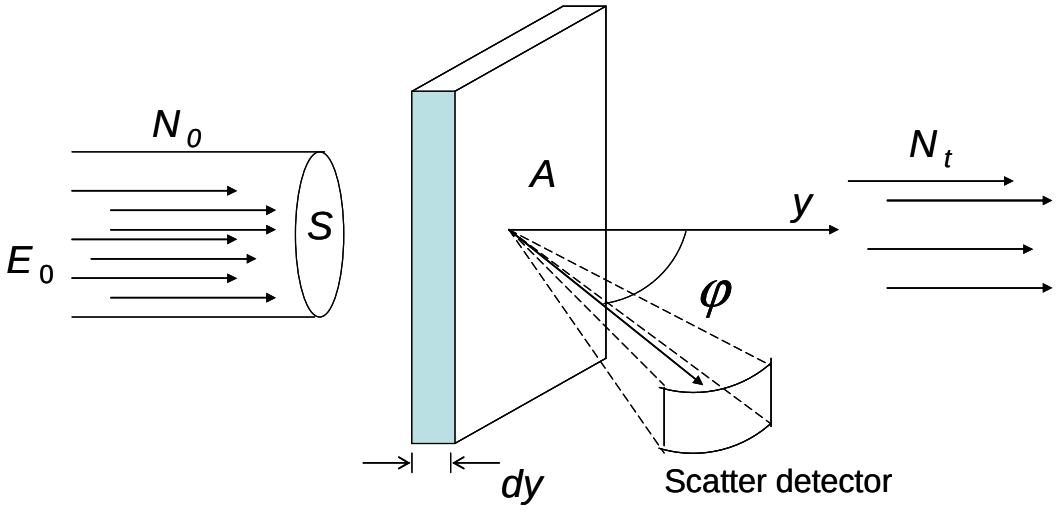

Figure 4.1. A beam with cross sectional area *S* consisting of N_0 x-rays with energy E_0 traversing a slab of material with linear attenuation coefficient μ and thickness *dy*. The cross sectional area of the slab is *A*, where *A*>*S*. As a result of photon interactions N_t photons pass through the slab while others are scattered at angle φ.

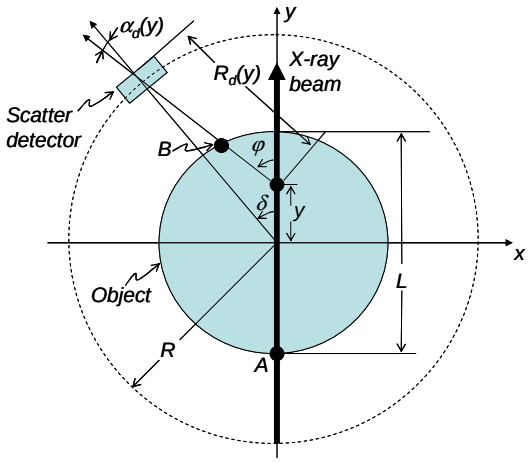

Figure 4.2. Geometry of first generation ISCT. An incident x-ray beam enters the object through point *A* until reaching a scattering point *y* from which it scatters by an angle φ. The scattered x-ray exits the object at point *B* and is measured by a detector located at a central angle δ and distance $R_d(y)$. *L* is the length of intersection of the beam and the object and *R* defines a circle where the scatter detector can be located. $\alpha_d(y)$ is the angle between the direction of the scattered photon and the normal to the detector surface.

where ρ_e is the *electron density* in electrons/cm^3 and $\varphi(\delta, y)$ indicates that the scattering angle is implicitly dependent on *y* and δ. Note that δ denotes the angle of location of the detector along a circle of radius *R* while φ is the scattering angle. According to Equation (4.2) the number of photons that reach a particular detector depends on the electron density as well as the KN cross section and solid angle. Since it is required that the number of scattered photons varies as a function of ρ_e variations along the material, and not of the relative position of the scattering centre with respect to the detector, the concept of a 4π detector is introduced. This

4π detector would measure the total number of scattered photons were it not for attenuation. Neglecting attenuation, one can calculate the number of photons scattered into the 4π detector when a line of material is traversed by an x-ray beam by integrating over the solid angle as

$$\begin{aligned} N_{SI} &= \int_0^L N_0 \rho_e(y) \left\{ \int_{4\pi} \frac{d_e\sigma_{KN}}{d\Omega}[E_0, \varphi(\delta, y)] d\Omega(\delta, y) \right\} dy \\ &= \int_0^L N_0 \rho_e(y)\, {}_e\sigma_{KN}(E_0)\, dy \\ &= N_0\ {}_e\sigma_{KN}(E_0) \int_0^L \rho_e(y) dy \end{aligned} \quad , \qquad (4.3)$$

where ${}_e\sigma_{KN}$ is the KN total cross section per electron. The total cross section can be calculated using

$${}_e\sigma_{KN} = 2\pi r_0^2 \left\{ \frac{1+\eta}{\eta^2} \left[\frac{2(1+\eta)}{1+2\eta} - \frac{\ln(1+2\eta)}{\eta} \right] + \frac{\ln(1+2\eta)}{2\eta} - \frac{1+3\eta}{(1+2\eta)^2} \right\}, \qquad (4.4)$$

where $\eta = E_0/m_0c^2$. The final form of Equation (4.3) shows that the 4π detector is capable of measuring ρ_e ray integrals. An example of a 4π detector is shown in Figure 4.3, which illustrates an x-ray beam traversing a volume whose scatter is measured in a spherical detector. The number of photons reaching the sphere is given by Equation (4.3) and is independent of both object location and beam direction. Incoherent scatter is symmetrical about the direction of the pencil beam and the 4π detector can be replaced by a ring of detectors located in the plane of the pencil beam (shaded area of Figure 4.3). These detectors

measure a fraction of the total number of scattered photons (Figure 4.4). Using this approach Equation (4.3) can be rewritten as

$$N_{SI} = \overline{F}\, N_0\, {}_e\sigma_{KN}(E_0)\int_0^L \rho_e(y)\,dy\,, \tag{4.5}$$

where $\overline{F}$ is a constant that denotes the fraction of scattered photons measured by the ring when compared with the 4π detector. For example, consider a semi-sphere (a 2π detector) whose bisection plane corresponds to the plane where the ring and pencil beam lie (shaded area of Figure 4.3). This 2π detector will measure a half of the total number of photons and $\overline{F}$ will equal 0.5. A constant $\overline{F}$ would allow backprojection to be used without correcting for the relative position of the scattering centre with respect to the detectors. Variations of $\overline{F}$ along the object will result in inaccuracies in the ρ_e image but the ring allows $\overline{F}$ to be approximated by a constant (section 4.3.2). The μ image can be reconstructed using first generation transmission CT formalism and is independent of $\overline{F}$.

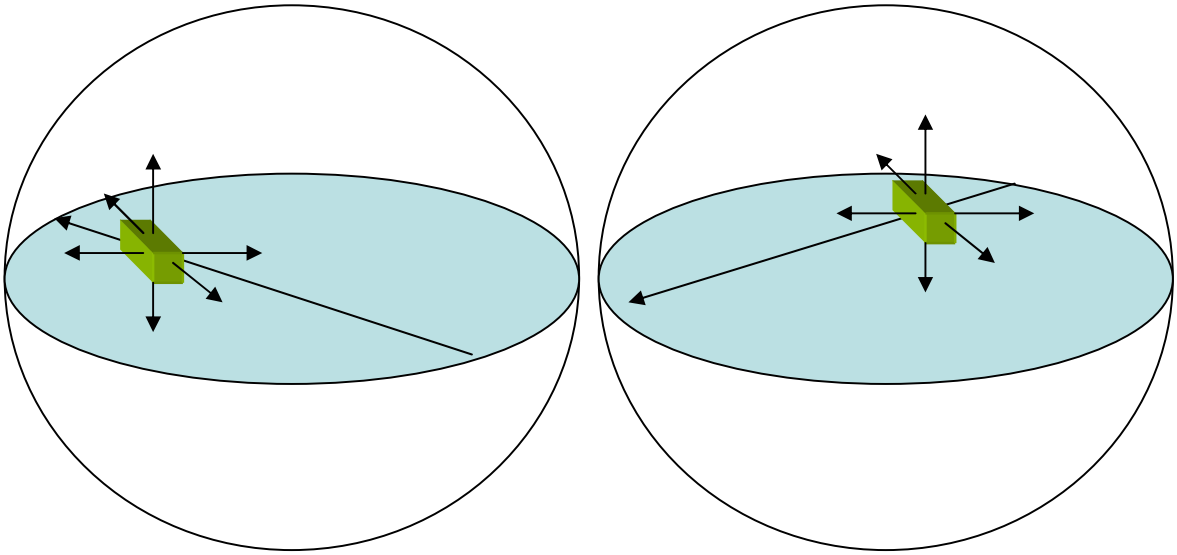

Figure 4.3. Spherical detector illustrating the concept of a 4π detector. The scatter measured by the sphere is the same irrespective of the voxel location and beam direction.

4.2.2. System description

The proposed system consists of a set of detectors arranged in a ring with a fixed x-ray source that produces a pencil beam coincident with the central axis of the ring [*y* axis of Figure 4.4(a)]. A detector located 180 degrees from the source measures the transmitted photons allowing for the simultaneous acquisition of a first generation transmission sinogram. The remaining detectors measure scattered photons and these are summed after correcting for attenuation to give the total scatter into the ring [i.e. Equation (4.5)]. In order to avoid confusion, sets of measurements and reconstructed images will be refered to as "primary" or "scatter" depending on whether primary (transmitted) or scattered photons were measured.

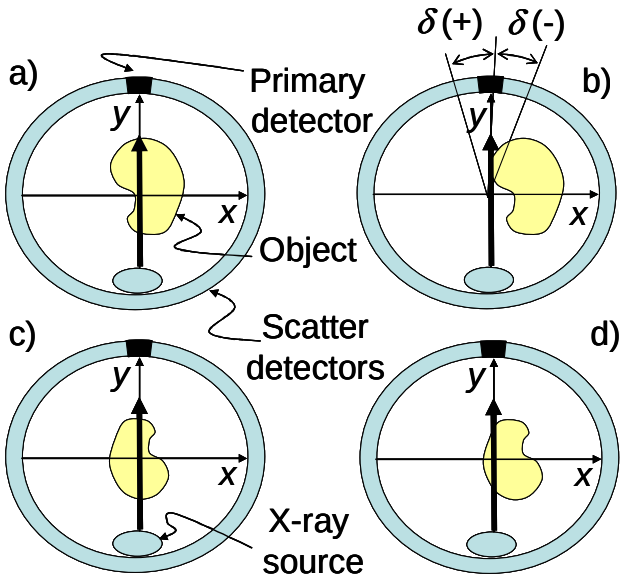

Figure 4.4. Proposed system with scanning required to produce both sinograms. (a) Object's original location. (b) An offset of the object. (c) A rotation of the object. (d) A rotation followed by an offset operation. δ is the central angle that identifies the scatter detector. Negative δ correspond to the right half of the ring while positive δ to the left half.

Although the proposed system resembles a fourth generation CT scanner, its data acquisition is that of a first generation scanner. In order to illustrate this, the acquisition procedure will be described as if the object were moving although this set of measurements could also be obtained by appropriate motions of the scanner. Figure 4.4(a) illustrates the location of the object at the beginning of the scan. Figure 4.4(b) illustrates a translation only operation of the object which allows for the acquisition of all ray integrals for one projection. Once a complete projection is achieved, the object is brought to its initial position [Figure 4.4(a)] and rotated [Figure 4.4(c)]. The rotated object can now be translated [Figure 4.4(d)] in the same way as described above, ultimately resulting in a complete sinogram acquisition.

4.2.3. Computer simulations

The EGSnrc MC code was used to simulate the geometry of Figure 4.4. The MC code was modified to catalogue photons into single or multiple scattered allowing two different MC sinograms to be created. An independent AN simulator was used to validate the MC simulation by comparing the single scatter sinograms. The AN simulated sinograms were also used to test the reconstruction algorithm in the absence of noise. The x-ray source was simulated as a mono-energetic 80 keV parallel beam with cross sectional dimensions of 0.12 cm x 0.12 cm. The beam sampled the entire object by translating the object every 0.12 cm. The radius of the detector ring was 35 cm which is large enough to encompass most breast sizes (most breast sizes are less than 20 cm in diameter [142]). The ring consists of D scatter detectors whose size was optimized based on the tradeoff between two factors: (1) number of measured photons and (2) accuracy in the attenuation correction calculation which requires the computation of equations (4.2) and (4.9) below. Both equations are calculated by assuming that scattered photons are measured at the centre of each detector. It is evident that increasing the detector size will measure a larger number of photons but reduce the accuracy of the attenuation correction. On the other hand, the attenuation correction will improve with smaller detector size but at the expense of reduced number of photons and hence greater noise. Using error propagation [143] the fractional uncertainty as a result of these competing effects was calculated for D = 180, 108, 36 and 20. The corresponding fractional uncertainties were of 0.051, 0.042, 0.032 and 0.048 respectively. These results show a minimum uncertainty for D=36 which correspond to detectors with dimensions of 6.1 cm x

6.1 cm. Each scattered photon was tracked until it reached the hypothetical geometrical location of the detector and the number of CT projections was set to 288. The scatter detectors modeled in this study are energy insensitive, such as the ones commonly used in CT. Energy sensitive detectors could be used to relate the energy of the scattered photon to the scatter location (for a mono-energetic beam) or range of location along the line (for a polychromatic beam). However the energy bin size would have to be carefully selected since a small bin, which provides the most precise scattering location, would have a reduced number of photons and hence large noise. The same information (electron density) can be obtained using the approach of this thesis without requiring the complexity and cost of incorporating energy discriminating detectors.

Figure 4.5 shows slices of the phantoms simulated in this study. These images are displayed using window levels that cover the entire range of values of the corresponding image. Phantom A is shown in the first row and consists of uniform breast tissue with dimensions of 10 cm x 10 cm. This virtual phantom also contains bone inhomogeneities located at different locations in μ and ρ_e. The μ values of breast and bone (whose ρ_e is almost double that of breast) were taken from the data provided by Hubbell and Seltzer [144]. The ρ_e was derived from the same reference data using Equation (3.4). The goal of this phantom is to test if the algorithm is able to obtain the correct ρ_e by starting with an incorrect initial estimate. To fulfill this purpose the presence of noise was neglected by using analytically simulated sinograms. In addition, the material composition of the object was known a-priori to correct accurately for attenuation. The second row of Figure 4.5 shows phantom B. This phantom consists of a cylinder with 14 cm diameter and 10.5 cm height. These dimensions are

typically used to simulate breasts [93]. Phantom B was used for two reasons: it shows the practical performance of the algorithm with heterogeneities and it can be machined for future experiments. The plastics that make up the regions of interest (ROI) of the phantom are listed in Table 4.1 along with their physical characteristics.

The MC code was validated by simulating a projection of phantom B and comparing the number of single scattered photons. The number of histories in the MC simulation was 1,771,800 incident photons which results in a mean MC uncertainty of 3% and a MGD of 9.6 mGy. The validated MC code was used to simulate the scan for phantom B in order to neglect possible effects from heterogeneities. A scan resulting in a 4 mGy *MGD* was also simulated by reducing the number of histories to 737,735. This number was selected based on dose studies that quantified the *MGD* due first generation CT to be described in Chapter 5.

4.2.4. Fraction determination

For an infinitesimally small scattering point, $\overline{F}$ reduces itself to F which can be calculated by integrating the differential KN cross section over the solid angle subtended by the ring as

$$F(y) = \frac{N_0\, n_e \int\limits_{ring} \frac{d_e\sigma_{KN}}{d\Omega}[E_0, \varphi(\delta, y)]d\Omega(\delta, y)}{N_0\, n_e \int\limits_{4\pi} \frac{d_e\sigma_{KN}}{d\Omega}[E_0, \varphi(\delta, y)]d\Omega(\delta, y)} = \frac{\int\limits_{ring} \frac{d_e\sigma_{KN}}{d\Omega}[E_0, \varphi(\delta, y)]d\Omega(\delta, y)}{{}_e\sigma_{KN}(E_0)}, \qquad (4.6)$$

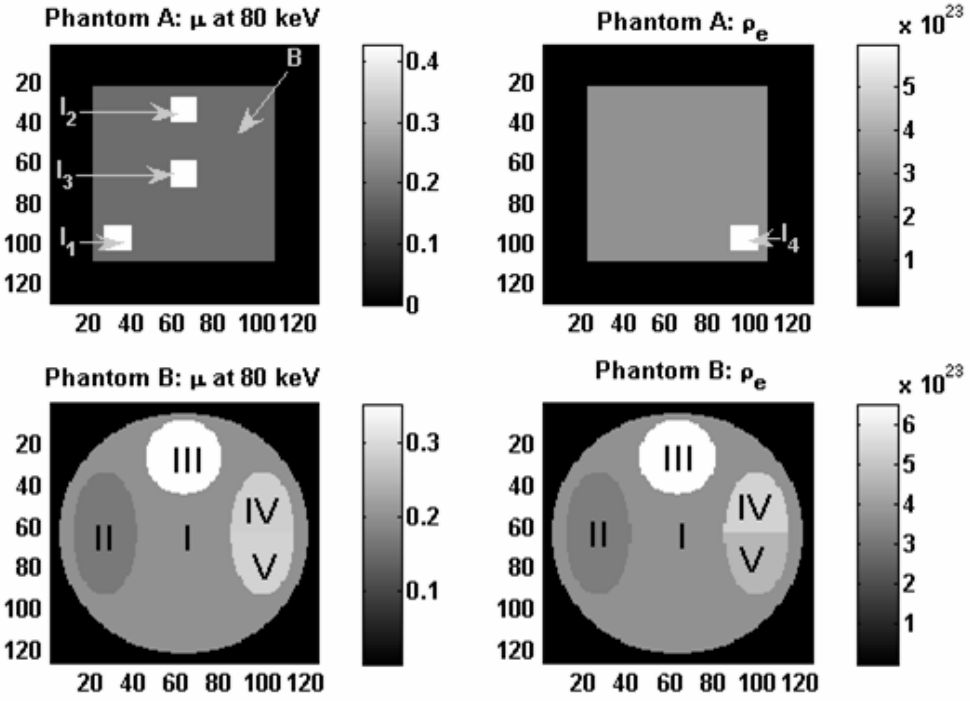

Figure 4.5. Definitions of Phantoms A (1st row) and B (2nd row) in terms of their μ at 80 keV (1st column) and ρ_e (2nd column). The arrows indicate different ROI for phantom A. The roman characters correspond to the different materials that make up Phantom B and are listed in Table 4.1. The units of μ are (cm^{-1}) whereas those of ρ_e are (electrons/cm^3).

Table 4.1. List of materials that make up phantom B along with their corresponding values of electron density, effective atomic number ($\overline{Z}$) and linear attenuation coefficient at 80 keV.

Material	$10^{23}\rho_e$ (electrons/cm^3)[a]	$\overline{Z}$ [b]	μ at 80 keV (cm^{-1})[c]
I: A-150 tissue-equivalent plastic	3.73	5.5	0.2032
II: Polyethylene	3.19	5.6	0.1695
III: Teflon	6.50	8.5	0.3672
IV: C-552 Air-equivalent plastic	5.30	7.6	0.2927
V: B-100 Bone-equivalent plastic	4.61	11.8	0.3010

[a]Values of ρ_e were calculated using $\rho_e = \rho N_A (Z/A)$, where N_A is Avogadro's number, ρ is the material density, Z is the atomic number and A is the atomic weight of the material. Values of ρ and the Z/A ratio were taken from Hubbell & Seltzer [144].

[b] $\overline{Z}$ was calculated using $\overline{Z} = \sqrt[b]{a_1 Z_1^b + a_2 Z_2^b + ... + a_n Z_n^b}$ where the a_i is the number of electrons per gram of element Z_i and n is the number of elements. A value of $b = 3.1$ was employed as was used by Busono and Hussein [24].

[c]Values of μ taken from Hubbell & Seltzer [144].

where it can be seen that F is independent of material. In order to integrate the numerator of Equation (4.6) one must remember that the ring is made of D square detectors. This geometry complicates the analytical integration of the numerator in Equation (4.6) using spherical coordinates. Instead numerical integration was used according to

$$\int_{ring} \frac{d_e\sigma_{KN}}{d\Omega}[E_0,\varphi(\delta,y)]d\Omega(\delta,y) = \sum_{d=1}^{D} \frac{r_0^2}{2}\left[\frac{E_{s,d}(y)}{E_0}\right]\left[\frac{E_0}{E_{s,d}(y)} + \frac{E_{s,d}(y)}{E_0} - \sin^2\varphi_d(y)\right]\left[\frac{a}{R_d^2(y)}\cos\alpha_d(y)\right], \quad (4.7)$$

where $\varphi(\delta)$ is written as φ_d to represent the discrete integration. The last term in brackets corresponds to the solid angle and the other terms to the KN cross section. r_0 is the classical electron radius and has a value of 2.818 x 10^{-13} cm. $E_{s,d}(y)$ is the energy of a photon scattered from point y (Figure 4.2) into detector element d with a scattering angle $\varphi_d(y)$ and located a distance $R_d(y)$ away. Each detector has an area a and $\alpha_d(y)$ is the angle between the vector normal to the detector surface and direction of the scattered photon. The summation over all D detectors is made in order to account for the complete ring. The values of the differential cross section and solid angle will change depending on the location of the point along the y axis (which coincides with the primary beam of Figure 4.4). As a result, the value of F will also change along the y axis as illustrated in Figure 4.6. For the acquisition geometry, the location of a point along the y axis will change with projection angle θ according to

$$y(\theta) = r\cos(\phi - \theta), \quad (4.8)$$

where (r,ϕ) are the polar coordinates of the point at the beginning of the scan. This equation shows that as the object rotates, a specific volume of material will interact with the beam at different locations along the y axis. As a consequence, the fraction of the total number of photons scattered into the ring from this volume will vary with projection angle.

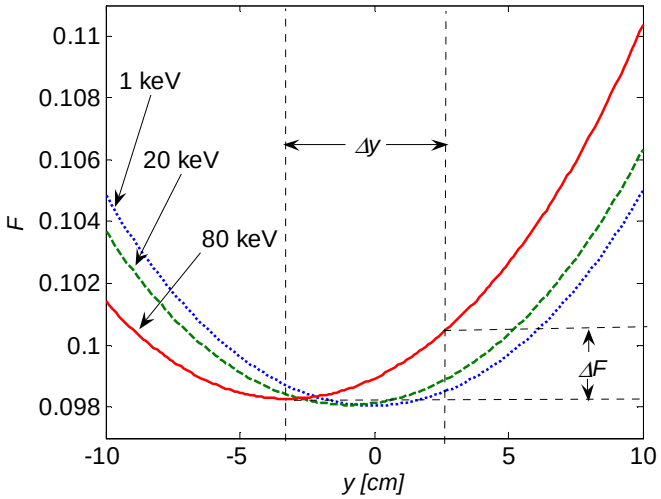

Figure 4.6. F as a function of location on the y-axis. Δy is the variation of a point location along the y-axis for a complete scan. ΔF is the resulting variation of the fraction of scattered photons measured by the ring.

For a point located at the centre of rotation (r = 0), the variation in its location along the y axis (denoted by Δy) during the scan will be zero. For this point F will remain constant and equal to the value at the centre (F_0). Figure 4.6 illustrates that as the point moves off-centre (r>0) Δy increases and results in a corresponding ΔF. During a complete scan, multiple beams from different projections will intersect with this point resulting in a mean value of F ($\overline{F}$). $\overline{F}$ is dependent on the FOV and can be extracted from ideal scatter sinograms. An

ideal scatter sinogram can be calculated analytically using Equation (4.2) [see for example Figure 4.10(a)]. Adding the ideal scatter sinograms over all detectors allows Equation (4.5) to be used to obtain the value of $\overline{F}$ that gives the correct ρ_e for each pixel within the object image. The resulting $\overline{F}$ image can be used to calculate a single value of $\overline{F}$ for the corresponding FOV along with its standard deviations. Phantom B was used to simulate ideal scatter sinograms and from these calculate the correct values of $\overline{F}$.

Ideal scatter sinograms can not be obtained in practice and a feasible method to estimate $\overline{F}$ was developed. The problem is approached by analytically calculating F at different locations along the y axis according to Equation (4.6). These values are grouped into Δy intervals which correspond to specific FOVs. The mean of these values is calculated and results in a look-up table that can be used to select $\overline{F}$ for a particular FOV.

4.2.5. Attenuation correction reconstruction algorithm

Equation (4.2) corresponds to the number of photons reaching the detector in the absence of attenuation. In practice, attenuation is always present and the number of photons reaching a detector is reduced. To account for attenuation, Equation (4.2) can be generalized to account for the attenuation of single scattered photons as follows

$$N_s(\delta) = \int_A^{A+L} N_0 e^{-\int_A^y \mu(E_0,y')dy'} \rho_e(y) \frac{d_e\sigma}{d\Omega}[E_0, \varphi(\delta,y)] \Delta\Omega(\delta,y) e^{-\int_y^B \mu(E_s,\gamma)d\gamma} dy, \qquad (4.9)$$

where E_s is the energy of the photon being scattered at an angle φ from its incident direction and γ is the path that follows from the point of interaction y to the detector. The first exponential in Equation (4.9) represents the pre-scatter attenuation (from point A to point y in Figure 4.2). The second exponential accounts for the reduction of photons from the scattering centre to the scatter detector (from point y to point B in Figure 4.2).

In the context of the ISCT theory presented in this work, all measurements in each of the scatter detectors must represent Equation (4.2). For this reason *attenuation correction factors* (ACFs) are introduced and applied to each scatter detector in an iterative algorithm that works as follows. First an image of $\mu(E_0)$ is reconstructed using the primary detector to measure those photons that do not undergo any interactions and therefore are not scattered. This primary image is then used to obtain an initial estimate of the ρ_e by using the $\rho_e/\mu(E_0)$ ratio for water. Using the $\mu(E_0)$ values and the current k-th estimate of electron density (ρ_e^k) Equation (4.2) and Equation (4.9) are calculated and their ratio is computed to yield the ACF of each detector at the specific point in the sinogram. The measurements of the scatter detectors are multiplied by their corresponding ACFs and the result is summed in order to obtain Equation (4.5). Since this is done for every rotation and translation of the system, a scatter sinogram is obtained which can then be reconstructed by the FBP algorithm to yield an ρ_e image. The reconstructed image can be used as the new estimate of ρ_e and the process repeated. A flow diagram of the iterative algorithm is shown in Figure 4.7. The differences in the ρ_e reconstructions between successive iterations (k+1 and k) were quantified in terms of the mean relative squared deviation (MRSD) defined by Equation (4.10)

$$MRSD = \frac{1}{J}\sum_{j=1}^{J}\left(\frac{\rho_{e,j}^{k+1} - \rho_{e,j}^{k}}{\rho_{e,j}^{k}}\right)^2 , \qquad (4.10)$$

where $\rho_{e,j}^{k+1}$ is the electron density of pixel j at iteration k+1 and J is the total number of image pixels. The following two conditions were set as stopping criteria: (1) if there is an increase in the MRSD with respect to the previous iteration or, (2) when the value of the MRSD falls below 10^{-6} which corresponds to an average difference of $\sqrt{10^{-6}} = 10^{-3}$ (or 0.1%).

Special attention was paid to the second exponential of Equation (4.9) which accounts for the post-scatter attenuation. As a photon is incoherently scattered, its energy E_s changes depending on the scattering angle, causing the value of $\mu(E_s)$ to differ from the reconstructed value of $\mu(E_0)$. Therefore it was necessary to find a way to estimate $\mu(E_s)$ given E_s and $\mu(E_0)$. This was achieved using Equation (4.11) which is derived in Appendix A:

$$\begin{aligned}\mu(E_s) = {} & (0.029)[\mu(E_0)]^3(E_s - E_0) \\ & - (0.067)[\mu(E_0)]^2(E_s - E_0) \\ & + [(0.007)(E_s - E_0) + 1]\mu(E_0)\end{aligned} , \qquad (4.11)$$

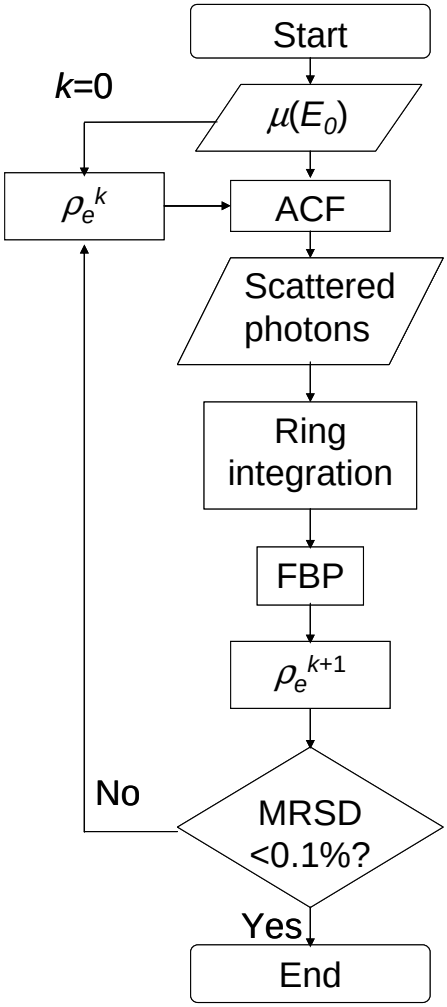

Figure 4.7. Flow diagram of the iterative algorithm used to reconstruct images of ρ_e. The algorithm was implemented using the 'edrec.m' code found in Appendix B.

where the unit of μ is cm^{-1} and that of energy is keV. This ISCT reconstruction algorithm was used to reconstruct images from sinograms derived from measurements of single scattered photons and from single and multiply scattered photons. This was carried out since

the former situation is based on the measurements required by Equation (4.5) while the latter (multiple and single scatter) is based on the measurements expected in practice.

4.3. *Results*

4.3.1. MC validation

Figure 4.8 shows the distribution of single scattered photons along the ring of detectors calculated using MC (steps with error bars) and AN simulations (solid lines). Each scatter detector is labeled by the central angle (δ) as defined in Figure 4.4. Negative δ corresponds to the right half of the ring while positive δ corresponds to the left half. The graph shows the distribution of photons for two beams: (i) a beam going through the centre of phantom B [corresponding to the object location of Figure 4.4(a)] and (ii) a beam tangential to phantom B [corresponding to the object location of Figure 4.4(b)]. This figure shows that the analytical simulation was able to match the MC simulation, with average errors of 1.3% and 1.2% for the central and tangential beams respectively. The average statistical fluctuations of the MC simulations for the central and tangential beams were 2.9% and 5.8% respectively. Figure 4.9 shows MC and AN generated sinograms of single KN scatter. The sinograms correspond to two arbitrarily chosen detectors, δ = -175 degrees and δ = -95. The mean error for the complete projection of the phantom was 1.1% with a mean MC uncertainty of 3.2%. Using the AN simulation a mean uncertainty of 3.2% can be expected which suggest that the number of histories was appropriate.

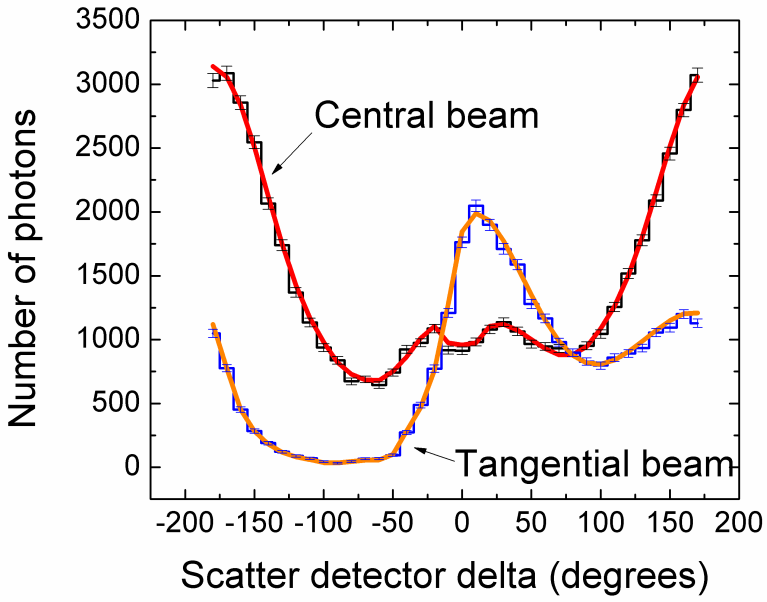

Figure 4.8. Distribution of single scattered photons along the ring using MC (discrete steps with error bars) and analytical simulations (solid lines). The scatter detectors are indexed by the central angle δ. δ is defined as the angle between the line joining the centre of the scanner and the primary detector and the line from the centre of the scanner to each scatter detector (Figure 4.4).

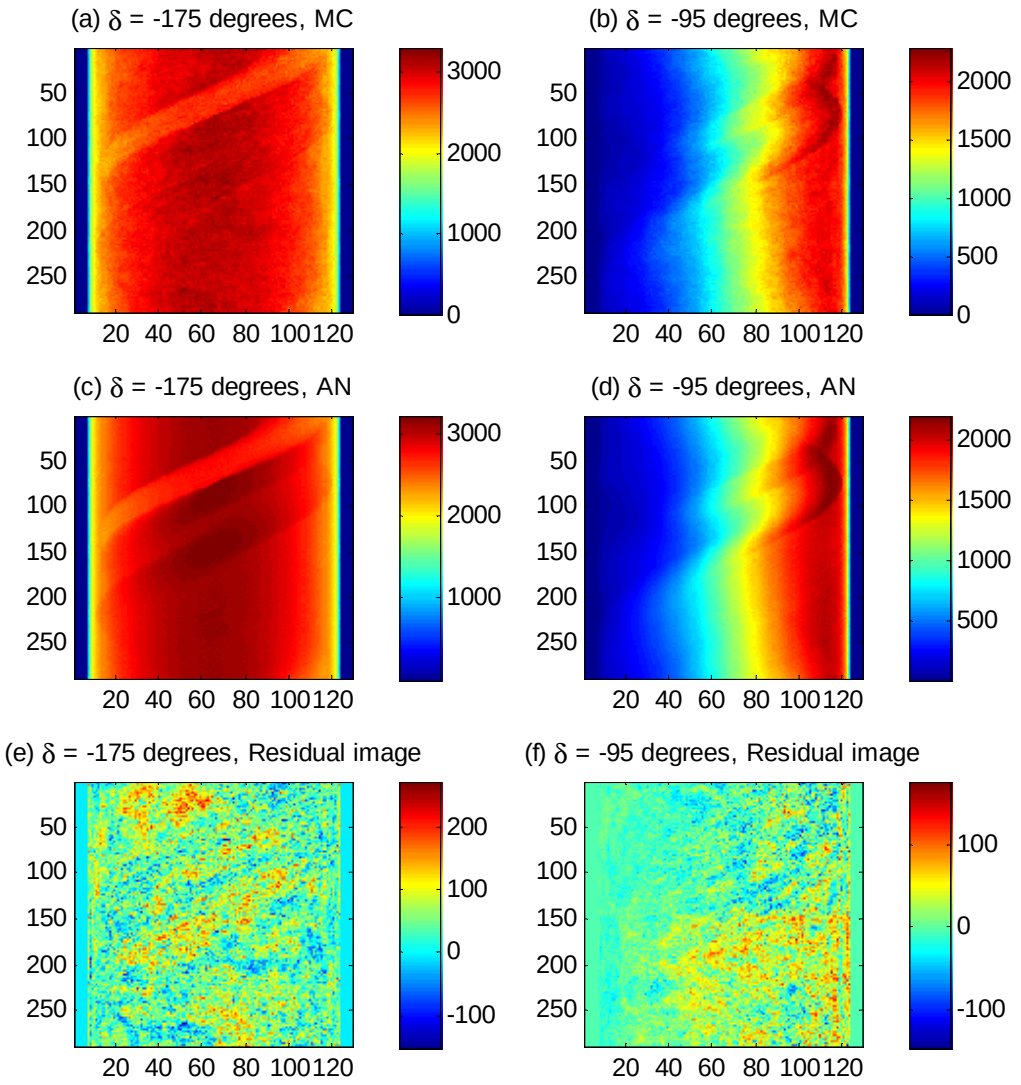

Figure 4.9. Single KN scatter sinograms generated by either MC (first row) or AN (second row) simulations. The figure shows sinograms for two arbitrarily chosen detectors: δ = -175 degrees (first row) and δ = -95 degrees (second row). Images of the third row are residual images obtained by subtracting the MC sinograms from the AN ones. The units of all images are number of photons.

4.3.2. $\overline{F}$ factor

Figure 4.10 shows the procedure used to obtain the correct values of $\overline{F}$. Figure 4.10(a) shows ideal scatter sinograms for detectors with δ = -175 degrees and δ = -95 degrees. These detectors are arbitrarily chosen and correspond to those of Figure 4.9. The sinograms correspond to simulations of phantom B with 15 cm size and 80 keV energy. Figure 4.10(b) shows the integrated scatter sinogram which is obtained after summing over all δ. This integrated sinogram can be reconstructed using FBP and divided by $N_0\, _e\sigma_{KN}(E_0)\ \vec{\rho}_e$, where $\vec{\rho}_e$ is the true electron density image. This process results in an approximately constant $\overline{F}$ image as shown in Figure 4.10(c). Figure 4.10(d) shows a distribution of Figure 4.10(c) whose mean is plotted on Figure 4.11. The standard deviation of the distribution is shown as the error bar. Figure 4.11 also shows the results of phantom B with 1 cm, 5 cm, 10 cm, 15 cm and 20 cm diameter. An additional sinogram was simulated for phantom A (with a 10 cm FOV). The corresponding correct $\overline{F}$ agreed within 1% with that of phantom B in accordance with Equation (4.6). This process can not be done in practice since $\vec{\rho}_e$ is unknown.

Figure 4.6 illustrates the variation of *F* as a function of location along the *y*-axis. *F* is plotted as a function of *y* for 1 keV, 20 keV and 80 keV. These values are grouped for different Δy intervals whose means yield the *calculated* values of $\overline{F}$. Figure 4.11 shows the variation of the calculated values of $\overline{F}$ as a function of phantom size. Note that these can be easily calculated with appropriate knowledge of the geometry, x-ray energy and FOV being

imaged. This variation is shown from 20 keV to 80 keV, which spans the range of diagnostic mean energies.

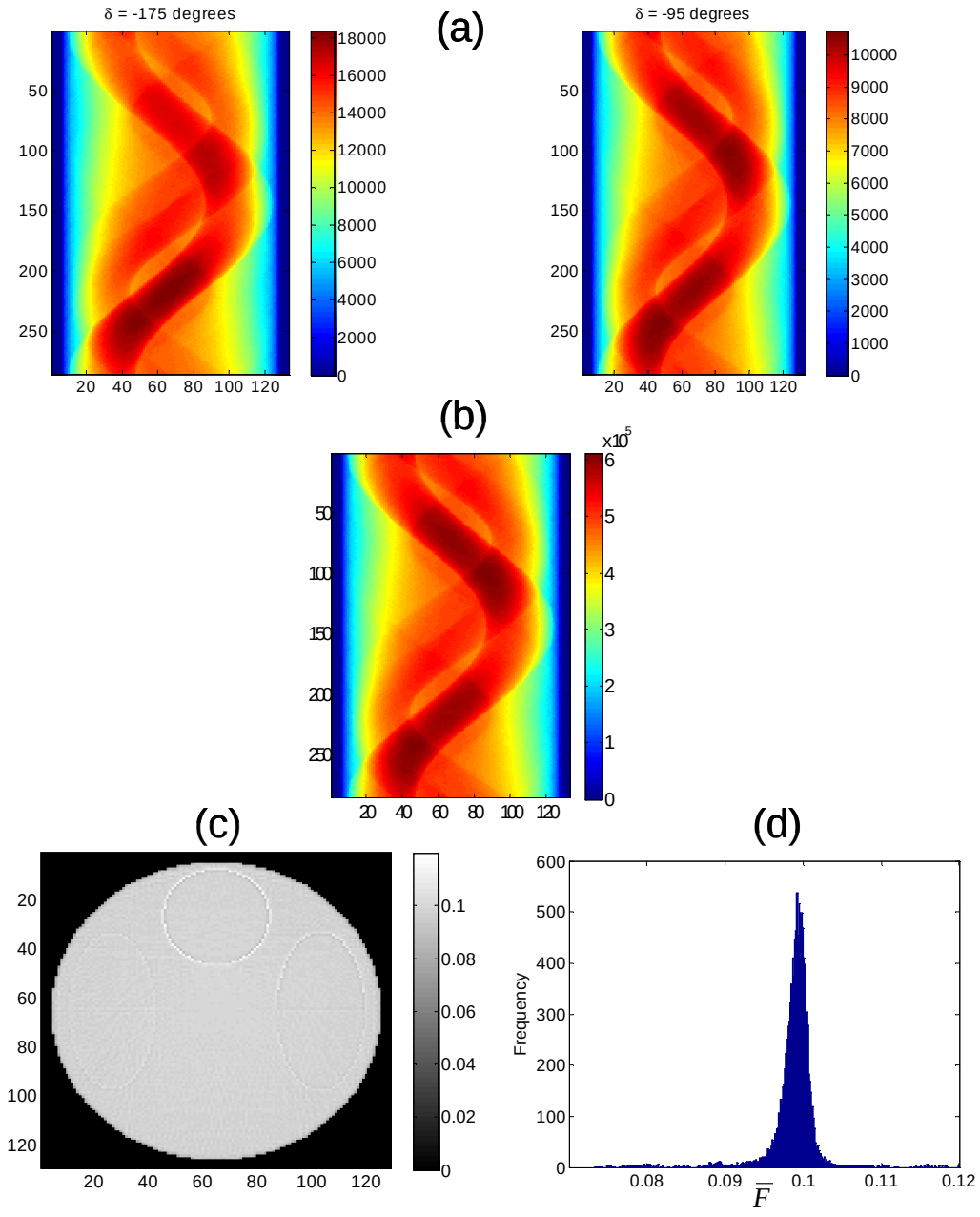

Figure 4.10. Steps followed to calculate the correct $\overline{F}$.

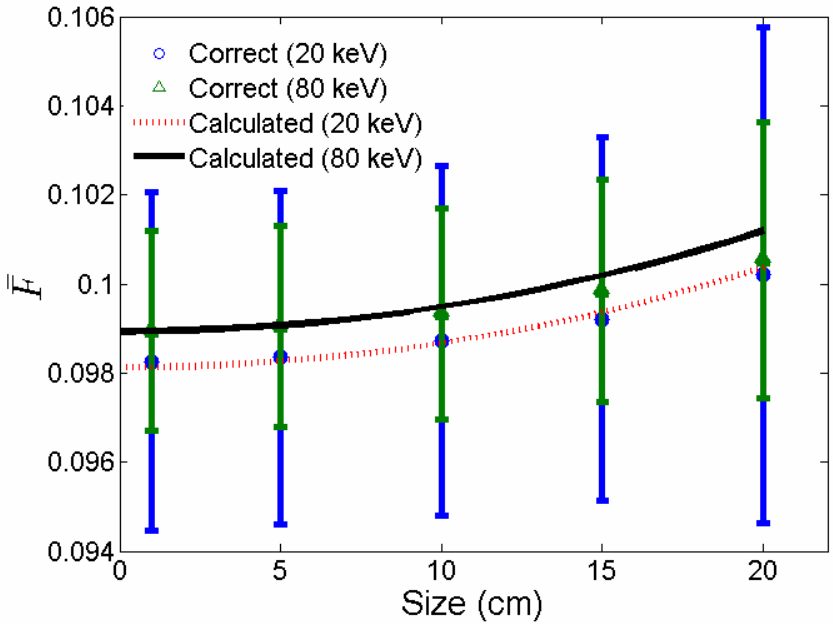

Figure 4.11. Correct and calculated values of $\overline{F}$ as a function of phantom size for 20 keV and 80 keV. Correct values of ($\overline{F}$) are derived from ideal scatter sinograms of phantoms with sizes of 1 cm, 5 cm, 10 cm, 15 cm and 20 cm. The error bars indicate the standard deviation for each of the correct ($\overline{F}$).

4.3.3. Image reconstructions

Figure 4.12 shows ρ_e images of phantom A at different stages of the reconstruction. This figure shows the evolution of the algorithm from the initial estimate [Figure 4.12(a)] to the final image [Figure 4.12(h)]. Figure 4.13 shows the change in the mean values of electron density for the five different ROI together with their standard deviations. The horizontal lines correspond to the correct values for each ROI. This figure shows that the initial values of ρ_e are overestimated by a factor as large as 2.3 but that this procedure enables the correct ρ_e to be calculated with a mean error of -2%. The computation time for each of the iterations was of ~9 hours and 40 minutes using an Intel® Xeon ® processor at 2.66 GHz.

Figure 4.14 shows the primary [Figure 4.14(a)] and scatter [Figure 4.14(b)] images for the plastics phantom. The scatter image of Figure 4.14(b) was derived from single KN scatter sinograms in accordance with the model of section 4.2.1. The electron density image of Figure 4.14(b) has errors that range from -2% to -3% for the different plastics with uncertainties that range from 3% to 4%. A reconstruction from primary photons yields the linear attenuation coefficient of the phantom with mean errors for any ROI within -1%. Figure 4.14(c) shows the final image of electron density obtained from scatter sinograms which include multiple scatter. While qualitatively correct the reconstructed values of ρ_e are a factor 2 larger than the correct ones.

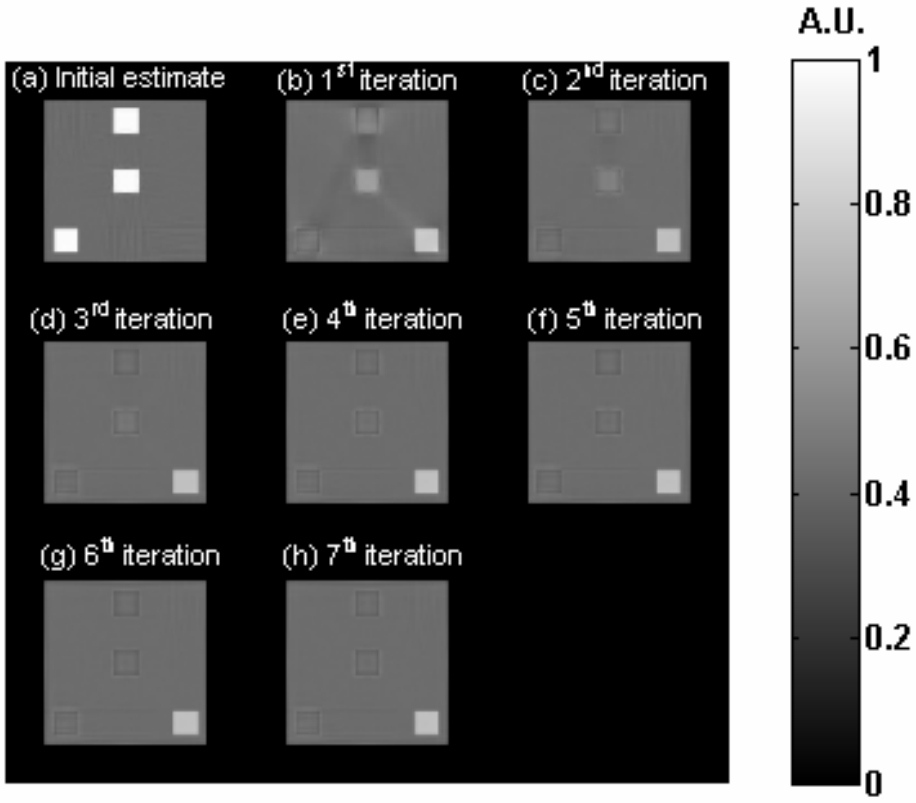

Figure 4.12. Electron density reconstructions of Phantom A for different steps of the iterative algorithm. Figures 9(a) to 9(h) correspond to the initial estimate, 1st, 2nd, 3rd, 4th, 5th, 6th and 7th iterations respectively. All images are displayed using the same window level which was normalized to the maximum value of ρ_e among all iterations.

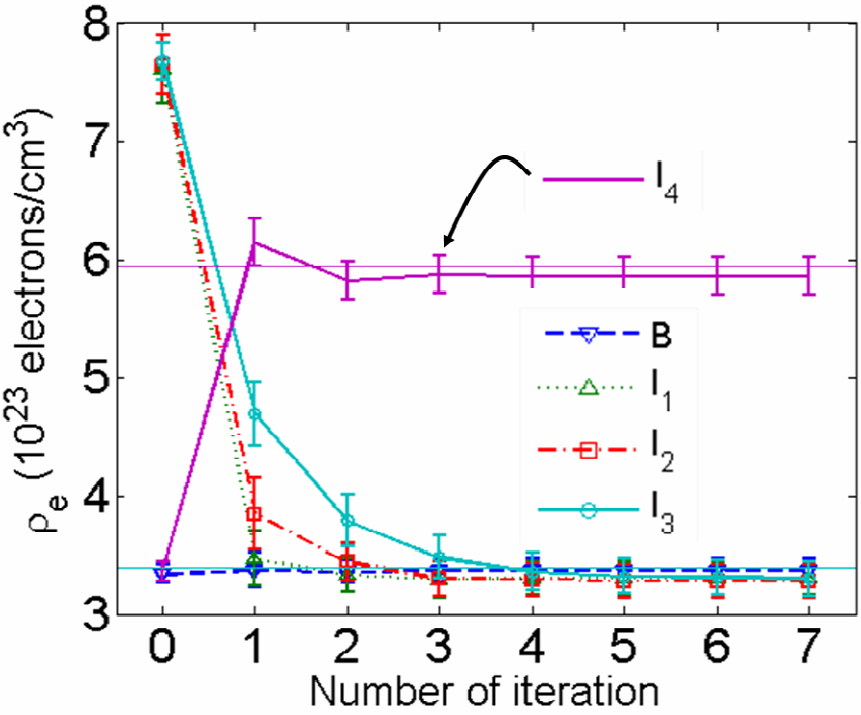

Figure 4.13. The variation of electron densities for each material of phantom A as the iterations proceed. Horizontal lines correspond to the correct values. Errors bars are used to indicate the standard deviations for each ROI. The definition of each ROI is shown in Figure 4.5.

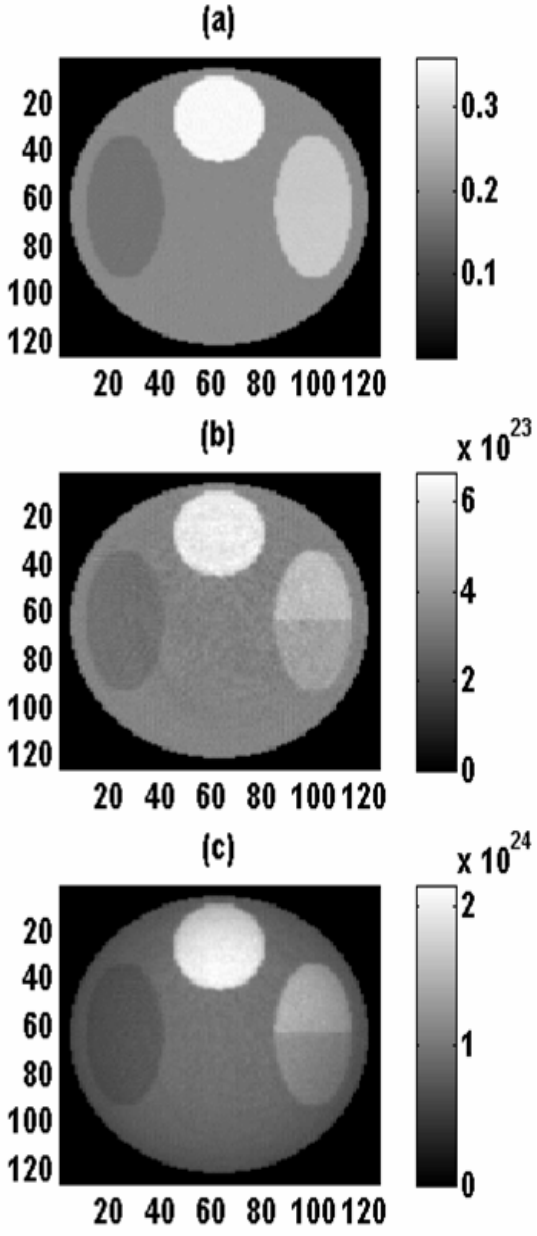

Figure 4.14. Reconstructed images of the phantom B. (a) μ image in cm^{-1}, (b) ρ_e image in electrons/cm^3 and (c) ρ_e image including multiple scatter in electrons/cm^3.

4.4. *Discussion*

4.4.1. $\overline{F}$ factor determination

Neglecting attenuation (as assumed in the 4π model) two competing factors determine the number of photons that reach a scatter detector: the solid angle and the KN cross section. Figure 4.6 shows that as the point moves towards the source (negative *y* axis) the number of detected photons increases (*F* large) as a result of back-scatter and the large solid angle subtended by the ring. As the point moves to the centre ($y = 0$) of the scanner fewer photons reach the detector due to the decrease of the solid angle subtended by the back-scattered detectors (*F* decreases in Figure 4.6). For 80 keV it is found that at $y \approx -3.3$ cm the solid angle subtended by the forward scatter detectors and the larger probability of forward scattering cause an increase in the number of measured photons (*F* increases). The curve is not symmetric due to the non-symmetric shape of the KN cross section. Figure 4.6 shows that as the energy is reduced, the so called "peanut" symmetry [145] of the KN cross section is recovered and *F* varies symmetrically along *y* as illustrated for the 1 keV curve.

That independence of *F* from material composition can be explained by recognizing that one is only interested in changes in the scatter distribution with respect to the 4π detector. *F* corrects for the geometric differences between the 4π detector and the ring. Therefore any change in material composition and shape will change the scatter distribution of both the 4π

detector and the ring. The reconstruction results of phantoms A and B support this argument since no effect was found for square and circular shapes of different materials (Table 4.2).

Figure 4.11 shows that the method of calculating $\overline{F}$ is accurate in the diagnostic energy range with maximum errors of 0.2% and 0.7% at 20 keV and 80 keV respectively. The change in $\overline{F}$ between the two energies is less than 1% indicating small energy dependence. This small dependence can be explained by recognizing that a change in energy affects both the numerator and denominator in Equation (4.6). For the energy range of interest, reducing the energy from 80 keV to 20 keV causes the numerator and denominator to increase by 19% and 20% respectively. This causes the value of F_0 to change by less than 1% which results in $\overline{F}$ remaining approximately constant. This implies that under the KN approximation one can assume a constant $\overline{F}$ which allows Equation (4.5) to be generalized for polychromatic spectra. As the energy decreases the probability of incoherent scatter will be reduced and Equation (4.6) will have to be modified by the incoherent scatter function (to be described in section 5.2.3). In section 4.2.4 it was stated that the value of $\overline{F}$ is dependent on the FOV. Intuitively one would expect to find a radial dependency of $\overline{F}$ within a phantom. The results, however, showed no significant variation between pixels at different distances from the centre [Figure 4.10(c)]. This can be explained by noting that for small FOVs the variation ΔF is approximately linear about F_0 (see Figure 4.6). This quasi-linear variation results in values of F_0 being over- and underestimated by approximately the same amount and canceling out. For larger FOVs the linear variation is no longer valid as a result of the change in the sign of dF/dy for negative values of y. Therefore the correct value of $\overline{F}$ is expected to increase with FOV in accordance with Figure 4.11. For larger FOVs the radial dependency should be more

noticeable. This effect is reflected in Figure 4.11 where the fractional uncertainties of the correct $\overline{F}$ increase with increasing FOV from 4 % to 6 % at 20 keV and from 2% to 3% at 80 keV. The change of $\overline{F}$ over a 20 cm FOV would introduce a 2% inaccuracy in electron density with breast size changes. However, if this inaccuracy is small in comparison to the actual ρ_e contrast, then a constant $\overline{F}$ could be assumed.

4.4.2. Image reconstructions

The reconstruction of phantom A demonstrates the weak dependence of the algorithm on the initial estimate of electron density. Defining the initial estimate of ρ_e equal to the primary image results in three false inhomogeneities. This estimate also ignores the presence of the true electron density inhomogeneity. After the first iteration [Figure 4.12(b)] the errors of the vanishing false inhomegeneities range from 3% to 39% while that of the true one, already visible, is only of 3%. It is evident from Figure 4.12 that as the iterations proceed, the false inhomogeneities disappear while the background and true inhomogeneity approach their correct values. The final image still shows the residual of the false inhomogeneties, however, the errors in ρ_e are ≈ -3% while that of the true one is ≈ -2%. These results illustrate that the algorithm reconstructs an image based on the scattered photons and is only weakly dependent on the initial estimate. This is an advantage of the proposed ISCT algorithm over iterative ones where selection of reconstruction parameters can potentially affect the solution. While the computation time per iteration seems large, the burden of the reconstruction is in the calculation of the ACF which is required by any ISCT reconstruction algorithm (iterative or analytical). Figure 4.15 shows an image of phantom B reconstructed without attempting to

correct for attenuation (sinograms of Figure 4.9). The lack of correction results in a severe cupping artifact as observed by Hogan [140]. This artifact reflects the larger attenuation of photons scattered at the centre and the reason why it must be corrected. Further reduction in time can be envisioned by using coding techniques like vectorization and parallelization on GPU hardware [146, 147].

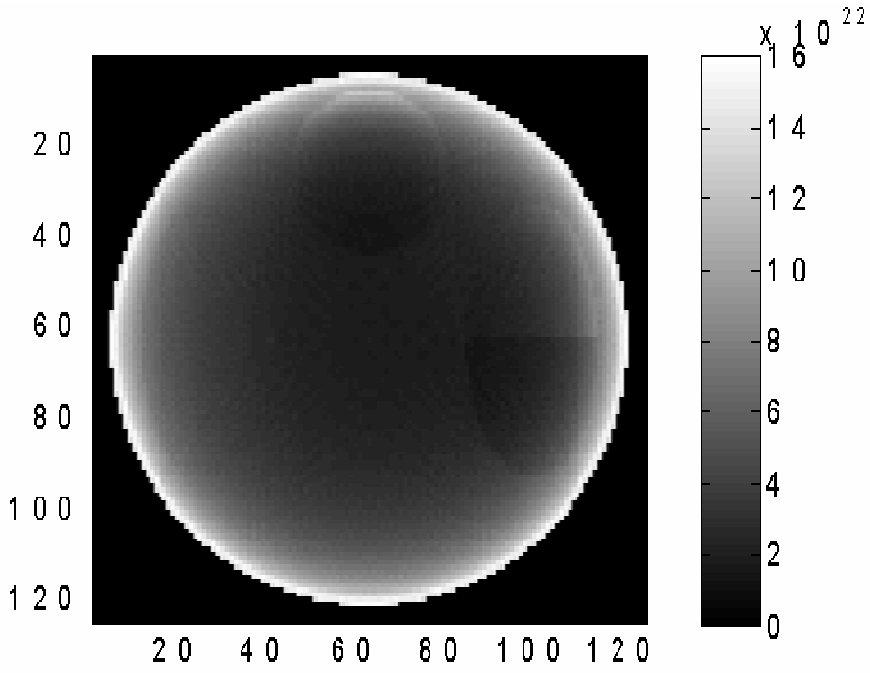

Figure 4.15. Electron density reconstruction without correction for attenuation. The image window is set to display the minimum and maximum values in the image. The image has units of (electrons/cm^3).

Figure 4.14(a) illustrates the difficulty of identifying the C-552 and B-100 plastics using an image of μ alone. These two materials are easily resolved in the ρ_e image due to the larger

difference in electron density (~13%) contrast when compared to that of μ (~3%). The reconstructions from single scatter sinograms starts, with the exception of B-100 plastic, with errors in electron density ranging from -1% to -5%. The electron density of B-100 plastic is overestimated by 14%. This is because the scaling factor used to obtain ρ_e^0 works well for materials with characteristics similar to those of water ($\overline{Z}$ =7.5 and ρ_e =3.34 $\times 10^{23}$ electrons/cm^3) but not for the B-100 plastic, whose atomic number is substantially larger ($\overline{Z}$ =11.8). After the first iteration the electron densities of all materials are within (-1% and -3%) one standard deviation and stay within it until the end of the reconstruction. Figure 4.14(b) shows the final ρ_e image for which the true contrast has been recovered.

There was an underestimation in the ρ_e reconstructions without sufficient zero padding. The MC generated sinograms initially consisted of the same number of voxels that made the phantom (125). On the other hand, the number of translations of the analytically generated sinograms was approximately equal to the number of projections. This resulted in reconstructions whose ρ_e values have errors of -1%. A sensitivity analysis shows that the difference in the amount of zero padding between MC and AN sinograms are the cause of the ρ_e underestimation. The same deterministic error was found in the reconstructions of a homogeneous breast phantom (shown in Figure 4.16 and which we will refer to as phantom C) of the same size. This issue was addressed by zero padding translations of the MC sinograms to the same number as those of the AN ones. Finally, the same error is found in reconstructions of the plastic phantom using an incident number of histories which differs by a factor of 2.4 (the number of histories used for the MC validation and that needed to achieve a 4 mGy dose). This indicates that the algorithm is quite robust to the noise levels expected in

breast examinations. Table 4.2 summarizes the reconstruction results for different phantoms and method used to simulate the sinogram.

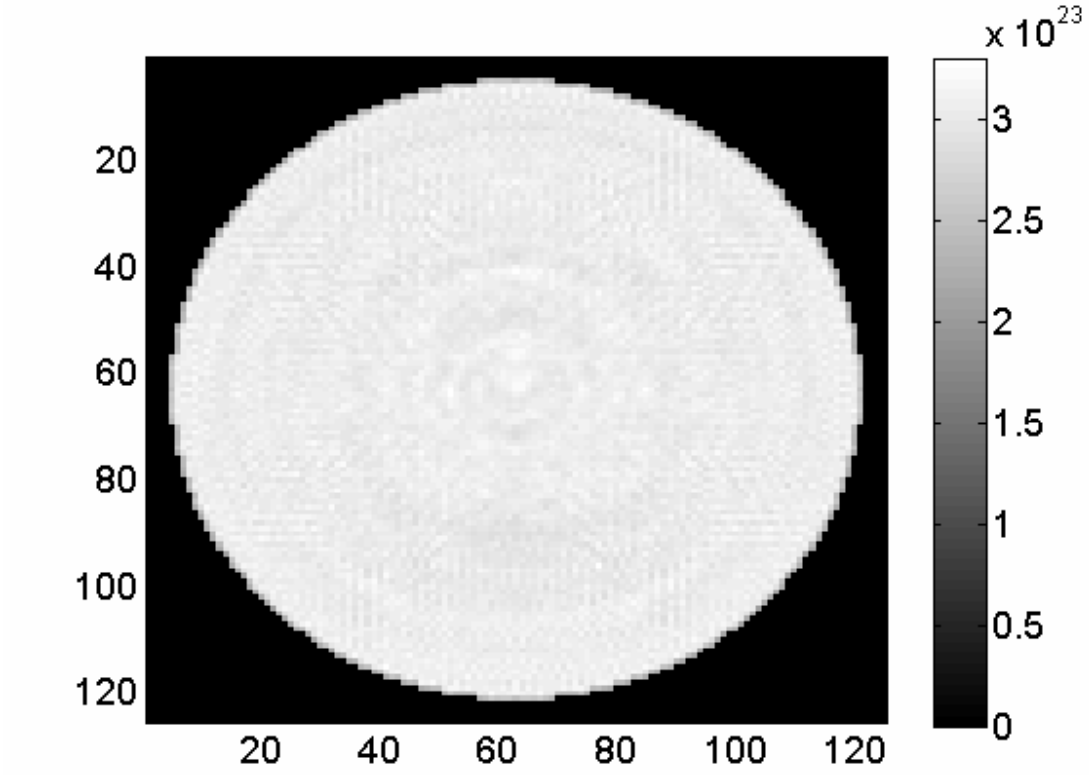

Figure 4.16. ρ_e reconstruction of phantom C without sufficient zero padding. The units of the image are (electrons/cm^3).

4.5. *Conclusions*

This chapter presents a technique capable of reconstructing electron densities from single KN scattered photons of large objects. The technique uses first generation CT, a ring of detectors and conventional FBP with appropriate attenuation corrections. The use of a ring of detectors

is an effective way of minimizing the problem of identifying changes in the scatter distribution due to the relative location of the scattering material with respect to the detector. This issue is evident by comparing figures 4.10(a) and 4.10(b). These images show that the number of scattered photons is dependent on the detector itself. Even without attenuation, reconstructions from each detector sinogram will yield different ρ_e as opposed to the ring integration. This results in quantification of changes in scatter that are due to electron density variations only. The factor that quantifies the fraction of scattered photons measured by the ring can be calculated as a function of the desired FOV by knowing the corresponding geometry and energy used. The $\overline{F}$ factor exhibits a radial dependency that results in only 2% changes for the FOVs of typical breasts (up to 20 cm).

A potential clinical benefit of the technique is illustrated in the reconstructions of the plastics phantom. The larger differences in ρ_e of plastics C-552 and B-100 provided better contrast than that of the primary image. Not only does the ρ_e allow for improved material identification but it can be seen that the contrast in the right ellipse is inverted with respect to that of the primary image. This additional information could result in better tissue characterization and consequently improved diagnosis.

The results from this chapter were obtained assuming a monoenergetic incident beam and focusing on single incoherent scatter. The purpose of this chapter was to show the basics of the algorithm and the next chapter will be devoted to correct for electron binding as well as both coherent and multiple scattering.

Table 4.2. Summary of electron density reconstructions results for the different phantoms. The table also indicates if the reconstruction is from an AN or MC sinogram. All reconstructions are from single scatter sinograms except where indicated. The last column indicates the ratio between the reconstructed ρ_e and correct ρ_e. The table also indicates if sufficient zero padding was used.

Reconstruction	ROIs errors	ROIs Standard deviations	Sufficient zero padding	Ratio
Phantom A (AN)	-1% to -2%	3% to 4%	√	N/A
Phantom B (AN)	-1%	2% to 3%	√	N/A
Phantom B (MC)	-6% to -8%	3% to 4%	X	N/A
Phantom C (MC)	-6%	2%	X	N/A
Phantom B (MC)	-2% to -3%	3% to 4%	√	N/A
Phantom B with multiple scatter (MC)	N/A	N/A	X	>2

5. A 1st generation scatter CT algorithm for electron density breast imaging which accounts for bound incoherent, coherent and multiple scatter: A Monte Carlo study

The material in this chapter has been reprinted and adapted from the *Journal of X-Ray Science & Technology*, In Press, Jorge E. Alpuche Aviles, Stephen Pistorius, Idris A. Elbakri, Richard Gordon and Bashir Ahmad, A 1st generation scatter CT algorithm for electron density breast imaging which accounts for bound incoherent, coherent and multiple scatter: A Monte Carlo study, Copyright (2011), with permission from IOS Press.

5.1. *Introduction*

The reconstruction of ρ_e images may be limited by nonlinearities introduced by attenuation, anisotropic probability of scatter, contaminating scatter [coherent scatter (CS) and multiple scatter (MS)] and noise. The reconstruction algorithm presented in Chapter 4 implemented corrections for attenuation and the anisotropic probability of single KN scattering. Under these conditions, it was able to reconstruct accurate images of ρ_e for breast sized objects.

Section 4.2.1 described the theory that relates ray integrals of ρ_e to the number of single incoherent scattered photons. In the context of this theory the presences of either CS or MS introduce inconsistencies and are therefore considered contaminating scatter. Since neither CS nor MS can be directly related to ray integrals of ρ_e, both CS and MS result in an excess of photons (with respect to the signal from single incoherent scatter). This is shown in the ρ_e overestimation of Figure 4.14(c) which includes MS. In the same way as MS, CS is expected to increase the number of photons measured by the ring. This will also lead to an increase in the number of photons which is not reflective of ρ_e. Electron binding on the other hand is expected to reduce the number of incoherent scatter events that is measured by the ring. The KN cross section assumes that incoherent scatter is the result of an interaction of a photon with a free and stationary electron. Orbital electrons do not meet these conditions and the probability of incoherent scatter is reduced. The purpose of this chapter is to reduce the limitations under which the reconstruction algorithm was previously derived and tested. This includes corrections for electron binding, coherent and multiple scatter. The algorithm was tested using full Monte Carlo (MC) simulations of the B-SECT system to provide a more realistic evaluation of its capabilities.

The EGSnrc MC code was used to simulate scans of the B-SECT system with a dose comparable to mammography. Breast CT dose studies that use diverging cone beams have been conducted [93, 142]. However, it was unclear if the same dose coefficients could be applied to a non-diverging pencil beam scan. MC simulations were used to quantify the *MGD* delivered to the breast as a result of the scan. All sources of scatter were simulated in

order to investigate their effect in ρ_e imaging. To address the issue of contaminating scatter, empirical scatter increase correction ratios (*SICR*) are introduced. The results of this chapter will show that the reconstruction of scatter images of inhomogeneous breast phantoms using a dose comparable to mammographic studies is not only feasible, but that with an appropriate correction for multiple scatter, the contrast may even be enhanced.

5.2. *Methods*

5.2.1. B-SECT system and reconstruction algorithm

This section summarizes the system and algorithm described in the previous chapter. Figure 5.1 shows the geometry of the B-SECT system that will be simulated. The system consists of a ring of discrete detectors designed to measure the scattered radiation. The scatter detectors are labeled by δ, where negative angles correspond to the right part of the ring and the 0º delta coincides with the incident beam (Figure 5.1). The system has a dedicated transmission detector located on the distal side of the object from the x-ray source. Unlike the scattered radiation detectors, the dedicated transmission detector could be pixilated in order to reconstruct a primary image of high spatial resolution. Following first generation CT practices, the breast phantom is translated across the pencil beam as shown by the dashed circle of Figure 5.1. This results in a complete projection. Once a projection is completed the breast phantom is rotated and the translation repeated, resulting in a transmission sinogram and one scatter sinogram per detector. Note that this acquisition can also be achieved by

moving the x-ray source and detectors while the breast remains stationary. While no measurements have been conducted, the system is being assembled with an x-ray tube consisting of a rotating tungsten anode with a 12º angle (model RAD-8, Rotating Anode X-ray Tube, Varian Medical Systems, Salt Lake City, UT). It is envisioned that readily available photomultiplier tubes can be used as scatter detectors.

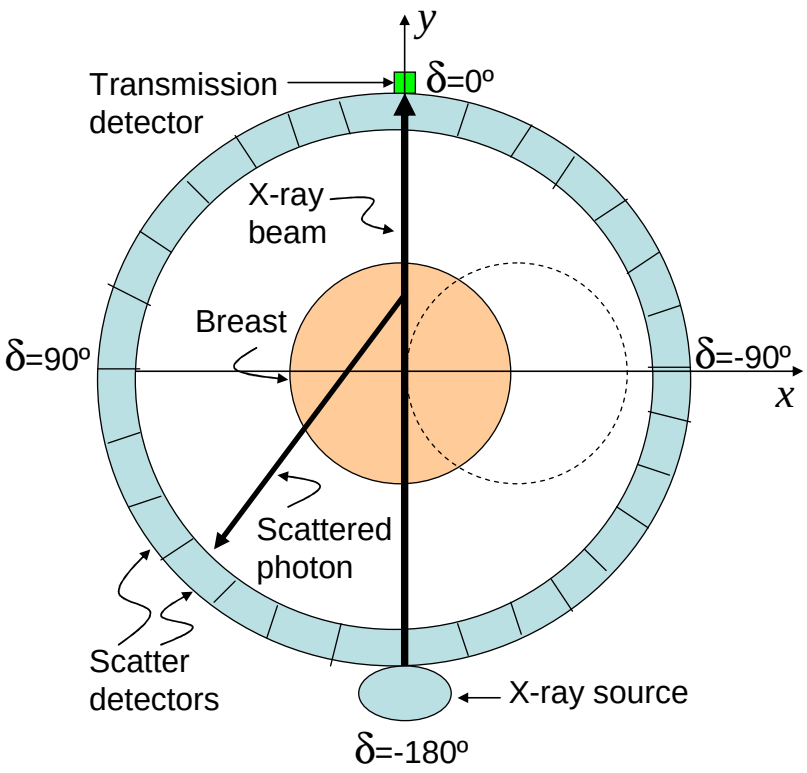

Figure 5.1. The geometry of the B-SECT system.

The B-SECT system is capable of reconstructing ρ_e images out of single KN scatter using the algorithm described in Chapter 4 and shown schematically in Figure 5.2 [37]. A μ image is reconstructed using the transmission sinogram and regular FBP. The μ image is used to calculate an estimate of ρ_e by multiplying it by the ρ_e/μ ratio for water at the mean energy of

the incident beam. Both μ and the ρ_e estimate are used to calculate ACF which are applied to the scatter sinograms. While the attenuation of the incident photons is known from the μ image, post-scatter attenuation is calculated using Equation (A.7) presented in Appendix A. The attenuation corrected scatter sinograms are summed to obtain the fraction $\overline{F}$ of the total incoherent scatter measured by the ring and correspond to scatter projections. Scatter projections that contain only single incoherent scatter photons are analogous to CT transmission measurements and are directly proportional to ray integrals of ρ_e. Images of ρ_e can then be reconstructed using any standard CT algorithm [148-150] and FBP was used. The reconstruction algorithm computes new sets of ACFs using the reconstructed ρ_e (Figure 5.2). However no iterations were required since these were found to only be necessary for extreme cases and the ρ_e of realistic phantoms did not improve with iterations (Chapter 4).

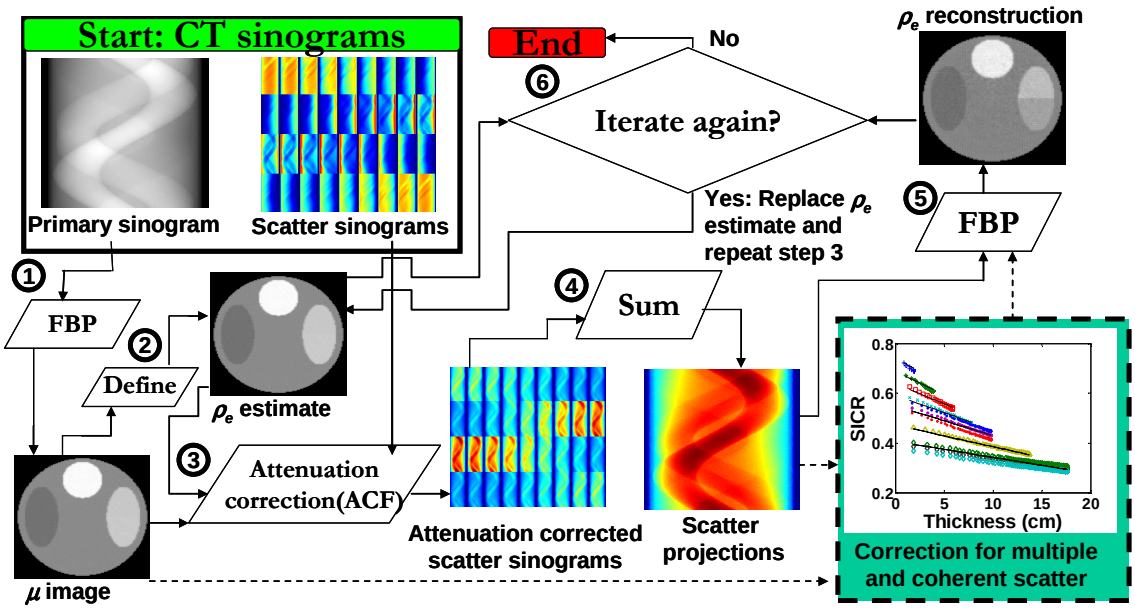

Figure 5.2. Flowchart of the ρ_e reconstruction algorithm. The dashed lines show the method to correct for multiple and coherent scatter which was not present in Chapter 4. The algorithm was implemented using the 'edrec.m' code found in Appendix B.

In this chapter all projections were zero padded to 1149 translations. The lack of proper zero padding lead to errors that ranged from -6% to -8% as showed in Chapter 4. In contrast, zero padding to 1149 translation results in ρ_e images with mean errors ranging from -1% to -2%.

5.2.1.1. $\overline{F}$ factor calculation

An essential part of the algorithm involves the calculation of the fraction of total incoherent scatter measured by the ring. This procedure was introduced in the previous chapter. For an infinitesimally small point, the fraction of photons measured by the ring is calculated using Equation (4.6) which can be rewritten as Equation (5.1)

$$F(y) = \frac{\sum_{\varphi} N_{SI}(\varphi)}{N_{Tot,Incoherent}}, \quad (5.1)$$

where y is the coordinate of the y axis (Figure 5.1). $N_{SI}(\varphi)$ denotes the number of photons that undergo single incoherent scatter by a scattering angle φ measured by the ring. The summation over φ is achieved by summing over all detectors. $N_{Tot,Incoherent}$ is the total number of photons undergoing single incoherent scatter (including those that are not detected). $F(y)$ is approximately constant across the object and can be approximated by taking the average value $\overline{F}$ over the FOV [37].

5.2.2. Monte Carlo simulations

The EGSnrc code was used to simulate the B-SECT system. The ability of MC simulations to model multiple scatter allows (i) accurate quantification of the total dose in the breast and (ii) investigation of the B-SECT performance in the presence of all types of scatter.

5.2.2.1. Dose quantification

The DOSRZnrc user code was used to quantify the dose in the breast [138]. DOSRZnrc is part of the EGSnrc MC package and allows fast and easy implementation of cylindrical geometries. Cylinders, made of homogeneous compositions of adipose and glandular tissue, are commonly used to quantify dose in BCT studies [93, 142]. The homogeneous breast phantom was simulated as a homogeneous mixture by weight of 50% adipose tissue and 50% glandular tissue [58] (which will be referred to as 50/50 breast). Figure 5.3 illustrates how a raster scan of the pencil beam is used to complete a 3D acquisition of the breast for one projection. This was simulated using an equivalent broad beam, incident on the side of a cylinder which models the breast with a cylinder of radius r, height of $1.5r$ and 50/50 breast composition as shown in Figure 3(b). A 4 mm layer of skin was added to the periphery of the cylinder and breasts with r = 5 cm, 7 cm and 9 cm were simulated. The incident number of photons was set to a million, resulting in MC uncertainties of less than 0.3% for the simulated cylinder.

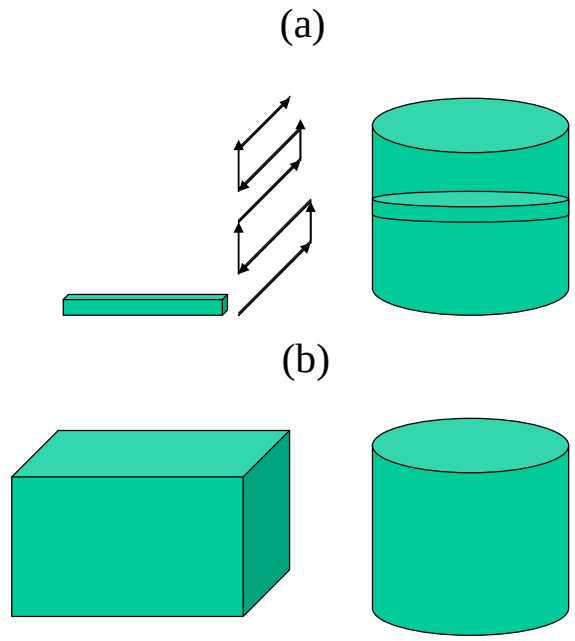

Figure 5.3. (a) Pencil beam raster scan needed to acquire a 3D image of the breast phantom used to quantify *MGD*. (b) Geometry of the equivalent broad beam incident on the side simulated by DOSRZnrc.

The *MGD* was calculated using Equation (5.2)

$$MGD = \frac{T\,\Phi_0\,S\,G}{f_g} 10^6, \qquad (5.2)$$

where T is the total dose deposited in the breast (in Gy per incident fluence) given by the DOSRZnrc simulation. Φ_0 is the beam incident fluence in photons/cm^2 and S is a factor that normalizes the dose delivered to the breast to the dose delivered by an incident fluence of 10^6 photons/mm^2. This incident fluence serves as a reference that allows direct comparison with

BCT results. f_g is the fraction by weight of glandular tissue and is equal to 0.5 for a 50/50 breast. The factor of 10^6 is used to obtain the *MGD* in units of μGy/(million photons/mm^2). *G* is a factor that accounts for the fraction of energy deposited in the glandular tissue and is given by

$$G = \frac{f_g \left(\frac{\mu_{en}}{\rho} \right)_g}{f_g \left(\frac{\mu_{en}}{\rho} \right)_g + (1 - f_g) \left(\frac{\mu_{en}}{\rho} \right)_a}, \qquad (5.3)$$

where (μ_{en}/ρ) is the mass energy absorption coefficient of either adipose or glandular tissue as indicated by the subscript. The (μ_{en}/ρ) of adipose and glandular tissue were calculated using the elemental composition given by Boone [58] and the (μ_{en}/ρ) of elements presented by Hubell and Seltzer [144].

The results of the DOSRZnrc simulation were compared with independent analytical calculations of the primary *MGD* (MGD_p). The primary *MGD* can be analytically calculated using Equation (5.4)

$$D_p(x, y) = \Phi_0 \, E_0 \, e^{-\int \mu \, dl} \left(\frac{\mu_{en}}{\rho} \right)_{50/50}, \qquad (5.4)$$

where $D_p(x,y)$ is the primary dose in a voxel with coordinates (x,y) and mass energy absorption coefficient $(\mu_{en}/\rho)_{50/50}$. E_0 is the energy of the incident beam and

$\Phi_0 e^{-\int \mu dl}$ denotes the attenuated fluence incident on the voxel. The dose deposited in each voxel can be used to calculate the total energy deposited in the glandular tissue and therefore MGD_p. Alternatively, DOSRZnrc calculates the total and scatter dose from which the dose from primary photons can be deduced.

5.2.2.2. MC simulation of the B-SECT system

DOSXYZnrc [137] is a MC user code useful for simulating rectilinear voxelized phantoms such as the ones described below. DOSXYZnrc was modified to simulate the scan of the B-SECT system and was tested, in the previous chapter, against an independent analytical simulator [37]. In the simulations of this chapter, the options to simulate coherent scatter as well as electron binding effects were turned on in EGSnrc. The simulation of coherent scatter did not include molecular interference effects. In this study the differential scatter signal is integrated along the ring to give a total cross-section. Taibi *et al*.[151] have shown that the total coherent scatter cross sections are similar both with and without molecular interference.

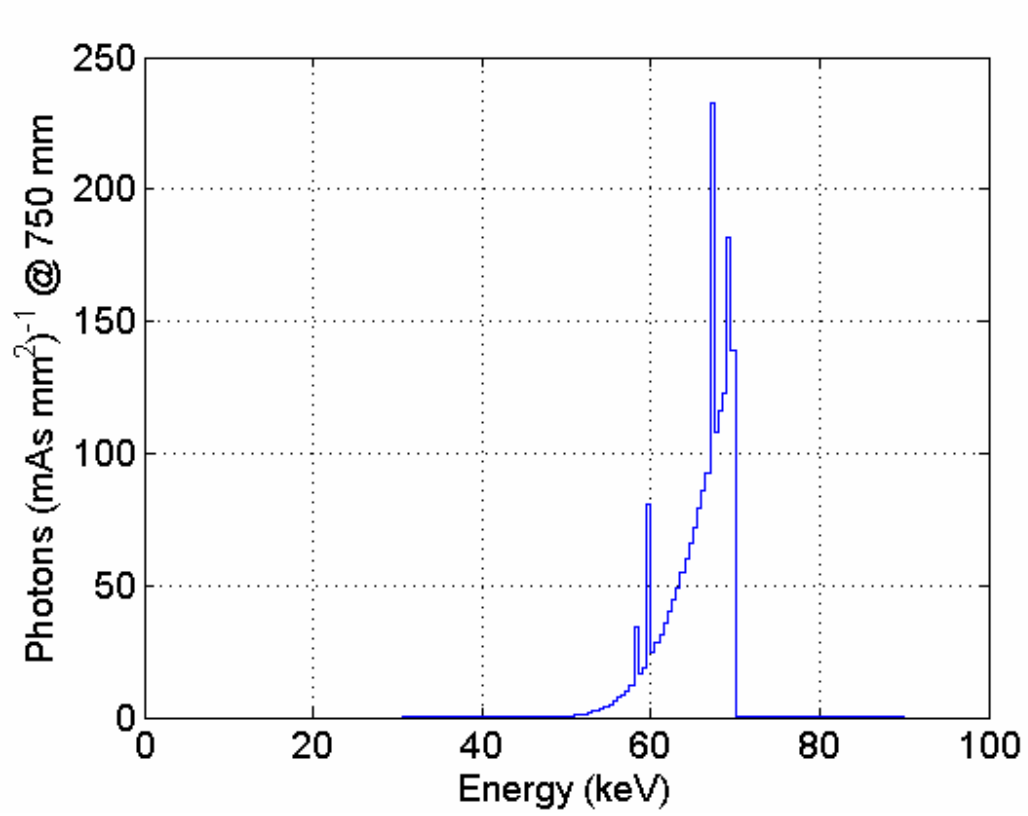

Figure 5.4. Spectrum of the simulated x-ray beam.

This stage of the project is based on simulated realistic quasi-monoenergetic beams [152]. Quasi-monoenergetic beams are currently being used in order to avoid beam hardening artifacts and to ensure accurate reconstructions of μ. Quantitative accuracy is needed for attenuation correction of scattered photons in ρ_e image reconstruction. The incident beam was simulated using a 90 kVp tungsten anode with an additional filtration of 1 mm Tungsten (Figure 5.4). This produces a beam with a mean energy of 65 keV and a full width at tenth maximum of 11 keV. This energy lies close to the energy at which the *MGD* per incident fluence is at its minimum (Section 5.3.1), allowing the use of more incident photons for a given dose. The simulated pencil beam has a square, 1 mm × 1 mm cross section. The ring of detectors was simulated as a spherical shell with 35 cm radius and equally divided into

segments that approximate square detectors of 5 cm × 5 cm. Each scattered photon was tracked until it reached the geometrical location where the detector would be located. The total number of transmitted (or primary) photons was also scored and was used as the measurement of the transmission detector. In contrast with the MC simulations described in section 5.2.2.1., the number of histories was set to deliver a *MGD* of 4 mGy for a 3D scan of the breast with 288 projections.

The scans of two different phantoms were simulated: a homogeneous breast with inserts which will be referred to as the Shikhaliev phantom [153] and an inhomogeneous breast phantom. Figure 5.5 shows the definition of the Shikhaliev phantom, modeled as a cylinder with 7 cm radius and height of 10.5 cm. The homogenous breast was simulated using voxels with dimensions of 1 mm × 1 mm × 10.5 cm and composition of 50/50 breast. The inserts consisted of cylinders of 1.4 cm diameter of blood, adipose tissue, MCC, glandular tissue, carcinoma and iodine content. The elemental composition of adipose tissue, 50/50 breast, glandular tissue, MCC and carcinoma were taken from Van Uytven *et al*.[15] whereas those of blood and iodine from Hubbell and Seltzer [144]. The MCC content region represents a volume composed of 90% glandular tissue and 10% calcium hydroxyapatite. The iodine content region is intended to represent the average tumor uptake of contrast agent [153]. The inhomogeneous breast phantom was used to test the overall reconstruction for a more realistic breast and was modeled from MRI breast images. These MRI images are segmented into three types of fibro-connective/glandular tissue, one transitional tissue and three types of fatty tissue [154]. Since the physical properties of these tissues were unknown, the three fibroconnective/glandular tissues were assigned to a single glandular tissue, transitional

tissue to 50/50 breast and the three fatty tissues to a single adipose tissue. The MRI phantom was further modified by binning the original 0.5 mm voxels into groups of 8. This process resulted in voxels of 1 mm size, matching the size of the beam that determines the sampling rate of the reconstructed image (voxel of the reconstructed image). This results in both simulated phantom and reconstructed image with the same voxel resolution, facilitating ρ_e comparison on a voxel-by-voxel basis. During the binning process voxels with adipose tissue, 50/50 breast and glandular tissues were combined to calculate the fractions by weight of adipose (f_a) tissue. In addition to adipose tissue, it has been suggested that three levels of glandular tissue provide a good tradeoff between breast model realism and practicality [155]. A fourth level of glandular composition was included to more equally subdivide the range of f_a into values of 0, 0.2, 0.5, 0.7 and 1. The final result is an asymmetric breast phantom made of 1 mm voxels and 5 different tissues defined by f_a. A 4 mm layer of skin was added to the periphery. Figure 5.6(a) shows a 3D surface rendering of the inhomoegensous breast.

The original MRI based 3D breast phantoms have, even after binning, 150 coronal slices. This large number of voxels increases the MC simulation time by a factor of 12 with respect to that of a geometry which extends the 2D cross section into the third dimension (also called 2.5D). In order to reduce the simulation time the central slice was extended in the chest-to-nipple direction by 15 cm [Figure 5.6 (b)]. This produces changes in scatter that are within MC uncertainties and the 2.5D model was used to simulate the complete scan.

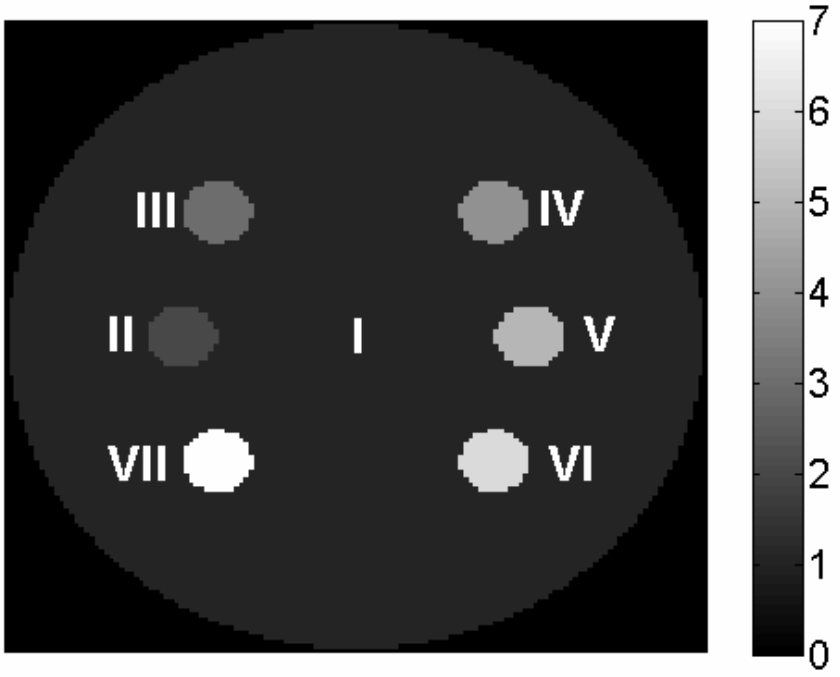

Figure 5.5. Definition of the Shikhaliev phantom with roman numbers corresponding to ROIs of 50/50 (I), blood (II), adipose tissue (III), MCC content (IV), glandular tissue (V), carcinoma (VI) and Iodine content (VII). The gray scale corresponds to the number associated with each ROI and has no physical meaning.

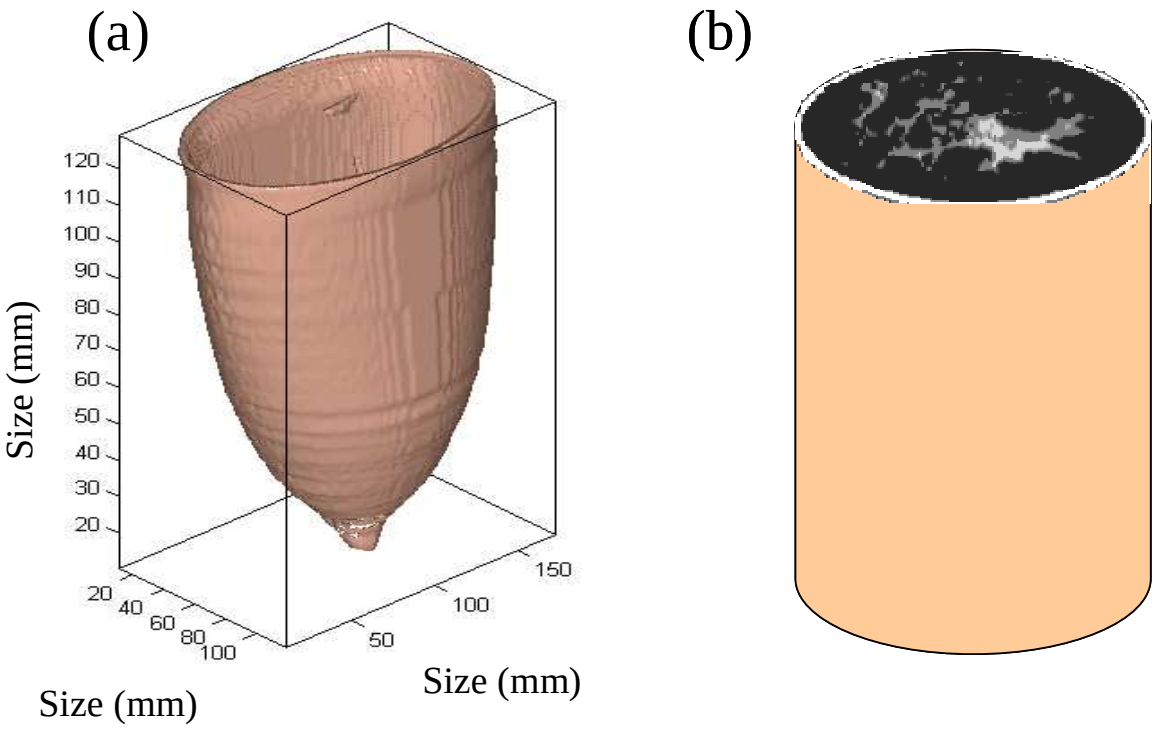

Figure 5.6. 3D surface rendering (a) of the inhomogeneous breast. The phantom was converted into a 2.5D breast (b) to reduce the MC simulation time.

5.2.3. Electron binding effects

The assumptions of the KN cross section break down for small values of momentum transfer. This is particularly important for the small scattering angles subtended by the ring. Since the ring measures a fraction of the total number of incoherently scattered photons, it is important to quantify this effect in the calculation of the corresponding fraction. For an infinitesimally small point, the fraction of photons measured by the ring is given by Equation (5.1).

The numerator of Equation (5.1) can be modified to include electron binding using Equation (3.21). The implementation of Equation (3.21) was validated by comparing the single incoherent scatter for a beam going through the centre of a 14 cm homogeneous breast phantom. The homogeneous breast phantom was simulated as a homogeneous mixture of 50/50 breast. The simulated beam had a 1 mm × 1 mm square cross-section (see section 5.2.2.2) with energy of 67 keV and 10^6 histories. This energy was used since it matches the mean energy of a beam previously used to reconstruct ρ_e images [16]. This beam is obtained with 2 mm Tungsten filtration which produces an impractically low output. This is the reason why filtration has been reduced to 1 mm for the scans described in section 5.2.2.2. Results for the beam with an energy of 67 keV show the ability to include electron binding at additional energies.

The denominator of Equation (5.1) can be calculated using Equation (5.5)

$$N_{Tot,Incoherent} = N_0 \rho N_A \left(\frac{{}_a\sigma}{A} \right) L \,, \qquad (5.5)$$

where ${}_a\sigma$ is the total incoherent scatter cross section per atom. The term in brackets can be calculated using Equation (5.6)

$$\frac{{}_a\sigma}{A} = \frac{1}{N_A} \left(\frac{\mu}{\rho} \right)_{incoherent} \,, \qquad (5.6)$$

where $(\mu/\rho)_{incoherent}$ is the incoherent scatter mass attenuation coefficient. The $(\mu/\rho)_{incoherent}$ of 50/50 breast was extracted from the PEGS (the EGSnrc data pre-processor) file and include electron binding effects.

Equations (3.21) and (5.5) through (5.6) can be used to calculate $F(y)$ and the corresponding $\overline{F}$. The elemental composition of 50/50 breast was used to calculate the fraction $\overline{F}_{E.B.}$ (where the subscript indicates that electron binding effects are being considered) of single incoherently scattered photons measured by the ring for different breast sizes.

5.2.4. Multiple and coherent scatter correction

The presence of MS and CS causes an increase in detected photons relative to the number of single incoherent photons which the algorithm uses to calculate the electron density. It is therefore necessary to quantify and correct for this relative increase in scatter for breasts of different sizes. The goal of this section is to construct an equation that predicts the scatter increase correction ratio before step 5 of Figure 5.2.

The MC code was used to simulate scans of homogeneous breasts for a single projection angle. The breasts were simulated as homogeneous cylinders with r = 1 cm, 2 cm, 3 cm, 4 cm, 5 cm, 7 cm and 9 cm, and corresponding heights of 1.5r. The geometry of the B-SECT system was the same as that described in section 5.2.2.2 as well as the incident beam. The scatter increase was sampled at the same size of the primary beam, i.e. every 1 mm. For comparison purposes, the scan of a breast with r = 7 cm was simulated assuming single KN

scatter, including all types of scatter and using the same number of photons as the simulations described in section 5.2.2. The number of histories was then increased to 10^8 to reduce the noise (MC uncertainty of less than 1%) in the quantification of scatter for all breast sizes. The scatter at each detector *d* was multiplied by its ACF_d generated with AN simulations since this correction is implicit in the calculation of scatter projections (step 4 of Figure 5.2). Scatter increase correction ratios were calculated using

$$SICR(L) = \frac{\sum_{d=1}^{D} N_{SI,d}(L) ACF_d(L)}{\sum_{d=1}^{D} N_{Tot,d}(L) ACF_d(L)}, \qquad (5.7)$$

where $N_{SI,d}$ represent the number of single incoherent scattered photons and $N_{Tot,d}$ the total scatter into detector *d*. The summation is over all *D* detectors. The independent variable *L* consists of the thickness traversed by the beam. Since the thickness approach ignores variations inside the breast and applies a correction which is a function of breast size only, the dependence on the radiological path was also investigated by replacing *L* by μL in Equation (5.7). Since transmission sinograms are sensitive to inhomogeneities it was hypothesized that the radiological path (μL) dependence would allow the impact of breast structure to be handled more accurately.

The *SICR* was approximately linearly dependant with *L* (and μL) for a given breast size (*BS*) but the parameters of the line (slope and y-intercept) were dependent on *BS*. This can be reflected in the following equation:

$$SICR(L, BS) = C_1^{'}(BS) + C_2^{'}(BS)L, \qquad (5.8)$$

where C'_1 and C'_2 are explicitly dependent on BS (with an equivalent equation when L is replaced by μL). The equations that matched the dependence of C'_1 and C'_2 with BS with the largest F-statistic are explicitly shown in Equation (5.9)

$$SICR(L, BS) = (C_1 + C_2 BS) + (C_3 + C_4\sqrt{BS})\,L \qquad (5.9)$$

with a similar equation as a function of μL instead of L. The values of parameters C_1, C_2, C_3, and C_4 were determined by fitting a 3D surface as a function of L (or μL) and BS using the Levenburg-Marquardt algorithm implemented in TableCurve3D (SYSTAT Software Inc., Richmond, CA). The empirical equation analytically calculates *SICR* using the transmission sinogram (or μ image to calculate L) and can be applied before the FBP step in the ρ_e reconstruction algorithm (Figure 5.2). The fitted equations [Equation (5.13) and Equation (5.14) below] were used to reconstruct the images of the Shikaliev and inhomogeneous phantoms. For the case of the inhomogeneous phantom a 14 cm breast size was used for the calculation of *SICR* since this corresponds to the FOV needed to cover its thickest part.

The accuracy of the reconstructed images were quantified in terms of the mean error for each ROI as defined by

$$Error(\%) = 100\left(\frac{\overline{\rho}_{e,ROI} - \rho_{e,true}}{\rho_{e,true}}\right), \qquad (5.10)$$

where $\overline{\rho}_{e,ROI}$ is the mean electron density of an ROI while $\rho_{e,true}$ is the true electron density of the same ROI as calculated from the elemental composition [Equation (3.13)]. The potential for lesion detection was quantified in terms of Rose's signal-to-noise ratio (*SNR*) as defined by the equation [9]

$$SNR = CNR\sqrt{N}, \qquad (5.11)$$

where *CNR* is the contrast-to-noise ratio and *N* is the number of pixels that make up the ROI. *N* can be approximated by $N = (\pi/4)*(d/\Delta)^2$, where *d* is the diameter of the ROI (1.4 cm) and Δ is the pixel size (1 mm) [9]. The *CNR* was calculated with respect to the 50/50 background according to [156]

$$CNR = \frac{\left|\overline{\rho}_{e,ROI} - \overline{\rho}_{e,50/50}\right|}{\sigma_{50/50}}, \qquad (5.12)$$

where $\overline{\rho}_{e,50/50}$ is the mean electron density of the 50/50 background and $\sigma_{50/50}$ is its corresponding standard deviation.

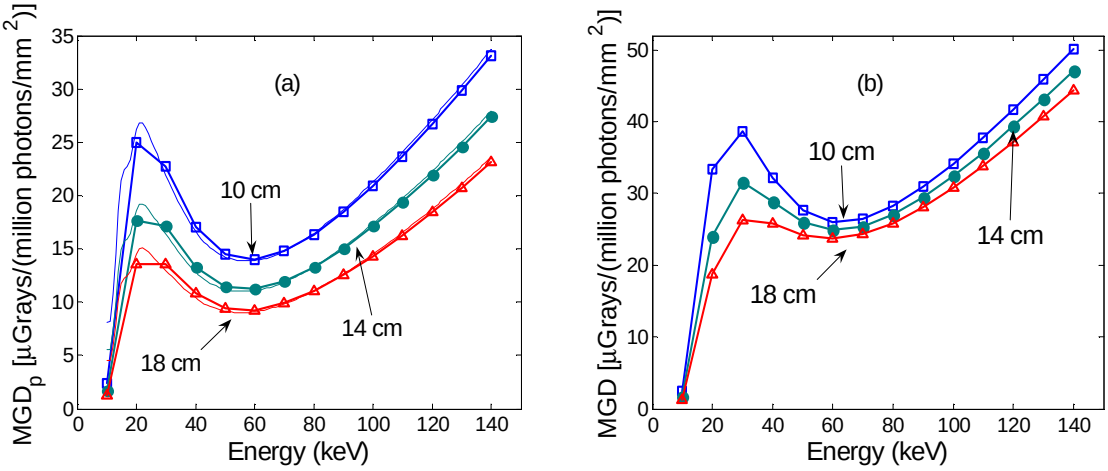

Figure 5.7. (a) Variation of mean glandular dose due to primary photons (MGD_p) for breast phantoms of different sizes and beams of different energy. The figure shows results from analytical (solid lines without markers) and MC (markers joined by dashed lines) simulations. (b) Total *MGD* per incident fluence as a function of beam energy and breast phantom size.

5.3. *Results*

5.3.1. Dose quantification

Figure 5.7(a) shows the variation of the primary *MGD* as a function of energy. The figure shows that MC and AN simulations are within 1% agreement for all breast sizes. Figure 5.7(b) shows the total (primary and scatter) *MGD* as a function of energy for different breast

sizes. Using this graph the number of incident photons needed to achieve a 4 mGy *MGD* for a given energy and breast size can be calculated.

5.3.2. MC simulation of the B-SECT system

Figure 5.8 shows the magnitude of scatter along the ring for the central and tangential beams (which correspond to the location of the solid and dashed circles of Figure 5.1). Scattered photons are classified as single incoherent, coherent only interactions, incoherent MS and Mix (which covers any combination of incoherent and coherent scattering). The total signal consists of the sum of all categories and this is what is measured in practice. The contribution of incoherent MS to the total scatter signal ranges from 4% to 77% with a mean value of 43% and standard deviation of 8%. This MS contribution is not constant across the detectors at 65 keV. For a beam going through the centre of the breast, the MS measured by the detector at δ = 0º is one half of that measured by the detector at δ = 180º. Coherent scatter makes up as much as 81% of the total signal for scattering angles less than 8º. This percentage drops quickly as a function of scattering angle reducing to 21% for angles between 8º and 16º and to less than 11% for larger scattering angles. The contribution of the mixture of incoherent and coherent multiple scatter to the total signal is 11% ± 5% and remains approximately constant across the detectors.

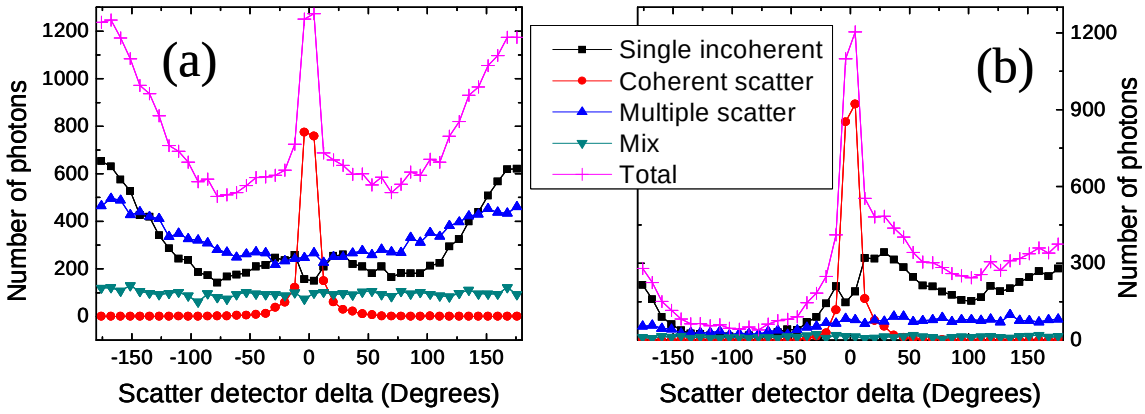

Figure 5.8. Variation in the number of scattered photons as a function of type and detector angle measured along the ring for beams passing through the centre (a) or tangentially (b) to the breast phantom.

5.3.3. Electron binding effects

Figure 5.9 shows the number of single incoherently scattered photons as a function of detector angle. The figure illustrates the magnitude of the scatter along the ring for a beam going through the centre of a 50/50 breast for a mono-energetic beam of 67 keV. The figure shows the variation in scatter when electron binding is taken into account with both MC and AN simulations. Figure 5.9 also shows the results of the AN simulation using the KN approximation for comparison. Figure 5.10 shows the variation in the fraction $\overline{F}$ for different breast size including ($\overline{F}_{E.B.}$) and excluding ($\overline{F}$) the effects of electron binding. Values of $\overline{F}_{E.B.}$ were used in the reconstruction of all ρ_e images in this chapter.

5.3.4. Multiple and coherent scatter correction

Figure 5.11 shows the total number of photons measured by the ring as a function of the thickness of the 14 cm breast (r = 7 cm) traversed by the beam. These measurements are obtained by summing over all detectors and are referred to as raw scatter projections to differentiate them from the scatter projections obtained after correcting for attenuation (Step 4 of Figure 5.2). The figure shows one half of the data points since the symmetry of the breast results in repeated measurements. The figure compares the raw scatter projections for single KN scatter with those including electron binding (labeled as single incoherent) and contaminating scatter.

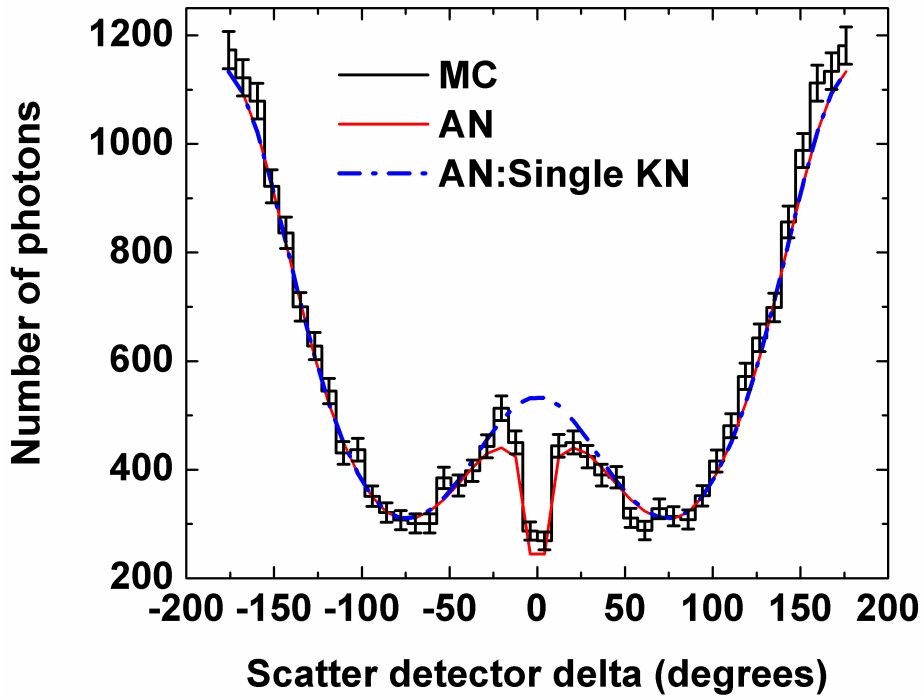

Figure 5.9. Number of single incoherently scattered photons along the ring of detectors. The graph shows the distributions of photons for MC (stairs with error bars) and AN (solid line) simulations of a beam with an energy of 67 keV going through the centre of the breast including electron binding effects. The graph also shows the hypothetical distribution under the KN approximation (dashed-dotted).

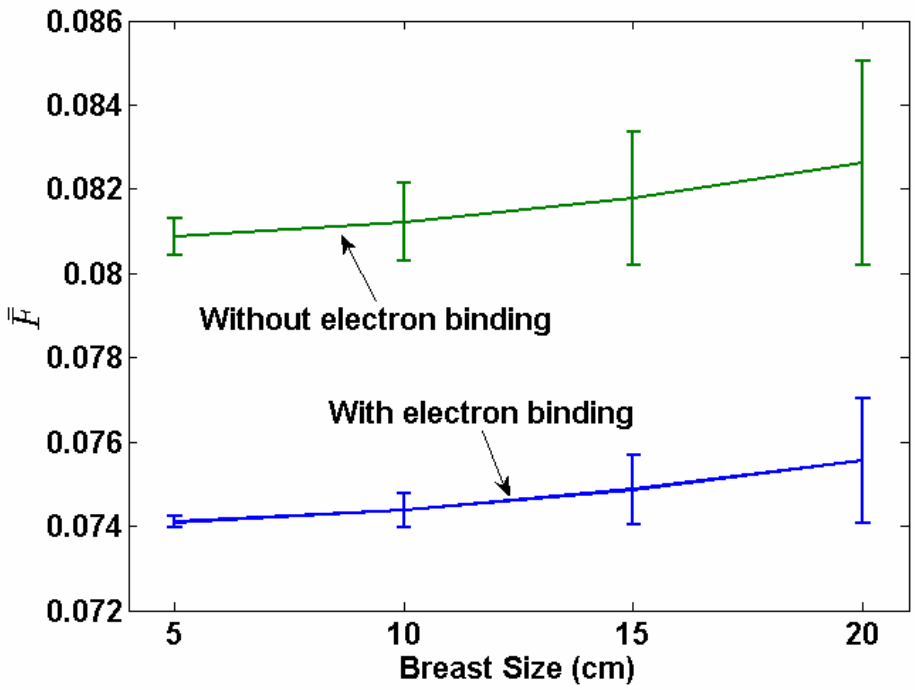

Figure 5.10. Variation in the fraction of photons detected by a ring of detectors relative to those that would be detected in a 4π geometry as function of breast size with ($\overline{F}_{E.B.}$) and without ($\overline{F}$) electron binding.

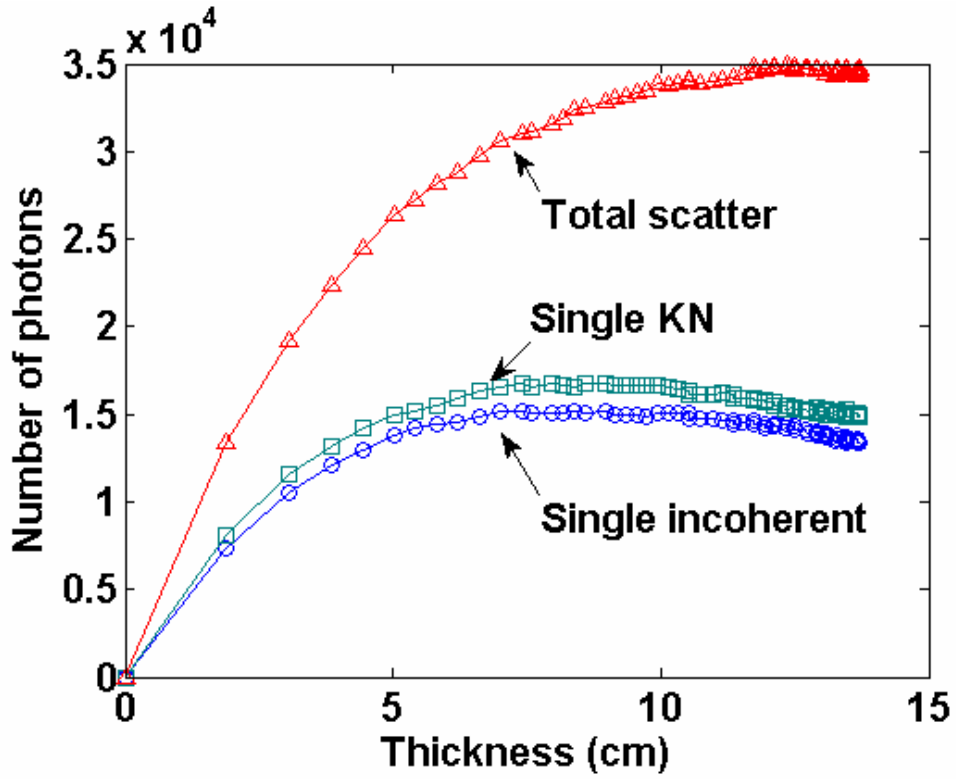

Figure 5.11. Number of scattered photons measured in the ring as a function of breast thickness traversed by the beam. This number of photons corresponds to the summation along each detector of the ring and represents raw scatter projections. The plot shows raw scatter projection of single incoherent and total scatter including electron binding. The raw scatter projection of single KN scatter is also shown for comparison.

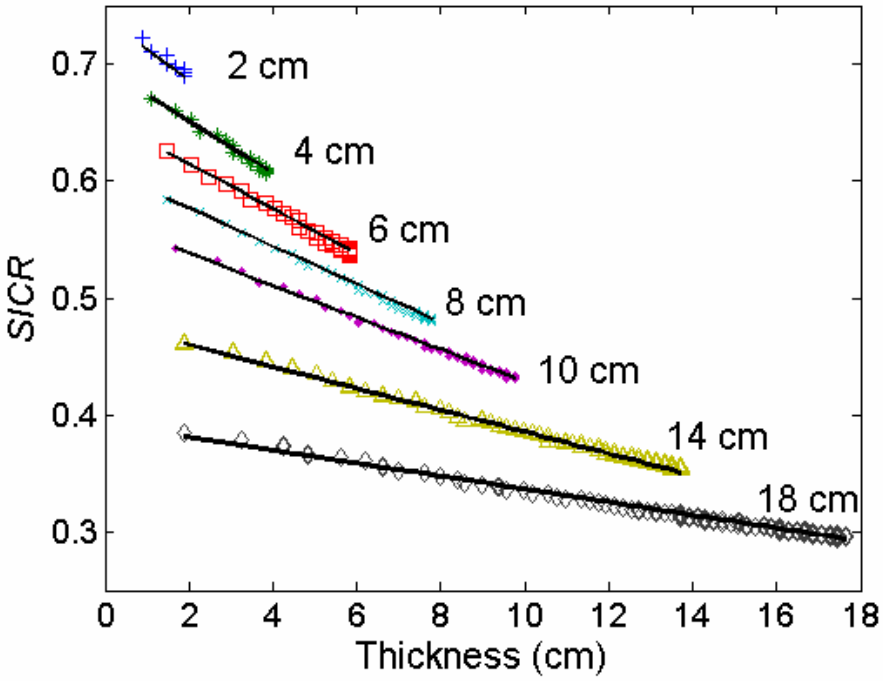

Figure 5.12. Symbols illustrate the scatter increase correction ratio's (*SICR*s) for different size breast phantoms as a function of thickness. The solid lines show the results of the linear fits of *SICR* vs thickness *L*.

Figure 5.12 shows the *SICR* as a function of thickness *L* for different breast sizes. A similar figure is obtained by plotting the *SICR* as a function of radiological path. This figure illustrates the effect of breast size on the variation of *SICR*. A correction scheme dependent on breast size and the physical or radiological path of the tissue being irradiated was implemented based on these observations. The fit of Equation (5.9) as a function of *L* and *BS* results in Equation (5.13)

$$SICR(L, BS) = (0.7827 - 0.02171BS) + \left(-0.0376 + 0.00756\sqrt{BS}\right)L, \qquad (5.13)$$

where the standard errors of all coefficients were within 1%. The same procedure was followed to fit Equation (5.9) as a function of radiological path μL and resulted in

$$SICR(\mu L, BS) = (0.7824 - 0.02171BS) + \left(-0.194 + 0.0391\sqrt{BS}\right)\mu L \qquad (5.14)$$

with coefficients whose standard errors were smaller than 1%. Figure 5.12 also shows the quasi-linear dependence of *SICR* as a function of *L* by setting *BS* to their corresponding size in Equation (5.13). Equations (5.13) and (5.14) correct the scatter projections of the Shikhaliev phantom with a mean error of -1% ± 1%.

5.3.5. Image reconstructions

Figure 5.13(a) shows the reconstructed image of the Shikhaliev phantom with no corrections for multiple scatter. A profile (Figure 5.14) through this image shows an overall increase in the reconstructed ρ_e along with a gradual increase towards the centre (called a capping artifact). Figures 5.13(c) and 5.13(e) show the ρ_e reconstructions with no iterations after using Equation (5.13) and Equation (5.14) for correction and with the same display window. Profiles through both reconstructions are shown in Figure 5.14. Figures 5.13(b), 5.13(d) and 5.13(f) are difference images obtained by subtracting images of figures 5.13(a), 5.13(c) and 5.13(e) from the true ρ_e image. Figure 5.15 shows the mean errors for each ROI for images reconstructed using *SICR* as a function of L and μL [Figure 5.13(c) and Figure 5.13(e)]. For comparison, Figure 5.15 includes the corresponding mean ρ_e errors from an estimate derived by linearly scaling the μ image by the $[\rho_e/\mu(E_0)]$ ratio for water. The error bars represent the standard deviations of each ROI. Figure 5.16 shows the reconstruction of the Shikhaliev phantom when the stopping criterion of Chapter 4 is used (6 iterations). The window level is set to display the minimum and maximum range of values as most of the images in this thesis. Figure 5.17 shows image reconstructions from sinograms generated using CS (circles of Figure 5.8) and MS (summation of ▲ and ▼ of Figure 5.8). These images show that both CS and MS can be used to produce images with inherent contrast.

Figure 5.18 shows the ρ_e reconstructions of the inhomogeneous breast phantom after applying the *SICR* correction as a function of both L and μL. The window display is the same

for both and has been adjusted in order to show regions of adipose tissue, 50/50 breast and glandular tissue as indicated by the arrows.

5.4. *Discussion*

5.4.1. Dose

The variation in the *MGD* (Figure 5.7) agrees with that observed in cone beam BCT studies conducted by Boone *et al.* [142] These results support the observation that the divergence of the beam has little impact on the *MGD* for their geometry. All breast sizes show an initial increase in dose associated with increased penetration and energy that peaks at about 30 keV. Beyond this energy the dose decreases from the combined effect of photon penetration and reduction in $(\mu_{en}/\rho)_{50/50}$. At about 60 keV the *MGD* reaches a minimum close to the energy that minimizes $(\mu_{en}/\rho)_{50/50}$. Higher energies show a continuous increase for both primary and total *MGD*. The increase in the primary *MGD* can be explained by the increase in $D_p(x,y)$[Equation (5.4)] for large E and $(\mu_{en}/\rho)_{50/50}$. The total *MGD* follows this behavior with the additional contribution from scatter dose that also increases with energy.

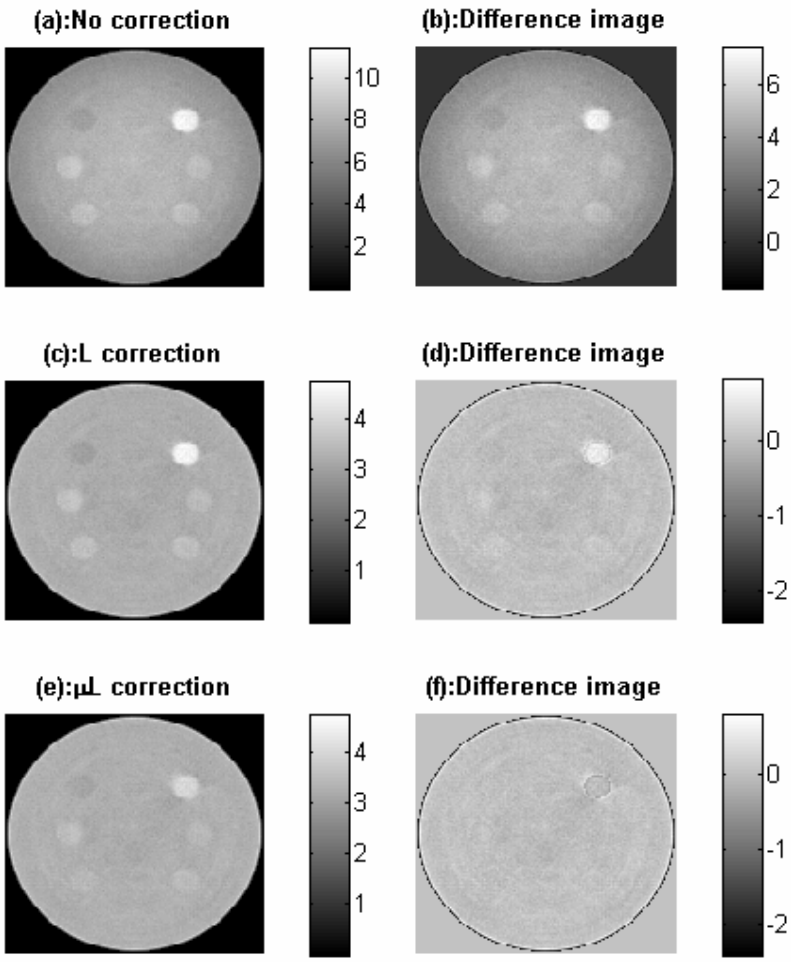

Figure 5.13. Electron density reconstructions with no correction (a), correction using L (c) and correction using μL (e). The images of the second column are difference images obtained by subtracting the reconstruction from the true ρ_e image. (a) and (b) have their own window display which cover their corresponding minimum and maximum values. The window display of (c) and (e) are the same and cover the minimum and maximum of both images. The window display of (d) and (f) are the same and cover the minimum and maximum of both images. All images in units of 10^{23} electrons/cm^3.

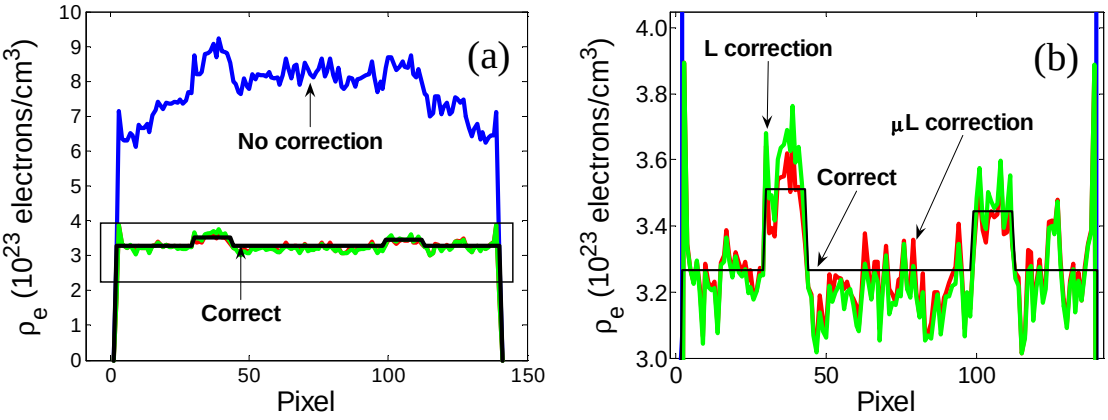

Figure 5.14. Profiles through figures 5.13(a), 5.13(c), 5.13(e) as well as the correct profile.

Figure 5.14(b) is a zoomed version of the rectangular area shown in Figure 5.14(a).

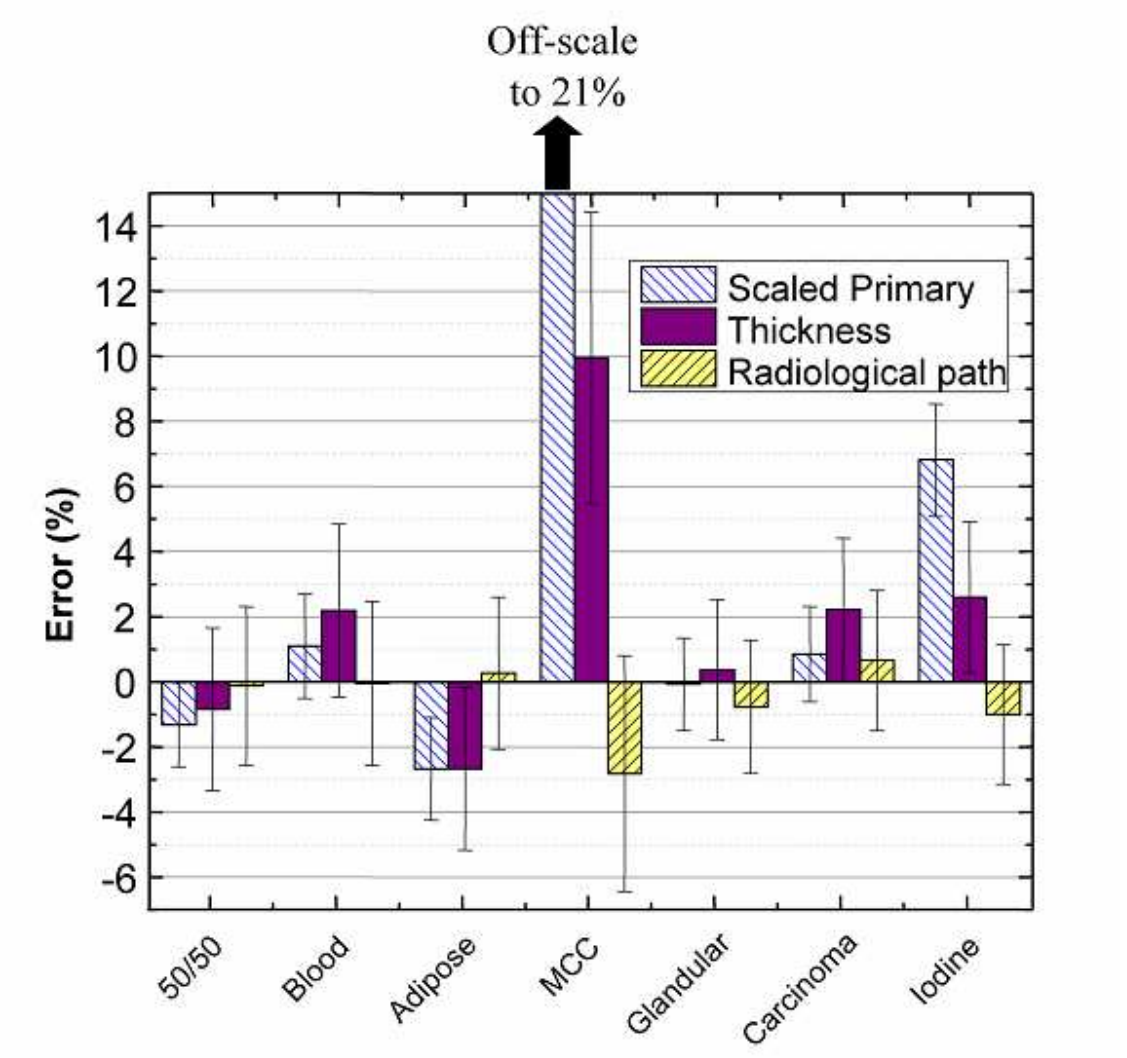

Figure 5.15. Mean errors for each ROI of figures 5.13(c) and 5.13(e). The results of the ρ_e estimate, derived from μ, are also shown as a comparison. The error of the MCC region for the scaled primary extends to 21%.

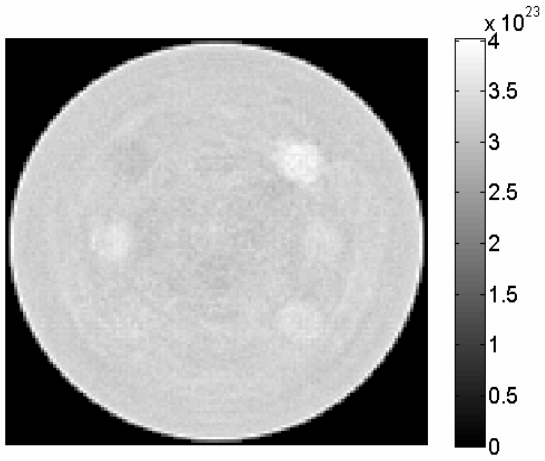

Figure 5.16. Reconstruction of the Shikhaliev phantom when the stopping criterion of Chapter 4 is used (6 iterations).

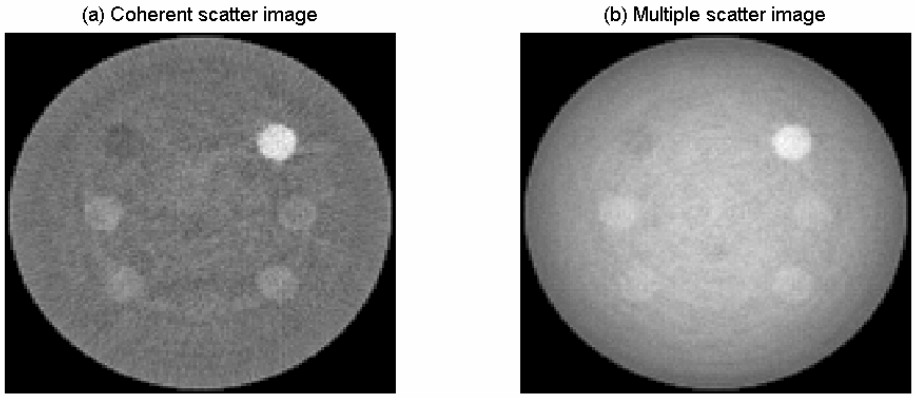

Figure 5.17. Images reconstructed from coherent (a) and multiple scatter (b).

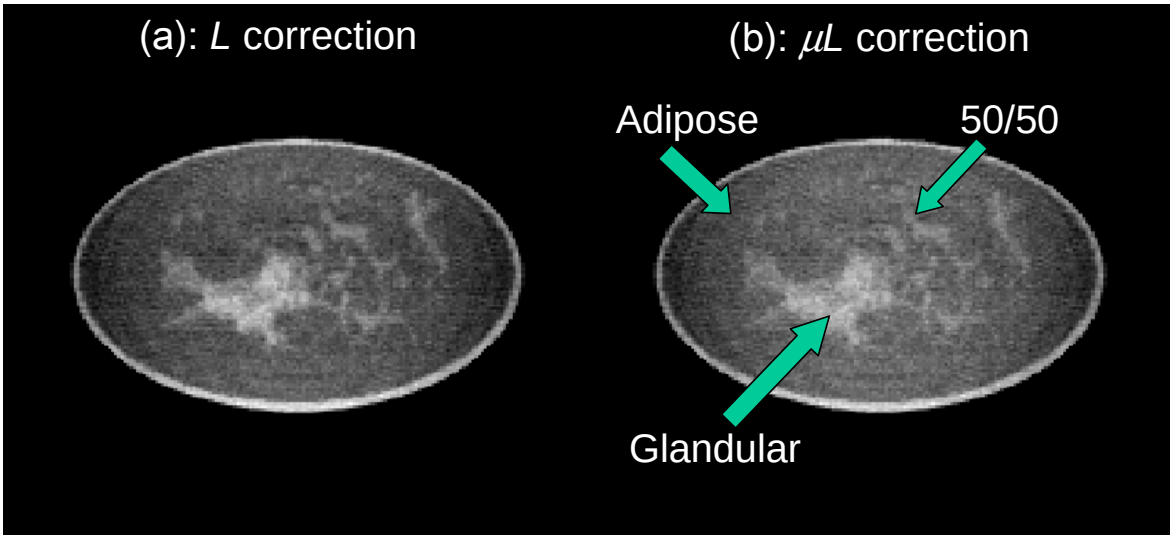

Figure 5.18. Electron density (ρ_e) reconstruction of the inhomogeneous breast phantom. The window display has been enhanced to show different types of breast tissue as indicated by the arrows.

The *MGD* results provide a reference to analytically calculate the dose of a BCT scan. $D_p(x,y)$ can be calculated using Equation (5.4) and compared with the results of Figure 5.7(a). The results of Figure 5.7(b) can then be used to calculate the total *MGD* of the breast. Alternatively, as done in this study, these results can be used to calculate the incident number of photons that result in a particular dose. For example, Figure 5.7(b) shows that for an energy of 60 keV, there is a *MGD* of 24.93 [μGy/(million photons/mm^2)]. The required dose per projection is (4 mGy/288 projections) 13.89 μGy, which means that ~5.6 x 10^5 photons per mm^2 would result in the desired dose. This number of histories was used to simulate the scan of the B-SECT system (Section 5.2.2.2). Note that although the mean energy of the beam was of 65 keV, the change in the *MGD* from 60 keV to 70 keV is only 2%. The same

procedure was used to calculate the number of histories for the 4 mGy scan of Chapter 4. Figure 5.7(b) shows that the MGD for a 14 cm breast at 80 keV is 27.11 μGy/(million photons/mm^2). Therefore the incident fluence needed in order to deliver the desired *MGD* per projection is of (13.89 / 27.11) ~512,316 photons/mm^2. For an incident beam with dimensions of 1.2 mm x 1.2 mm, the number of incident histories is of 737,735.

5.4.2. Electron binding effects

Figure 5.9 validates the implementation of the model that accounts for electron binding. The average difference between the MC and AN simulations is -2%. A reduction in the probability of incoherent scatter for small scattering angles as a result of electron binding is also observed. For example, the average difference between the KN simulation and that including electron binding is 1% for $|\delta|>16^o$, -14% for detectors with $|\delta|<16^o$ and $|\delta|>8^o$, and -49% for $|\delta|=8^o$ and smaller. Figure 5.10 shows that electron binding reduces the fraction of photons measured by the ring by 8% for breasts smaller than 10 cm and by 9% for larger breasts. This effect is also observed in Figure 5.11 if the raw scatter projections of single incoherent and single KN scatter are compared.

5.4.3. SICR empirical correction

The *SICR* dependence on breast size is a function of the production and attenuation of single incoherent and multiple scatter with respect to the breast size and the asymmetric location of

the beam. This is shown in Figure 5.19 where the angular distribution of single incoherent and MS for beams traversing the same thickness of different breast sizes are compared. The dependence of single incoherent scatter on breast size is due to the post-scatter attenuation and the net result is that the detected single incoherent scatter reduces with breast size. For MS, the breast size dependence can be observed by comparing the scatter from a 2 cm path (L) through a small (2 cm) and large (18 cm) breast. This L corresponds to the central beam through the 2 cm breast (the small circle at the centre of Figure 5.19) while being approximately tangential to the 18 cm one (the large circle at the centre of Figure 5.19). The greater volume of the 18 cm breast produces more MS than the 2 cm breast. The asymmetry around the primary beam of the 18 cm breast results in an increase in attenuation on the side with the greater volume. However, the net effect for a 2 cm thickness is an increase in MS for the large breast with respect to that of the 2 cm one. An additional dependence on breast size is introduced by the ACF. However, a correction for attenuation is essential for accurate ρ_e reconstructions and needs to be applied to each detector, i.e. prior to ring integration. These factors result in *SICR* which are dependent on both L and breast size. The *SICR* empirical correction accounts for the breast size dependence by varying the slope and intercept of an equation which is linear with thickness.

The dependence of *SICR* on breast size introduces a practical challenge to the correction. While the selection of breast size is trivial for cylindrical phantoms, this can be ambiguous for real breasts. In this study, the breast size selected was based on the FOV needed to image the breast and resulted in an approximate mean error of -1%[†]. More studies are needed to

[†]This number was obtained by calculating the error over all image pixels and their corresponding mean. This was done due to the lack of well defined ROI in the inhomogeneous breast phantom.

investigate the calculation of an equivalent breast size for clinical anatomies or to develop a more general equation using segment integration.

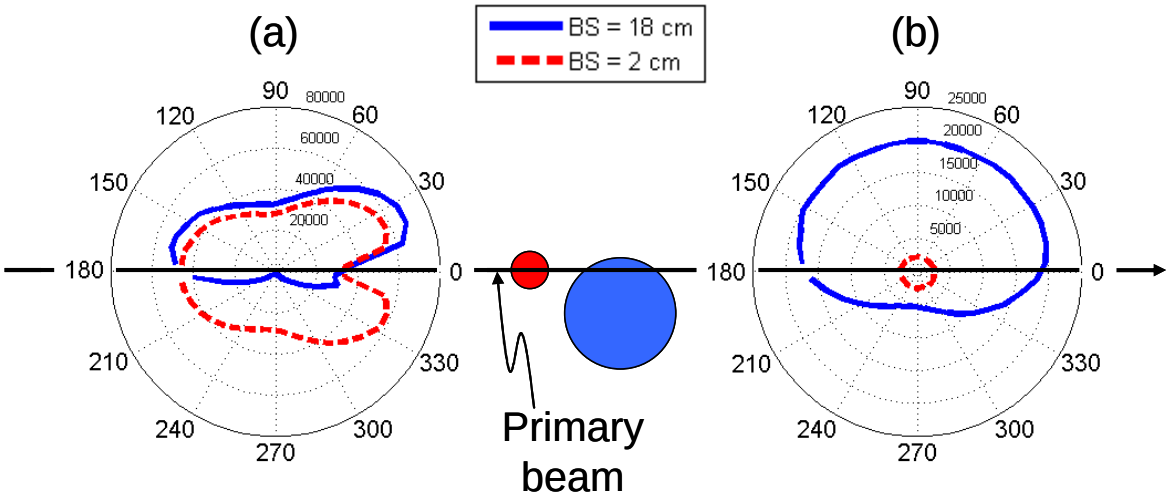

Figure 5.19. Angular distribution of single incoherent (a) and multiple scatter (b) for beams going through the same thickness of breast with sizes of 2 cm and 18 cm. The figure shows the primary beam going through the centre of the small (2 cm) breast while been tangential to the large one (18 cm). The units of the polar angles are in degrees and correspond to the δ definitions of Figure 5.1.The units of polar axis are in number of photons and correspond to the results from the simulation described in section 5.2.4.

The difference between using L and μL is their sensitivity to breast structure. Both approaches work in the case of homogeneous breasts but neither is able to completely correct for all inserts (Figure 5.15). Using the thickness to calculate the *SICR* is equivalent to

applying a post-reconstruction method to correct for the overestimation and capping. The μL approach is more accurate than using L since it attempts to correct for inhomogeneities.

5.4.4. Image reconstructions

The MC simulations show that coherent scatter contributes ~9% to the total signal for a typical size breast, demonstrating that multiple scatter is the major source of image artifacts. The artifacts in Figure 5.13(a) are in line with the observations at the end of Chapter 4 where CS was not present. The capping artifact of Figure 5.14(a) is due to the overall increase in the scatter projections with respect to those expected from single incoherent scatter. This can be explained by noting that the increase (Figure 5.11) is larger when the beam goes through thicker parts of the breast. Electron density reconstructions without any correction are overestimated by more than a factor of 2 in both the Shikhaliev and inhomogeneous phantoms.

Figure (5.15) shows contrast reduction of the Iodine ROI whose original ρ_e is 5% larger than that of the background. The ROI error (of -3%) and the SD of the background (3%) combine to make this ROI nearly unnoticeable. Table 5.1 shows the ROIs errors for reconstructions with and without iterations for phantoms B (of Chapter 4) and Shikhaliev. The results show that the errors for some ROIs increase with iterations in both cases. Reconstructions from AN generated sinograms of the same phantoms and using a-priori knowledge of attenuation result, with the exception of the MCC ROI, in ρ_e errors of -1% with and without iterations. This suggests that the algorithm is able to converge to the correct solution under ideal

conditions. The reconstruction of the Shikhaliev phantom using the stopping criteria of section 4.2.5, a-priori knowledge of attenuation and MC generated sinograms results in similar results than those of Table 5.1. This suggests that noise, the main difference between the AN and MC sinograms, can lead to inaccuracies with iterations while Equation (A.7) had little effect. With regards to the results of Phantom B, Section 4.4.2 indicated that the range of errors (within -3%) did not change with iterations. Table 5.1 shows that this is true but the ρ_e error of ROI V increases with iteration. The same behavior is observed by replacing the sinogram by its AN counterpart. This suggests that the inaccuracy of the post-scatter attenuation is responsible for the increase in error while noise had little effect. These results indicate that the iterative option of the algorithm may need to be modified to handle photon noise (the main difference between AN and MC sinograms), inaccuracies in ACF calculations (specifically in the post-scatter attenuation) and inaccuracies in the correction for contaminating scatter. Phantom A (Chapter 4) is the only reconstruction whose ρ_e improved with iterations. It is unlikely that breasts will exhibit the extreme case of virtual Phantom A, therefore reconstructions with no iterations are discussed from now on. The ρ_e image after a single iteration is close to the correct solution but the inaccuracies mentioned above can lead to inconsistencies which in turn result in inaccurate electron densities.

Table 5.1. Electron density errors for each ROI of Phantoms B and Shikhaliev. The reconstructions correspond to results of the initial estimate, reconstruction without and with iterations.

Phantom B				Shikhaliev phantom			
ROI	Initial estimate	No iterations	With iterations	ROI	Initial estimate	No iterations	With iterations
I	-3	-3	-3	50/50	-1	<-1	<-1
II	-5	-2	-2	Blood	1	<-1	-1
III	-1	-2	-2	Adipose	-3	<1	1
IV	-2	-3	-3	MCC	21	-3	-8
V	14	-1	-3	Glandular	<-1	-1	-1
				Carcinoma	1	1	1
				Iodine content	7	-1	-3

Figure 5.15 shows that electron densities reconstructed using L have mean errors ranging from -3% to +3% with the exception of the MCC region where the error is +10%. Using μL results in ρ_e errors that range from -1% to +1% for all regions with the exception of the MCC region where the error is -3%. In comparison, the ρ_e estimate derived from the μ image has errors that range from -3% to +7% with a MCC region error of 21%. This shows that this approach can reconstruct ρ_e images with a reduced range of error (13% and 4%) when compared to the use of μ to predict ρ_e (24%). This is also true if the MCC region is excluded in the computation of the range of errors (6% and 2% vs 10%). A common way of measuring relative ρ_e consists of applying a bilinear model, i.e. two linear fits of Hounsfield unit (HU) vs relative ρ_e [32]. In this bilinear model, two different lines are used to calculate the relative ρ_e below and above a HU threshold value (typically 100). Since the HU of the MCC is 479 at this energy, it is possible that the line used for HU>100 will result in smaller ρ_e error for the MCC region. However the HUs of all other ROIs are less than 100 and it is unlikely that the errors in ρ_e can be reduced by using the μ image alone.

Comparing Figure 5.13(c) and Figure 5.13(e) shows that the reconstruction using L has improved contrast while μL results in electron densities with smaller errors (Figure 5.15). Table 5.2 lists the CNR for each ROI with respect to the 50/50 background for different images. The corresponding SNR (for lesions of 1.4 cm as defined in the original Shikhaliev phantom) is obtained by multiplying the CNR by a factor of ~12 ($\sqrt{N}$) and all ROIs exceed Rose's criterion for lesion detection (SNR>5) [157]. Equation (5.11) can be used to calculate the number (N) of pixels needed for the detection of carcinoma by setting SNR=5. N is

related to the diameter of the circular ROI according to $N=(\pi/4)*(d/\Delta)^2$ as indicated in section 5.2.4 [where Δ is the size of the pixel (1 mm)]. This suggests that a carcinoma with a diameter of 2 mm could be detected with the current algorithm. It should be noted that this size is applicable to the detection of carcinoma with respect to a 50/50 homogeneous background. The CNR of carcinoma is similar to those obtained by Van Uytven *et al.* [15] Van Utven *et al.* found CNRs of 2.63 and 3.04 for abnormal lesions simulated as glandular tissue and calcification content by weight of 0.16% and 0.55% respectively. In terms of accuracy, both approaches are able to reconstruct the ρ_e within 1%. The precision of both approaches, as measured by the standard deviations, ranges from 2% to 3% with the exception of this study's MCC region that can be as large as 5%. Overall, the technique presented in this thesis is equally accurate and slightly less precise but doesn't require the use of costly and complex detector technology with good energy resolution (200 eV was used by Van Uytven *et al.*). The CNR for the primary image is larger due to the combined effect of both a larger contrast in μ and a smaller standard deviation of the background (1% for the μ image vs 2% and 3% in the ρ_e images). Note that these images convey different information. The CNR of the L approach improves by a factor that ranges from 1.4 to 1.9 with respect to the μL approach. This is because the thickness approach makes no attempt to correct for the additional contrast due to CS and MS (Figure 5.17). That CS has inherent contrast is well known and has been studied for many years [120, 121, 158]. The MS contrast is somewhat surprising and is due to the use of first generation CT approach. In first generation scatter CT, any region with large ρ_e is likely to produce more single scatter that can undergo MS. The size of the region will also affect the number of photons undergoing MS. Large regions with large ρ_e will result in more MS than small regions. On the other hand, large regions with

small ρ_e will produce less MS than small ones since MS could have been produced by the other regions with larger ρ_e. Therefore both magnitude and size of the region are likely to change MS and consequently disturb the scatter projections. This will manifest as contrast resulting in an image that is no longer representative of ρ_e exclusively, but rather of the objects "scatter properties". These three images may form a valuable set of tools to provide tissue information. While the μ image has the largest contrast, it is not directly related to the electron density of the object. The ρ_e is better quantified by the scatter image reconstructed using the μL approach but at the expense of lower CNR. The L approach can be used to enhance the scatter contrast at the expense of reduced ρ_e accuracy. This multiple information is not available in either image alone.

The reconstruction of the inhomogeneous breast phantom shows that it is feasible to reconstruct ρ_e images of large inhomogeneous objects. The inhomogeneous breast modeled in this study was intended to provide a test of the reconstruction technique for more realistic conditions. More specifically, it was used to evaluate the ability of the algorithm to distinguish breast internal structure and reconstruct asymmetric objects. The simulated scan is representative of the scan corresponding to a central slice and, for slices closer to the nipple; additional breast-like material may be required to compensate for the lack of tissue underneath which would not generate MS. This support material could be added by using a breast holder previously suggested to form the breast into a cylindrical shape [93].

Table 5.2. CNR for each ROI of the Shikhaliev phantom with respect to the 50/50 background for different images.

ROI	μ image	ρ_e with thickness correction	ρ_e with radiological path correction
Blood	7.7	4.3	3.1
Adipose	4.8	2.7	1.8
MCC	39.5	14.8	8.2
Glandular	5.1	2.7	2.0
Carcinoma	6.1	3.6	2.7
Iodine content	11.0	3.7	1.9

5.5. *Conclusions*

This chapter presented the results of the MC simulation of a first generation B-SECT system. The results from the simulation show that using the B-SECT system, useful scatter images could be obtained from a 3D scan with the doses comparable to those used in cone beam BCT. Electron binding reduces the probability of incoherent scatter for detector angles of <16º. For the 65 keV energy used in this study, this results in a net reduction of 8% to 9% in the single incoherent scatter measured by the ring. This reduction can be taken into account when calculating the fraction of incoherent scatter measured by the ring, accurately relating scatter projections with ρ_e ray integrals. CS dominates the scatter signal for scattering angle less than 8º but it rapidly decreases to less than 11% for scattering angles larger than 16º.

MS is of the same magnitude as single incoherent, does not remain constant across the detectors and is the major source of image artifacts. The contributions from both CS and MS cause an increase in the reconstructed values of ρ_e and a gradual increase towards the centre of the breast (capping artifact). The overall contribution from all sources of scatter increase the value of the reconstructed ρ_e by a factor greater than 2 if not corrected for. Using a MC simulation of the system it is possible to develop an empirical correction that is dependent on breast size and either thickness or radiological path of the incident beam. Both correction approaches predict the scatter projections of a cylindrical phantom with a mean error of 1%. Although these approaches have their limitations, it is possible to reconstruct ρ_e images that are more accurate than the estimate derived from the primary by using a correction based on radiological path-lengths. This could potentially improve and complement BCT, especially for materials whose μ is not driven exclusively by ρ_e.

This study shows that using first generation incoherent scatter CT it is possible to reconstruct ρ_e images of inhomogeneous breasts with errors of -1%. Beam polychromacity and low fluxes pose challenges that must be overcome in order to make the technique clinically relevant. Although practical challenges remain, future efforts will be directed towards the practical implementation of the B-SECT system. Experimental measurements will establish the ultimate benefit of reconstructing *in vivo* scatter images of the breast.

6. Summary and future work

6.1. *Summary*

X-ray mammography has undergone many improvements over the years and is currently the gold standard for breast imaging. These improvements have made it a practical technique with good spatial resolution and large sensitivities, capable of detecting thousands of cancers per year. However the current sensitivity and specificity of mammography still results in missed cancers and unnecessary false positives. This has lead many investigators to search for new and innovating modalities that can aid in breast cancer detection. Volumetric techniques, including BCT, have risen among these modalities and have shown potential to replace mammography. Its tomographic nature reduces the overlap of structures and could lead to detection of lesions with sizes smaller than those detected with current mammography. This could in turn result in improvements in breast cancer survival [70].

Current BCT systems use an x-ray cone beam with a 2D flat panel detector, both of which rotate around the breast. Using a cone beam has the disadvantage of incurring large levels of scatter contamination. Studies show that the scatter to primary ratio can be as large as 0.5 for the typical breast and, if not corrected for, can lead to image artifacts, noise, contrast reduction and inaccuracy in the reconstructed μ [44, 100, 113, 114]. This can limit the ability to quantify tissue using the μ. In addition, the μ itself may not be sufficient to characterize

tissue and the inclusion of ρ_e imaging holds promise as an aid for tissue characterization. Electron density images can be reconstructed using incoherently scattered photons, making them a latent source of valuable information. An ρ_e image could be particularly useful for MCC, which remains as one of the main challenges in BCT, and materials whose μ contrast is small.

The ultimate benefit of simultaneous ρ_e and μ imaging of the intact breast remains unknown. This can be investigated conducting laboratory studies and the B-SECT system has been designed for this purpose. The B-SECT system is based on first generation CT, providing a cost-effective and simple approach to reconstruct images of breast samples, mastectomies and, depending on their results, potential volunteers. Electron density imaging is limited by the anisotropic probability of scatter emission and detection, attenuation, noise and contaminating scatter. These issues were previously addressed using optimization approaches that required long computation times and whose convergence can be affected by reconstruction parameters. Analytical algorithms were also attempted but had limited accuracy due to incomplete attenuation correction and fail to address the anisotropic probability of scatter and detection.

The objective of this thesis was to develop a reconstruction algorithm for first generation ISCT suitable for the laboratory B-SECT system. This thesis started by addressing the fundamental limitation of anisotropic probability of scatter and detection. This is an essential problem that can limit the accurate reconstruction of ρ_e images out of incoherently scattered

photons. The algorithm was built from the simplistic scenario of Chater 4 and was generalized to include more realistic issues in Chapter 5.

Chapter 4 introduced a first generation ISCT algorithm that addressed the fundamental problem of reconstructing ρ_e images out of single KN scattered photons. Single KN is the simplest scatter model that depends on the ρ_e of the object. Chapter 4 was published in the *Journal of X-Ray Science and Technology* [37] and is a hybrid (analytic-iterative) first generation ISCT algorithm that reconstructs ρ_e images of objects with breast sizes. A ring of detectors is introduced and measures a fraction of the total number of scatter using a factor $\overline{F}$ that is approximately constant. This enables the number of scattered photons to be directly related to ray integrals of ρ_e independent of the location of the scattering centre with respect to the detector. ACFs were introduced and calculated using transmission measurements and an estimate of ρ_e. The ACFs were applied iteratively and converge to the correct solution within a few iterations. The algorithm avoids the need to formulate an objective function and the selection of parameters that can affect its solution. The robustness of the algorithm to the initial estimate was shown by using a virtual phantom in the absence of noise. The algorithm was tested against MC simulations to provide an independent set of data with noise. MC simulations on a phantom made of realistic plastics demonstrate its usefulness in practical cases without iterations. The algorithm could be used confidently for scenarios when incoherent scatter is the dominant type of scatter and the KN approximation holds, e.g. high energy photon beams. Even without multiple scatter correction, the qualitative features of the object are still preserved. The algorithm was tested in the absence and presence of noise

corresponding to a clinically feasible dose. The ρ_e images had accuracy as good as -1%, no worse than -3% and standard deviations that ranged from 3% to 4%.

The practicality of the algorithm presented in Chapter 4 may be limited by the assumption of single KN scatter. The KN cross section is an approximation that breaks down for small scattering angles and energy, while ignoring coherent and multiple scatter is unrealistic. Corrections for these issues were built into the reconstruction algorithm in Chapter 5 and were submitted to the *Journal of X-Ray Science and Technology* [159]. This is the next step in the development of the algorithm to handle more realistic conditions. The options that control electron binding and coherent scatter were enabled in the MC simulations of the B-SECT system. The limiting assumption of a mono-energetic beam was removed by simulating a quasi-monoenergetic beam with a mean energy of 65 keV that can be generated in the laboratory. The MC simulations were also used to conduct an extensive study to quantify the *MGD* as a result of first generation CT scan and, accordingly, calculate the number of histories that results in a dose of 4 mGy. The results show good agreement with dose calculations of BCT systems based on cone beams. Electron binding reduced the number of single incoherently scattered photons measured by the ring by up to 9% but was explicitly included in the calculation of the $\overline{F}$ factor. The presence of both CS and MS resulted in an increase in scatter that can not be directly related to ρ_e and, if not corrected for, overestimate the ρ_e and result in a capping artifact. Empirical scatter increase correction ratios were derived from MC simulations and used as corrections with the aid of the primary image even in the case of inhomogeneous and asymmetric breasts. Two empirical equations were derived as a function of radiological path and thickness and effectively reduced image

artifacts. This method is similar to corrections for beam hardening applied in commercial CT scanners (also based on empirical corrections in projection space [160]). Scatter bone densitometry has also applied MC simulated correction factors [161, 162]. A limitation of the empirical correction is that it would have to be re-simulated if the tube potential is changed. Although it would be preferred to avoid this tedious process, the difficulty of developing an analytical model for MS poses a major challenge. The correction based on the radiological path gave the most accurate ρ_e image but has less CNR than the image reconstructed using the thickness. The thickness correction, insensitive to inhomogeneities, can potentially improve the contrast in scatter images based on the inherent contrast of CS and MS. The results suggest that the algorithm can detect 2 mm lesions embedded in homogenous breast tissue and improve quantification of ρ_e with respect to the estimate derived from the primary image.

This dissertation presents the results of a first generation incoherent scatter CT algorithm for breast imaging. The algorithm is able to reconstruct the ρ_e of breast soft tissues with an accuracy of 1%, precision (as quantified by the standard deviations) ranging from 2% to 3% and a mean glandular dose of 4 mGy. The algorithm has achieved the targeted accuracy but it may lack the precision needed to differentiate glandular tissue from carcinoma. However, the reconstructed images showed improved quantification of ρ_e which could aid in tissue characterization. The results of this thesis are based on computer simulations and the major challenges are related to the practical implementation of the system. Future efforts should be directed to overcome these issues and further experimental evaluation of the technique is warranted.

6.2. *Future work*

This thesis showed the ability of the algorithm to reconstruct ρ_e images using computer simulations. The next logical step consists of testing the algorithm with real measurements from the B-SECT system. However, there are a number of practical issues that must be addressed before the system can be tested. Integrating the area under the spectrum of Figure 5.4 indicates that ~300 mAs (at a distance of 75 cm from the source) are needed to achieve the number of photons simulated in Chapter 5. This combination of tube potential (90 kVp) and mAs (300) can potentially be achieved in 1 s using the x-ray tube in the lab. This would result in scanning times in the order of hours which makes it suitable for non-moving objects but not for volunteers. This combination may also result in tube heating and consequently long cooling times. To reduce the tube heating one can explore reducing the amount of filtration. For example, reducing the thickness of Tungsten to 0.9 mm increases the total output by a factor of 1.8 while the mean energy and the full width at tenth maximum of the beam remains approximately the same. Studies will have to be conducted to investigate the tube load capabilities and the thickness of filter material that can be used to scan larger objects in less time without substantially degrading the accuracy of the reconstructions. The model of Equation (4.5) can be generalized to account for polyenergetic beams but the μ image will lose quantitative meaning and will be subject to the cupping artifact. This will in turn complicate the computation of the correct ACFs which requires μ for any energy of the incoming beam. Alternative approaches consist of exploring other quasi-mononergetic beams published in the literature. Saito has showed that it is possible to perform quasi-monochromatic (59 keV ± 1.9 keV) CT using a Tungsten target and the balance filter method

[163]. This same approach has been used by Beath *et al*. in first generation CSCT [164] but the disadvantage of this method is its high dose. Jost *et al*. used a Tungsten CT tube to obtain beams with mean energy of 57.5 keV, full width at half maximum of 5 keV and fluxes as high as 10^7 photons/(mm^2 s) [165]. This flux corresponds to 10^9 photons/(cm^2 s) which for the fluence employed in Chapter 5 (5.6 x 10^7 photons/cm^2) will require about 0.05 s per pencil beam location. This results in ~7 seconds per projection for a 14 cm slice. This means that, in principle, one can acquire 288 projections in ~34 minutes which is comparable to an MRI scan. Another possible solution would be to correct the μ image for beam hardening [166] and investigate mean corrections for polyenergetic attenuation. This approach would enable conventional x-ray tubes with clinical spectrums to be used. Conventional tubes can generate outputs of up to10^7 photons/(mm^2 s) [167] which can result in practical imaging time. Ultimately, fan beam algorithms may be imperative for patient studies and would have to be carefully selected based on their current limitations (Chapter 2).

The energy used in this study was based on the desire to use more incident photons per mean glandular dose. This energy also favours the production of scatter but compromises the contrast of the μ image. Establishing the optimal energy for simultaneous ρ_e and μ imaging of the breast is beyond the scope of this thesis but a brief summary of the factors that will be affected is now given. Figure 5.7 shows that setting the MGD to a given value (e.g. 4 mGy) will change the number of incident photons. This will in turn change the noise in both ρ_e and μ images. Changing the energy of the beam will also change the probability of photon scatter, affecting noise in the ρ_e image as well as potential scatter artifacts in the primary one. Another parameter that is affected by energy is the μ of the breast itself. Changing μ will lead

to changes in the primary image contrast along with noise in both images. The contrast of the ρ_e image on the other hand will be unaffected by changes in energy. The difference between ρ_e and μ images will also change with energy and, consequently, the benefit of simultaneous imaging. For energies where incoherent scatter dominates the μ, little benefit can be expected since the μ image will reflect change of ρ_e. On the other hand, the photoelectic effect will dominate the μ for low energies and the μ image will be weighted to the contribution from the atomic number as opposed to the ρ_e. In summary, changing the energy of the beam will produce changes in the CNR of the μ image while affecting the noise in the ρ_e image.

The incident beam was simulated using the parallel source option available in DOSXYZnrc. In practice all x-ray sources are divergent and lead to (1) an increased beam size and (2) reduced fluence with distance. However the number of photons remains constant over the size of the beam and will create the same number of scattered photons as long as there is a homogeneous amount of material over the beam. The presence of inhomogeneities will contribute to scatter from a beam that should have not have contributed in the case of a parallel beam. This means that the divergence of the beam will result in image blur whose magnitude depends on both object inhomogeneity and amount of divergence. The divergence can potentially be reduced by increasing the distance from the source to the object but at the expense of reduce flux. It is recommended that this issue is investigated further.

The results of this thesis show that there are potential benefits of using the current algorithm but its precision may not be sufficient to differentiate glandular tissue from carcinoma. The current standard deviations, even for noise free reconstructions, can be as large as 4%. This

implies that the algorithm is not quantum limited and increasing the number of beam translations and projections can potentially improve the reconstruction. For example two major artifacts are observed in the reconstruction of Figure 5.13 (e): rings and a circle close to the centre of the phantom. These artifacts are also present in primary images of a homogeneous breast reconstructed with the same beam size and number of projections as shown in Figure 6.1. The window display of the image has been enhanced to emphasize the artifacts and shows that are not exclusive to the ρ_e reconstruction. However increasing the number of projections or translations while keeping the same dose, would result in reduced incident fluence. This reduction in incident fluence will hence result in less number of scattered photons and noise could become the limiting factor. The time needed per scan will also be increased consequently. Further investigation on the trade-offs between noise and the quality of the CT image reconstruction is recommended.

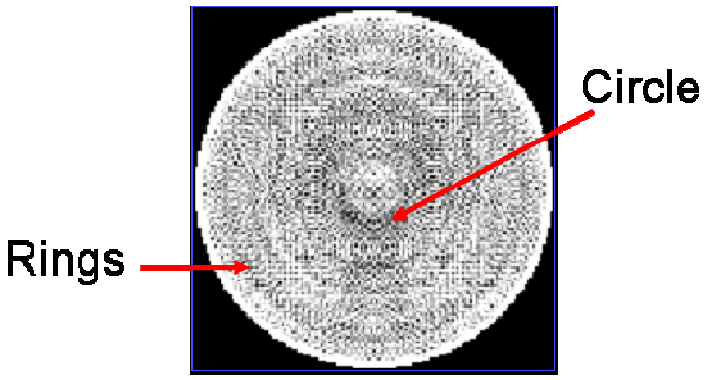

Figure 6.1. Primary image of a homogeneous breast phantom simulated in the same way as the Shikhaliev phantom. The image has been windowed to enhance the display of reconstruction artifacts.

The iterative potential of the algorithm has yet to be optimized. The iterative function reconstructs accurate images out of sinograms from AN simulations and accurate attenuation correction. The results from Chapter 5 show that the variations with iterations may not be suitable for breast imaging where the ρ_e differences can be as small as 2% [39]. This was not an issue in Chapter 4 since the smallest ρ_e difference was of 14%, the ρ_e error increased by 2% with iterations and the SD of the background was 4%. It is hypothesized that noise, which is the main difference between AN and MC sinograms, and inaccuracies in the attenuation correction lead to variations in the reconstructed ρ_e with iterations. Studies show that scatter imaging is an ill-posed problem and that the selection of regularization can affect the convergence of the solution [24, 27]. Regularization was not investigated in this thesis but may be necessary to perform iterations. In addition, the current stopping criterion is based on the difference between images but alternative criteria can be investigated. The results of Chapter 5 indicate that when no iterations are used the reconstructed images are more accurate but more research could allow the iterative function to be used if desired.

The above mentioned issues must be addressed before the system can be translated into the clinic. Given that these issues can be overcome, it is possible to envision further applications where the technique can be useful. For example, there is great interest in quantifying breast density since this property has been linked with high risk of developing cancer [168]. The technique presented in this thesis could be used to quantify breast density on a voxel by voxel basis. Electron density imaging can also be used provide tissue information to make better diagnosis [169]. Efficient tissue characterization can eventually result in on-site diagnosis,

eliminating the time between test and diagnosis and, hence, minimizing patient concern. Biopsy procedures could be reduced and its resources re-allocated to other strategies. The ultimate goal is to have an efficient, cost-effective, comfortable procedure of low dose that improves patient care.

Appendix A.

Chapter 4 pointed out that knowledge of μ at E_0 and E_s is necessary in order to compute attenuation correction factors (ACFs). While μ at E_0 is known from the primary image, μ at the energy of the scattered photons (E_s) is not directly available and a technique capable of predicting it was developed. The problem was approached by expanding μ for a particular material around the primary energy E_0 using Taylor series

$$\mu(E) = \mu(E_0) + \left.\frac{d\mu}{dE}\right|_{E_0} (E - E_0) + \frac{1}{2!}\left.\frac{d^2\mu}{dE^2}\right|_{E_0} (E - E_0)^2 + \ldots, \quad \text{(A.1)}$$

where E is an energy which, in this case, corresponds to E_s. It can be seen that truncation to the zero order term corresponds to estimating $\mu(E)$ using the primary, i.e. $\mu(E)=\mu(E_0)$. Since the energy of scattered photons is always smaller than that of the incident photons, the use of primary values of μ would always result in an underestimation of the attenuation suffered by scattered photons. For this reason it was decided to incorporate the first order term of Equation A.1. This term linearly scales the value of $\mu(E_0)$ to any E using the first order derivative of μ evaluated at E_0. The challenge with this approach is that it requires the unknown first order derivative $d\mu/dE$. Nevertheless, it can be shown that $d\mu/dE$ at 80 keV (energy initially used in the simulations) can be estimated from the value of the primary μ using a power expansion around $\mu(E_0)$. This is reflected in Figure A.1 which was calculated assuming that μ is described by Equation (A.2)

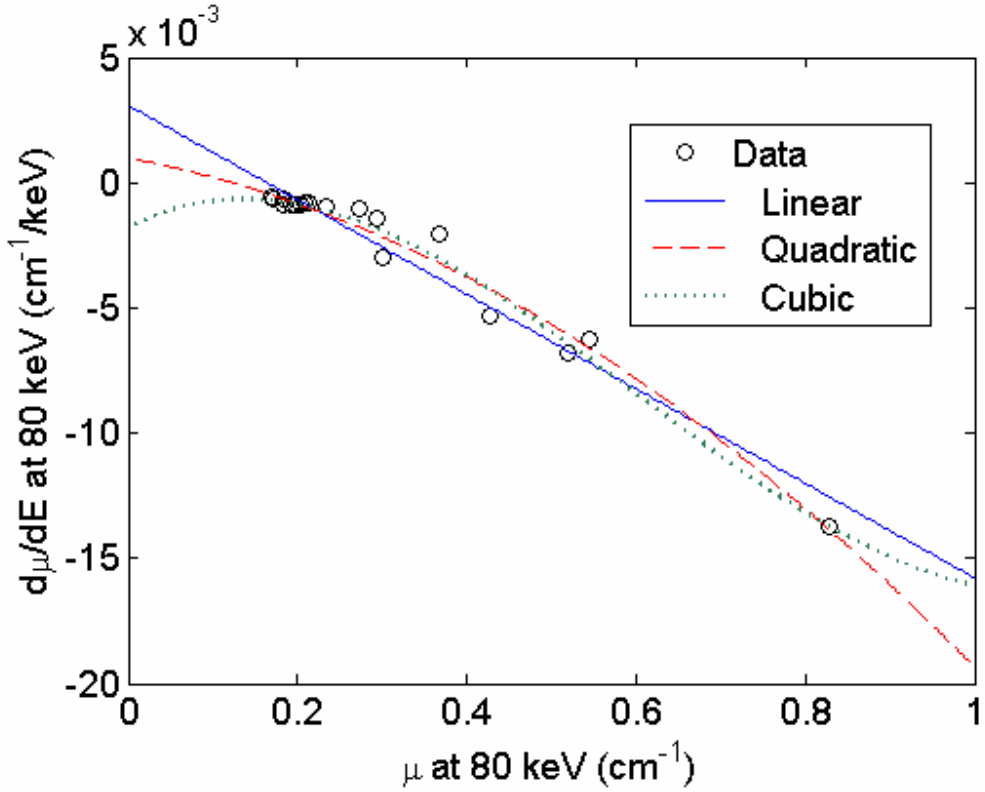

Figure A.1. Approximation of $d\mu/dE$ at E_0 by a power series of μ at E_0.

$$\mu(E) = a\left(\frac{Z}{E}\right)^3 + \rho_e\,{}_e\sigma(E), \quad \text{(A.2)}$$

which is obtained by setting n = 3 in Equation (3.3). This exponent is generally agreed to describe the photo-electric effect at diagnostic energies [123]. Note that the parameter a differs from that of Equation (3.3) by the density ρ. The incoherent scatter cross section ${}_e\sigma$ can be calculated using Equation (4.4) under the KN approximation. The first order derivative of Equation (A.2) was derived using software for symbolic computation [Maple

(Waterloo Maple Inc., Waterloo, ON)] and including Equation (4.4) explcitly. The values of *a*, which are material dependent, were obtained by solving for *a* in Equation (A.2). The equation was solved for each material given $\mu(E_0)$. Table A.1. lists the set of radiologically important materials that was used and plotted in Figure A.1 as "Data". These materials are either present in the body or have been used in x-ray studies.

Figure A.1. can be mathematically stated as

$$\left.\frac{d\mu}{dE}\right|_{E_0} \cong \sum_{p=0}^{P} c_p \left[\mu(E_0)\right]^p \qquad \text{(A.3)}$$

where c_p are the expansion coefficients and P is the order of the expansion. Substituting Equation (A.3) into Equation (A.1) results in

$$\mu(E) = c_n\left[\mu(E_o)\right]^n (E - E_0) + \ldots + c_2\left[\mu(E_0)\right]^2 (E - E_0) + \left[c_1(E - E_0) + 1\right]\mu(E_0) + c_0(E - E_0)$$

(A.4)

The order P of the polynomial was found by plotting μ at two different E_s as a function of μ at E_0 using the materials of table A.1 (Figure A.2). Each energy was fitted by polynomials of different orders as shown in Figure A.2. Table A.2 lists the mean, standard deviation, minimum and maximum of the residuals distribution for different energy and *P*. Table A.2 shows no additional benefit in going from third to fourth order polynomial. For this reason Equation (A.4) was truncated to yield

Table A.1. List of radiologically important materials used to develop the post-scatter attenuation. All ρ_e were calculated using $\rho_e = \rho N_A (Z/A)$, where ρ and *Z/A* were taken from Hubbell & Seltzer [144]. $\overline{Z}$ was calculated using $\overline{Z} = \sqrt[b]{a_1 Z_1^b + a_2 Z_2^b + ... + a_n Z_n^b}$ where the a_i is the number of electrons per gram of element Z_i and n is the number of elements. A value of b = 3.1 was employed as was used by Busono and Hussein [24]. Values of μ taken from Hubbell & Seltzer [144]. All quantities for calcium hydroxyapatite were calculated from the elemental composition presented by VanUytven *et al.* [15]

Material	ρ g/cm^3	ρ_e x 10^{23} electrons/cm^3	$\overline{Z}$	μ @ 80 keV	μ @ 70 keV	μ @ 60 keV
Polyethylene	0.93	3.19	5.6	0.1695	0.1764	0.1832
Adipose tissue	0.95	3.18	7.0	0.1710	0.1793	0.1875
Polystyrene	1.06	3.43	5.7	0.1829	0.1905	0.1982
Water, liquid	1.00	3.34	7.5	0.1837	0.1948	0.2059
Muscle, skeletal	1.05	3.48	7.5	0.1914	0.2032	0.2150
Lung tissue	1.05	3.48	7.5	0.1917	0.2037	0.2156
Ovary	1.05	3.49	7.5	0.1919	0.2038	0.2157
Tissue Soft	1.06	3.51	7.5	0.1932	0.2052	0.2171
Glandular tissue	1.09	3.60	7.2	0.1970	0.2085	0.2201
A-150 plastic	1.127	3.73	5.5	0.2032	0.2148	0.2263
PMMA	1.19	3.87	7.0	0.2084	0.2187	0.2290

Table A.1. List of radiologically important materials used to develop the post-scatter attenuation. (Continued)

Material	ρ g/cm^3	ρ_e x 10^{23} electrons/cm^3	$\bar{Z}$	μ @ 80 keV	μ @ 70 keV	μ @ 60 keV
Bakelite	1.25	3.97	6.3	0.2134	0.2233	0.2333
Mylar	1.38	4.33	6.7	0.2339	0.2459	0.2578
Carbon, Graphite	1.7	5.11	6.0	0.2737	0.2859	0.2980
C-552 plastic	1.76	5.30	7.6	0.2927	0.3113	0.3298
B-100 plastic	1.45	4.61	11.8	0.3010	0.3490	0.3970
Teflon	2.25	6.50	8.5	0.3672	0.3951	0.4230
Bone, cortical	1.92	5.95	13.4	0.4280	0.5161	0.6044
Silicon	2.33	6.99	14.0	0.5191	0.6332	0.7472
Aluminum	2.70	7.83	13.0	0.5447	0.6472	0.7498
Calcium Hydroxyapatite	3.16	9.47	16.0	0.8287	1.0651	1.30145

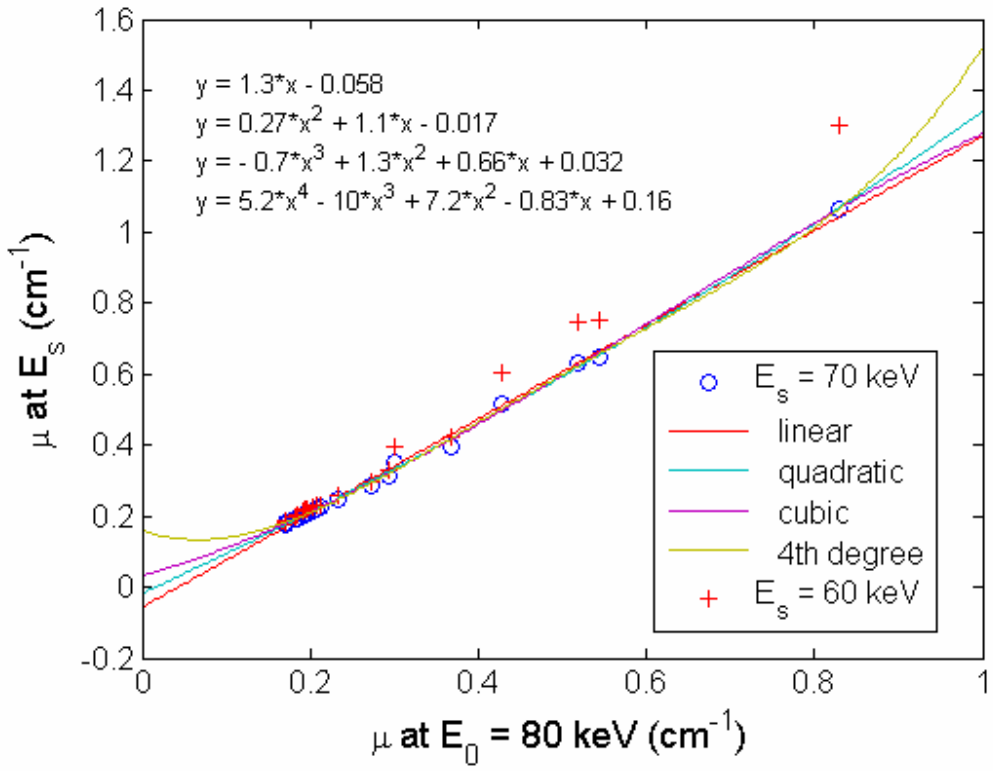

Figure A.2. The μ at scatter energy E_S plotted as a function of μ for a primary energy of 80 keV. Each point corresponds to a specific material in table A.1. The figure also shows fits of different order through the 70 keV data points along with their equations. The corresponding residuals are summarized in table A.2.

Table A.2. Statistical descriptors derived from the residuals (in %) for different energy and exponent *P*.

Descriptor	*E*= 70 keV				*E* = 60 keV			
	P = 1	P = 2	P = 3	P = 4	P = 1	P = 2	P = 3	P = 4
Mean	-0.49	-0.02	0.04	0.05	-0.91	0.04	0.15	0.17
SD	3.99	2.60	2.28	2.37	7.52	4.81	4.13	4.33
Minimum	-5.48	-4.30	-5.69	-5.75	-10.47	-7.55	-10.00	-10.12
Maximum	8.81	5.75	4.86	5.84	16.45	10.73	9.07	10.92

$$\mu(E) = c_3[\mu(E_o)]^3(E - E_0) + c_2[\mu(E_0)]^2(E - E_0) + [c_1(E - E_0) + 1]\mu(E_0) + c_0(E - E_0). \quad \text{(A.5)}$$

The final form of Equation (A.5) does not ensure that $\mu(E)$ goes to zero in the limit when $\mu(E_0)$ approaches zero. Since this has no physical meaning the value of c_0 was set to zero resulting in Equation (A.6).

$$\mu(E) = c_3[\mu(E_o)]^3(E - E_0) + c_2[\mu(E_0)]^2(E - E_0) + [c_1(E - E_0) + 1]\mu(E_0) \quad \text{(A.6)}$$

Equation (A.6) defines $\mu(E)$ as a surface which is a function of E and $\mu(E_0)$, both of which are available and can be used to predict the value of the post-scatter attenuation. The values of the parameters c_1, c_2 and c_3, were obtained by fitting a surface through data points in a [$\mu(E_0)$, E, $\mu(E)$] coordinate space built from a set of radiologically important materials (Table

A.1). The values of the parameters are c_3 = 0.029 ± 0.008 (28%) cm^2 keV^{-1}, c_2 = -0.067 ± 0.008 (12%) cm keV^{-1}, c_1 = 0.007 ± 0.002 (29%) keV^{-1} and result in Equation (4.11).

$$\begin{aligned}\mu(E_s) = &(0.029)[\mu(E_0)]^3(E_s - E_0) \\ &-(0.067)[\mu(E_0)]^2(E_s - E_0) \\ &+[(0.007)(E_s - E_0)+1]\mu(E_0)\end{aligned} \qquad (4.11)$$

Figure A.3 shows the fitted surface of Equation (4.11) along with the points used for the fit.

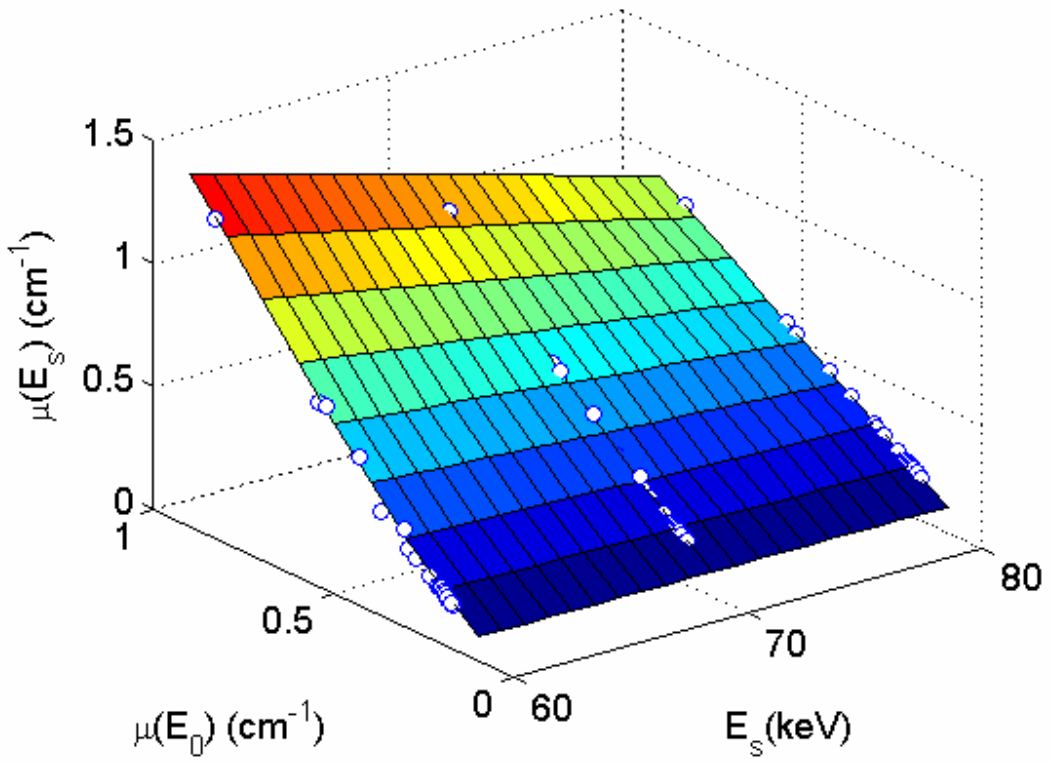

Figure A.3. Fitted surface [(Equation (4.11)] on a [$\mu(E_0)$, E_s, $\mu(E_s)$] space for E_0 = 80 keV. The scatter points correspond to materials in table A.1.

The surface fit (Equation 4.11) and the primary attenuation were used compute the post-scatter attenuation at the lowest energy of scattered photons (~60 keV for E_0=80 keV). Figure A.4 shows a distribution of errors from both approaches. Figure A.4(a) shows the results of the surface fit whose mean error is -0.1% and whose errors range from -8% to 10%. As a comparison, the primary attenuation [Figure A.4(b)] results in a mean error of -15% and ranges from -36% to -8%.

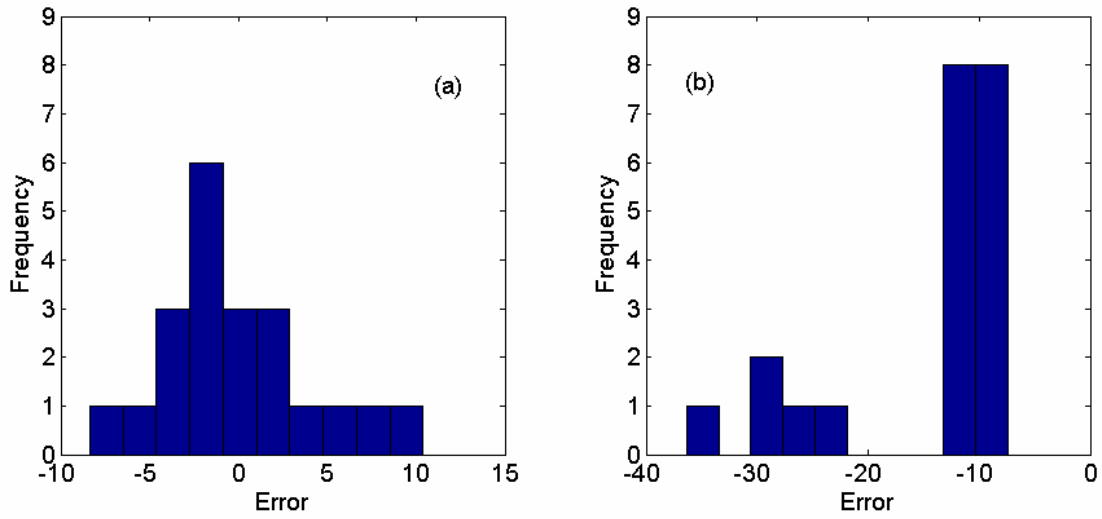

Figure A.4. Distribution of errors for the post scatter attenuation at 60 keV using the surface fit (a) and the primary (b).

Both post-scatter attenuation calculations methods were used in the algorithm described in Chapter 4. Figure A.5 shows the ρ_e reconstructions from AN sinograms of a low resolution version (simulated with 65 x 65 pixels and 144 projections) of phantom B reconstructed using both approaches. Note that this version of phantom B includes an aluminum (Al) insert.

The Al insert provides an additional challenge since it has a larger Z than the rest of the inserts. Table A.3 list the mean ρ_e error for each ROI and post-scatter attenuation approach. The results indicate that the surface fit results in ρ_e errors within -3% to +2% whereas the errors obtained using the primary ranged from -5% to -9%. Similar errors are found using the surface for the higher resolution phantom of Chapter 4.

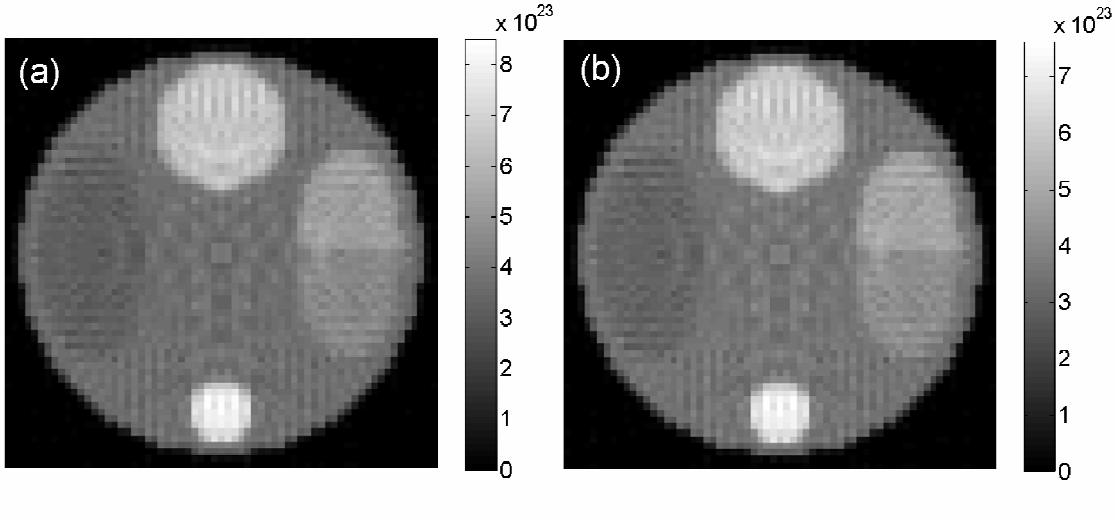

Figure A.5. ρ_e images of a low resolution version of phantom B from Chapter 4. The reconstructions calculated the post-scatter attenuation using the surface fit (a) and the primary image (b). Image units in (electrons/cm^3).

Table A.3. Error (%) of the mean ρ_e for each ROI and post-scatter attenuation method. The ROI labels match those of Chapter 4. A new Al inset is labeled as ROI VI and is located at the central bottom part of the phantom.

ROI	Surface fit	Primary
I: A-150 tissue-equivalent plastic	-0.5	-5.3
II: Polyethylene	-1.2	-6.4
III: Polytetrafluoroethylene, "Teflon"	0.8	-6.6
IV: C-552 Air-equivalent plastic	-0.8	-7.1
V: B-100 Bone-equivalent plastic	-3.1	-9.1
VI: Aluminum	2.3	-7.6

The surface fit was repeated to calculate the parameters that describe the post-scatter attenuation of photons with incident energy of 65 keV. This energy corresponds to the mean energy used in Chapter 5. The values of the surface parameters are c_3 = 0.039 ± 0.006 (15%) cm^2 keV^{-1}, c_2 = -0.088 ± 0.009 (10%) cm keV^{-1} and c_1 = 0.010 ± 0.002 (20%) keV^{-1} and results in Equation (A.7)

$$\begin{aligned}\mu(E_s) = {} & (0.039)[\mu(E_0)]^3(E_s - E_0) \\ & - (0.088)[\mu(E_0)]^2(E_s - E_0) \\ & + [(0.010)(E_s - E_0) + 1]\mu(E_0)\end{aligned} \quad , \qquad \text{(A.7)}$$

where E_0 = 65 keV and c_0 was set to zero to ensure that $\mu(E)$ goes to zero when $\mu(E_0)$ approaches zero. The surface fitted the data with a mean residual of -0.4%, minimum residual of -9.9% and maximum of 11.9%. Using $\mu(E_0)$ results in an overestimation of the attenuation that can be as large as 43.2%. Equation (A.7) was evaluated by reconstructing ρ_e images from single KN scatter sinograms. It was found that the mean error in the ρ_e images of the Shikaliev and the inhomoeneous phantoms increase by only 1% with respect to those using the true post scatter attenuation.

Appendix B.

This appendix contains selected codes (or portions of code) that were used for the electron density reconstructions of this thesis. All codes were written in version 7.1.0.246 (R14) of Matlab.

edrec.m

```
% This is a script that performs ED reconstructions employing the
% algorithm presented in the thesis: "The development and validation of a
% first generation x-ray scatter computed tomography algorithm for the
% reconstruction of electron density breast images using Monte Carlo
% simulation", Written by Jorge Edmundo Alpuche Aviles, 2011

% -------USER INPUTS (Copy and paste in the command window) --------------
% Start of inputs

% % Copy and paste this in the command window. Only copy the text that is
% within the 'Start to inputs' and 'End of inputs'
%
% % recInfo.DescriptionText will display a brief description of the
% current reconstruction. It helps identifying the reconstruction that is
% currently running
recInfo.DescriptionText='Reconstruction of Shikaliev MC simulation with
SICR=(A+B*BS)+(C+D*SQRT(BS))*muL: All scatter,CF65,VS,ZP(1149)';
%
% dataName contains the data for the reconstruction: SinogramMC, K, Im.
% SinogramMC contains the 3D matrix SinogramMC.all which is the scatter
% sinogram  to be reconstructed.
% K contains setup variables like energy, geometry, etc.
% Im must contain Im.noisePIRT (the image of the linear attenuation
% coefficient or mu) and Im.PostMatrix. Im.PostMatrix is a segmentation
% matrix defined as 1 inside the phantom and 0 outside the phantom.
% This matrix could be calculated using the image of mu.
dataName='initialData';

% Load the data. It is preferred that the data file consists of Im, K and
% Sinogram variables. DO NOT EDIT THE FOLLOWING 2 LINES
load(dataName)
load mass_mu mass_mu_liquid_water   % Load the attenuation coefficient of
% water for the calculation of WaterAttenuation below
```

```
% recSinogram is the sinogram to be reconstructed defined once the data
% has been loaded
recSinogram=SinogramMC.all;

% initialName is a common prefix used to create file names for
% consecutive iterations
initialName='Nov192010_2_';

% resultsDataName is used to save the reconstructed electron density
% images, the MRSD of each iteration and the recInfo variable (below)
resultsDataName='MCresultsALL';

% Selects the filter to be used in the FPB step
filter='Ram-Lak';

% Number of initial iteration: it must be an integer larger or equal than
initialIt=1;

% In case initialIt ~=1 then you have to give the current values of MRSD
% MRSD=[];
% load FirstIterationResults.mat

edrec
% End of inputs
%-------------------- Program start----------------------

% Obtain starting date and time
recInfo.StartText=datestr(now);

% Display on screen a general description of the reconstruction as well as
% startting date
disp(recInfo.DescriptionText);
disp(strcat('Starting date:', recInfo.StartText))

% These values are just defined so that we enter the while loop at the
% begginig
initialMRSD=1;
finalMRSD=1;

% Defining the current iteration number and displaying on the screen
itNumber=initialIt;
disp(strcat('Start of iteration:',num2str(itNumber)));

% The current while loop ensures that the algorithm runs according to the
% stopping criteria of section 4.2.5 is
while finalMRSD>10^(-6) & initialMRSD>=finalMRSD

    %
    if itNumber==1

        WaterElectronDensity=3.35*10^23;      % The electron density of
%                                   liquid water (Busono and Hussein 1999)

       % obtaining the mu of water at the incident energy using cubic
```

```
       % spline interpolation
WaterAttenuation=exp(interp1(log(mass_mu_liquid_water(:,1)),log(mass_mu_li
quid_water(:,2)),log(K.Energy),'spline')); % [cm^-1]

% Defining the first electron density estimate
      AssumedRho_e=(WaterElectronDensity/WaterAttenuation)*Im.noisePIRT;

% Setting to zero values that lie outside the object
      AssumedRho_e(Im.PostMatrix==0)=0;

% Initializing SIRT. SIRT is a cell array that will contain the electron
% density images at each iteration. In this case is defining the first
% element in the array equal to initial estimate
        SIRT={AssumedRho_e};
    else

% If the initial iteration is different than one, the current estimate of
% electron density must be defined. In the line below it is made equal to
% the electron density image of the previous iteration
        AssumedRho_e=SIRT{itNumber};

    end % end of the if itNumber==1 conditional


% The line below calls the function rawACF which calculates IdealRay3D
% (Equation 4.2) and RealRay3D (Equation 4.9). The inputs include,
% the current estimate of electron density (AssumedRho_e), the mu image
% (Im.noisePIRT), the setup variable (K) and the current iteration number
[IdealRay3D,RealRay3D,itInfo]=rawACF(AssumedRho_e,Im.noisePIRT,K,itNumber)
;

    % Defining the name of the current iteration and saving its results
    iterationName=strcat(initialName,num2str(itNumber));
    save(iterationName,'IdealRay3D','RealRay3D','itInfo');

% The rec function can be found below and returns the new electron density
% estimate (finalImage).
    finalImage=rec(recSinogram, RealRay3D, IdealRay3D, K.VoxelSize, K.M,
K.VoxelsNumber, K.N0, filter, K.Energy, K.F_FS,
SinogramMC.rayintegral*K.VoxelSize, K.BreastSize);

% Setting to zero values that lie outside the object
    finalImage(Im.PostMatrix==0)=0;

% Update the electron density images variable
    SIRT{itNumber+1}=finalImage;

    % Initilizing the MRSD with a large value to ensure that does more
% than one iteration
    if itNumber==1
        initialMRSD=1;
    else
        initialMRSD=MRSD(itNumber-1);
    end % end of the if itNumber==1 conditional
```

```
    % Calculating the MRSD (Equation 4.10) after the iteration
    finalMRSD=sum(((SIRT{itNumber+1}(Im.PostMatrix~=0)-
SIRT{itNumber}(Im.PostMatrix~=0))./SIRT{itNumber}(Im.PostMatrix~=0)).^2)/l
ength(SIRT{itNumber}(Im.PostMatrix~=0))

% Store the values of MRSD for each iteration
    MRSD=[MRSD, finalMRSD];

% Save the results
    save(resultsDataName, 'SIRT', 'MRSD');

% Display the end of the iteration along with the current MRSD
    disp(strcat('End of iteration ',num2str(itNumber)));
    disp(strcat('MRSD= ',num2str(finalMRSD)));

% Next iterations
    itNumber=itNumber+1;

end % This is the end of the while loop

% This line is achieved when the algorithm has stopped iterating

% Finally, store the reconstruction information and the results
recInfo.EndText=datestr(now);
recInfo.iterationsNumber=length(SIRT)-1;
save(resultsDataName, 'SIRT','MRSD','recInfo');
```

rec.m

```
function y=rec(Sinogram3D, RealRay3D, IdealRay3D, VoxelSize, M,
VoxelsNumber, N0, filter, Energy, F, pSinogram, BreastSize)
%
% This is a function that takes the measured scatter sinogram and
% reconstructs a scattering image. The scatter sinogram of each
% detector is corrected using the Primary CT image. The "corrected
% sinogram" is then used to computed the "ideal integrated sinogram" by
% integrating each detector's sinogram. This is finally fed into the
% FBP algorithm to reach the electron density image.
%
% INPUTS:
% - Sinogram3D: The measured scatter sinogram
% - RealRay3D: Equation 4.9
% - IdealRay3D: Equation 4.2
% - VoxelSize: the size of the voxel in cm
% - M: The # of projections
% - VoxelsNumber: The number of voxels in a single dimension
% - N0: # of incident photons
% - filter: FBP reconstruction filter
% - Energy: Energy (in keV) of the incident beam
% - F: Fraction of photons measured by the ring (Figs 4.11 & 5.9)
% - pSinogram: The primary sonogram (Equation 3.25)
% - BreastSize: The diameter of the breast
% OUTPUT:
% - y: The electron density image

% Calculating the dimensions of the sinogram
```

```
 [d1 d2 d3]=size(Sinogram3D);
%
% Calculating the attenuation correction factors (Fd variable). These will
% correct each ray that hits a detector. It is of the same dimensions as
% Sinogram3D
Fd=zeros(d1,d2,d3);
for i=1:d1
      for j=1:d2
            for k=1:d3
                  if RealRay3D(i,j,k)==0
                        Fd(i,j,k)=0;
                  else
                        Fd(i,j,k)=IdealRay3D(i,j,k)/RealRay3D(i,j,k);
                  end
            end
      end
end

% Calculating the attenuation corrected sinogram (See Fig 5.2)
CorrectedSinogram=Fd.*Sinogram3D;
%
% Integrating the ring or the detectors. It is integrated along the third
% dimension of the array since it represents each detector (See Fig 5.2).
% At this point, IntSinogram is equal to Eq. 4.5
IntSinogram=sum(CorrectedSinogram,3);

% Calculating the SICR (Eq. 5.14)
new_sicr = (0.7824 - 0.0217*BreastSize) + ...
            (-0.194 + 0.0391*sqrt(BreastSize) )*pSinogram;
%
% Calculating the constants in front of the electron density ray integral
% in Eq. 4.5. Note that VoxelSize is inside the integral (is the dy
% differential)
const=(N0*F*VoxelSize*cross_section(Energy));

% SICR correction before step 5 of Fig 5.2
IntSinogram=(new_sicr.*IntSinogram)/const;

% calculating the projection angles
theta=0:(360/M):(360-360/M);

% FPB (Step 5 of Fig. 5.2)
y=iradon(IntSinogram',theta, filter,VoxelsNumber);
disp(filter)
```

Notes regarding rawACF.m

The function edrec.m (above) calls the function rawACF.m to calculate equations (4.2) and (4.9). This function however is too long to be included in this dissertation. Function

rawACF.m primarily conducts the geometric calculations needed to define Figure 3.3 and the procedure of section 3.4.1. The following list summarizes the most relevant steps performed by this function.

1. Calculate the coordinates of the x-ray beam start and end point. This defines the 'Incident beam" of Figure 3.3.
2. Call the ray tracer algorithm of Siddon [132] to identify the voxels traversed by the incident beam. This defines the voxels that can produce scatter.
3. For each intersected voxel. Calculate the coordinates of the centre of the voxel and the centre of each scatter detector
    a. Equation (4.2) calculation. At this point there is enough information (geometry) to calculate the terms of Equation (4.2).
    b. Equation (4.9) calculation. The first exponential is calculated using the μ image and the length of voxel intersection returned by Siddon's algorithm. The post-scatter attenuation is calculated by calling the ray tracer algorithm to identify the voxels traversed by the scattered beam. This set of voxels is used to calculate the second exponential of Equation (4.9) using Equation (4.11) or Equation (A.7).
4. Move to the next intersected voxel and repeat step 3 until all intersected voxels have been used. This represents the integral along the beam.

References

1. Canadian Cancer Society. *General cancer statistics*. Canadian Cancer Encyclopedia 2010, August 17, 2010; Available at: www.cancer.ca.
2. Canadian Cancer Society (2010) *Breast cancer stats*. January 15, 2010; Available at: www.cancer.ca.
3. K. Decker and K. Watters, *Biennial report 2006-2008*, Manitoba Breast Screening Program, CancerCare Manitoba: Winnipeg. p. 24.
4. U.S. Preventive Services Task Force (2009) *Screening for Breast Cancer: Recommendation Statement*. AHRQ Publication No. 10-05142-EF-2.
5. L.L. Humphrey, M. Helfand, B.K. Chan and S.H. Woolf, *Breast cancer screening: a summary of the evidence for the U.S. Preventive Services Task Force.* Ann of Intern Med, 2002. **137**(5 Part 1): p. 347-60.
6. Public Health Agency of Canada (2008), *Organized Breast Cancer Screening Programs in Canada - Report on Program Performance in 2003 and 2004*, HP32-1/2004E-PDF.
7. W. Huda and R. Slone, *Review of radiologic physics*. Second ed. 2003: Lippincott Williams & Wilkins.p. 104-20.
8. A. Karellas, J.Y. Lo and C.G. Orton, *Cone beam x-ray CT will be superior to digital x-ray tomosynthesis in imaging the breast and delineating cancer.* Med Phys, 2008. **35**(2): p. 409-411.
9. J.M. Boone, T.R. Nelson, K.K. Lindfors and J.A. Seibert, *Dedicated breast CT: radiation dose and image quality evaluation.* Radiology, 2001. **221**(3): p. 657-67.

10. P.C. Johns and M.J. Yaffe, *X-ray characterisation of normal and neoplastic breast tissues.* Phys Med Biol, 1987. **32**(6): p. 675-95.

11. K.K. Lindfors, J.M. Boone, T.R. Nelson, K. Yang, A.L.C. Kwan and D.F. Miller, *Dedicated Breast CT: Initial Clinical Experience1.* Radiology, 2008. **246**(3): p. 725-733.

12. B.B. Muir, J. Lamb, T.J. Anderson and A.E. Kirkpatrick, *Microcalcification and its relationship to cancer of the breast: experience in a screening clinic.* Clin Radiol, 1983. **34**(2): p. 193-200.

13. J.M. Guinebretiere, E. Menet, A. Tardivon, P. Cherel and D. Vanel, *Normal and pathological breast, the histological basis.* Eur J Radiol, 2005. **54**(1): p. 6-14.

14. R.C. Chen, R. Longo, L. Rigon, F. Zanconati, A De Pellegrin, R.-H. Menk, E. Vallaza, T. Q. Xiao and E. Castelli, *Measurement of the linear attenuation coefficients of breast tissues by synchrotron radiation computed tomography.* Phys Med Biol, 2010. **55**(17): p. 4993.

15. E. Van Uytven, S. Pistorius and R. Gordon, *A method for 3D electron density imaging using single scattered x-rays with application to mammographic screening.* Phys Med Biol, 2008. **53**(19): p. 5445-59.

16. E. Van Uytven, S. Pistorius and R. Gordon, *An iterative three-dimensional electron density imaging algorithm using uncollimated compton scattered x rays from a polyenergetic primary pencil beam.* Med Phys, 2007. **34**(1): p. 256-65.

17. P.J. Arsenault and E.M.A. Hussein, *Image Reconstruction From the Compton Scattering of X-Ray Fan Beams in Thick/Dense Objects.* IEEE Trans Nucl Sci, 2006. **53**(3): p. 1622-1633.

18. F.E. Khettabi, E.M.A. Hussein and H.A. Jama, *A nonrotating multiparameter 3-D X-ray imaging system-Part I: modeling and reconstruction.* IEEE Trans Nucl Sci, 2004. **51**(3): p. 641-647.

19. B. Golosio, A. Simionovici, A. Somogyi, L. Lemelle, M. Chukalina and A. Brunetti, *Internal elemental microanalysis combining x-ray fluorescence, Compton and transmission tomography.* J Appl Phys, 2003. **94**(1): p. 145-156.

20. F.E. Khettabi and E.M.A. Hussein, *An inverse problem for three-dimensional x-ray scatter/transmission imaging.* Inverse Probl, 2003. **19**(2): p. 477.

21. B. Golosio, A. Brunetti and R. Cesareo, *Correction for X-ray absorption in compton tomography.* J. Phys. IV France 2003. **104**: p. 651-654.

22. J. Wang, X. Huang and X. Zhong, *The convergence condition of the successive approximation process in Compton scattering tomography.* J Appl Phys, 2002. **92**(4): p. 2149-2152.

23. A. Brunetti and B. Golosio, *Software for X-ray fluorescence and scattering tomographic reconstruction.* Comput Phys Commun, 2001. **141**(3): p. 412-425.

24. P. Busono and E.M.A. Hussein, *Algorithms for density and composition-discrimination imaging for fourth-generation CT systems.* Phys Med Biol, 1999. **44**(6): p. 1455-77.

25. T. Yuasa, M. Akiba, T. Takeda, M. Kazama, A. Hoshino, Y. Watanabe, K. Hyodo, F.A. Dilmanian, T. Akatsuka and Y. Itai, *Incoherent-scatter computed tomography with monochromatic synchrotron x ray: feasibility of multi-CT imaging system for simultaneous measurement-of fluorescent and incoherent scatter x rays.* IEEE Trans Nucl Sci, 1997. **44**(5): p.:1760-1769.

26. G. Harding, *Inelastic photon scattering: Effects and applications in biomedical science and industry.* Radiat Phys Chem, 1997. **50**(1): p. 91-111.

27. N.V. Arendtsz and E.M.A. Hussein, *Energy-spectral Compton scatter imaging. I. Theory and mathematics.* IEEE Trans Nucl Sci, 1995. **42**(6): p. 2155-2165.

28. N.V. Arendtsz and E.M.A. Hussein, *Energy-spectral Compton scatter imaging. II. Experiments.* IEEE Trans Nucl Sci, 1995. **42**(6): p. 2166-2172.

29. S.J. Norton, *Compton scattering tomography.* J Appl Phys, 1994. **76**(4): p. 2007-2015.

30. G. Harding and R. Tischler, *Dual-energy Compton scatter tomography.* Phys Med Biol, 1986. **31**(5): p. 477-89.

31. L. Brateman, A.M. Jacobs and L.T. Fitzgerald, *Compton scatter axial tomography with x-rays: SCAT-CAT.* Phys Med Biol, 1984. **29**(11): p. 1353-70.

32. J.J. Battista and M.J. Bronskill, *Compton scatter imaging of transverse sections: an overall appraisal and evaluation for radiotherapy planning.* Phys Med Biol, 1981. **26**(1): p. 81-99.

33. R.L. Clarke and G. Van Dyk, *A new method for measurement of bone mineral content using both transmitted and scattered beams of gamma-rays.* Phys Med Biol, 1973. **18**(4): p. 532-9.

34. F.T. Farmer and M.P. Collins, *A new approach to the determination of anatomical cross-sections of the body by Compton scattering of gamma-rays.* Phys Med Biol, 1971. **16**(4): p. 577-86.

35. P.G. Lale, *The examination of internal tissues, using gamma-ray scatter with a possible extension to megavoltage radiography.* Phys Med Biol, 1959. **4**: p. 159-67.

36. M. Torikoshi, T. Tsunoo, M. Sasaki, M. Endo, Y. Noda, Y. Ohno, T. Kohno, K. Hyodo, K. Uesugi and N. Yagi, *Electron density measurement with dual-energy x-ray CT using synchrotron radiation.* Phys Med Biol, 2003. **48**(5): p. 673-85.

37. J.E. Alpuche Aviles, S. Pistorius, R. Gordon and I.A. Elbakri, *A novel hybrid reconstruction algorithm for first generation incoherent scatter CT (ISCT) of large objects with potential medical imaging applications.* J Xray Sci Technol, 2011. **19**(1): p. 35-56.

38. Q. Zhihua, J. Zambelli, N. Bevins and G.-H. Chen, *Quantitative imaging of electron density and effective atomic number using phase contrast CT.* Phys Med Biol, 2010. **55**(9): p. 2669.

39. E.A. Ryan, M.J. Farquharson and D.M. Flinton, *The use of Compton scattering to differentiate between classifications of normal and diseased breast tissue.* Phys Med Biol, 2005. **50**(14): p. 3337-48.

40. J.S. al-Bahri and N.M. Spyrou, *Electron density of normal and pathological breast tissues using a Compton scattering technique.* Appl Radiat Isot, 1998. **49**(12): p. 1677-84.

41. E.A. Ryan and M.J. Farquharson, *Breast tissue classification using x-ray scattering measurements and multivariate data analysis.* Phys Med Biol, 2007. **52**(22): p. 6679-96.

42. M. Antoniassi, A.L.C. Conceição and M.E. Poletti, *Characterization of breast tissues using Compton scattering.* Nucl Instrum Methods Phys Res A, 2010. **619**(1-3): p. 375-378.

43. Y. Chen, B. Liu, J.M. O'Connor, C. S. Didier, and S. J. Glick., *Characterization of scatter in cone-beam CT breast imaging: Comparison of experimental measurements and Monte Carlo simulation.* Med Phys, 2009. **36**(3): p. 857-869.

44. A.L.C. Kwan, J.M. Boone and N. Shah, *Evaluation of x-ray scatter properties in a dedicated cone-beam breast CT scanner.* Med Phys, 2005. **32**(9): p. 2967-75.

45. W.A. Berg, J.D. Blume, J.B. Cormack, E.B. Mendelson, D. Lehrer, M. Bohm-Velez, E.D. Pisano, R.A. Jong, W.P. Evans, M.J. Morton, M.C. Mahoney, L. Hovanessian Larsen, R.G. Barr, D.M. Farria, H.S. Marques, K. Boparai and A.I. for the, *Combined Screening With Ultrasound and Mammography vs Mammography Alone in Women at Elevated Risk of Breast Cancer.* JAMA, 2008. **299**(18): p. 2151-2163.

46. C. K. Glide-Hurst, A.D.A.Maidmetn and C.G. Orton, *Ultrasonography is soon likely to become a viable alternative to x-ray mammography for breast cancer screening.* Med Phys, 2010. **37**(9): p. 4525-4528.

47. A. Karellas and S. Vedantham, *Breast cancer imaging: a perspective for the next decade.* Med Phys, 2008. **35**(11): p. 4878-97.

48. C.K. Kuhl, *Current status of breast MR imaging. Part 2. Clinical applications.* Radiology, 2007. **244**(3): p. 672-91.

49. C. Kuhl, *The current status of breast MR imaging. Part I. Choice of technique, image interpretation, diagnostic accuracy, and transfer to clinical practice.* Radiology, 2007. **244**(2): p. 356-78.

50. D. Saslow, C. Boetes, W. Burke, S. Harms, M.O. Leach, C.D. Lehman, E. Morris, E. Pisano, M. Schnall, S. Sener, R.A. Smith, E. Warner, M. Yaffe, K.S. Andrews and

C.A. Russell, *American Cancer Society guidelines for breast screening with MRI as an adjunct to mammography.* CA Cancer J Clin, 2007. **57**(2): p. 75-89.

51. F. Benard and E. Turcotte, *Imaging in breast cancer: Single-photon computed tomography and positron-emission tomography.* Breast Cancer Res, 2005. **7**(4): p. 153-62.

52. L.T. Niklason, B.T. Christian, L.E. Niklason, D.B. Kopans, D.E. Castleberry, B.H. Opsahl-Ong, C.E. Landberg, P.J. Slanetz, A.A. Giardino, R. Moore, D. Albagli, M.C. DeJule, P.F. Fitzgerald, D.F. Fobare, B.W. Giambattista, R.F. Kwasnick, J. Liu, S.J. Lubowski, G.E. Possin, J.F. Richotte, C.Y. Wei and R.F. Wirth, *Digital tomosynthesis in breast imaging.* Radiology, 1997. **205**(2): p. 399-406.

53. A.E. Burgess, F.L. Jacobson and P.F. Judy, *Human observer detection experiments with mammograms and power-law noise.* Med Phys, 2001. **28**(4): p. 419-37.

54. X. Gong, S.J. Glick, B. Liu, A.A. Vedula and S. Thacker, *A computer simulation study comparing lesion detection accuracy with digital mammography, breast tomosynthesis, and cone-beam CT breast imaging.* Med Phys, 2006. **33**(4): p. 1041-52.

55. J.T. Dobbins, 3rd and D.J. Godfrey, *Digital x-ray tomosynthesis: current state of the art and clinical potential.* Phys Med Biol, 2003. **48**(19): p. R65-106.

56. M.S. Christina, S. Ehsan and Y.L. Joseph, *The quantitative potential for breast tomosynthesis imaging.* Med Phys, 2010. **37**(3): p. 1004-1016.

57. J.T. Bushberg, *The essential physics of medical imaging*. 2002, Philadelphia: Lippincott Williams & Wilkins. p. 191-229.

58. J.M. Boone, *Glandular breast dose for monoenergetic and high-energy X-ray beams: Monte Carlo assessment.* Radiology, 1999. **213**(1): p. 23-37.

59. A.D. Maidment, R. Fahrig and M.J. Yaffe, *Dynamic range requirements in digital mammography.* Med Phys, 1993. **20**(6): p. 1621-33.

60. M. Hayat, *Cancer imaging: Lung and breast carcinomas*. 2008: Academic Press. p. 383-92.

61. J. Law, *Measurement of focal spot size in mammography X-ray tubes.* Br J Radiol, 1993. **66**(781): p. 44-50.

62. E.D. Pisano, C. Gatsonis, E. Hendrick, M. Yaffe, J.K. Baum, S. Acharyya, E.F. Conant, L.L. Fajardo, L. Bassett, C. D'Orsi, R. Jong and M. Rebner, *Diagnostic performance of digital versus film mammography for breast-cancer screening.* N Engl J Med, 2005. **353**(17): p. 1773-83.

63. P.S. Rezentes, A. de Almeida and G.T. Barnes, *Mammography grid performance.* Radiology, 1999. **210**(1): p. 227-32.

64. D.R. Dance and G.J. Day, *The computation of scatter in mammography by Monte Carlo methods.* Phys Med Biol, 1984. **29**(3): p. 237-47.

65. J.M. Boone, K.K. Lindfors, V.N. Cooper, 3rd and J.A. Seibert, *Scatter/primary in mammography: comprehensive results.* Med Phys, 2000. **27**(10): p. 2408-16.

66. N. Maalej, M. Kafi, A. Nobah and A. Naqvi, *Air Gap Effect on Mammography Image Quality*, in *World Congress on Med Phys and Biomedical Engineering 2006*, R. Magjarevic and J.H. Nagel, Editors. 2007, Springer Berlin Heidelberg. p. 1401-1404.

67. D.R. Dance, *Monte Carlo calculation of conversion factors for the estimation of mean glandular breast dose.* Phys Med Biol, 1990. **35**(9): p. 1211-9.

68. X. Wu, G.T. Barnes and D.M. Tucker, *Spectral dependence of glandular tissue dose in screen-film mammography.* Radiology, 1991. **179**(1): p. 143-8.

69. X. Gong, A.A. Vedula and S.J. Glick, *Microcalcification detection using cone-beam CT mammography with a flat-panel imager.* Phys Med Biol, 2004. **49**(11): p. 2183-95.

70. S.J. Glick, *Breast CT.* Annu Rev Biomed Eng, 2007. **9**: p. 501-26.

71. C.A. Beam, E.F. Conant and E.A. Sickles, *Association of volume and volume-independent factors with accuracy in screening mammogram interpretation.* J Natl Cancer Inst, 2003. **95**(4): p. 282-90.

72. C.A. Beam, E.F. Conant and E.A. Sickles, *Factors affecting radiologist inconsistency in screening mammography.* Acad Radiol, 2002. **9**(5): p. 531-40.

73. C.F. Nodine, H.L. Kundel, C. Mello-Thoms, S.P. Weinstein, S.G. Orel, D.C. Sullivan and E.F. Conant, *How experience and training influence mammography expertise.* Acad Radiol, 1999. **6**(10): p. 575-85.

74. P. Taylor, J. Champness, R. Given-Wilson, K. Johnston and H. Potts, *Impact of computer-aided detection prompts on the sensitivity and specificity of screening mammography.* Health Technol Assess, 2005. **9**(6): p. iii, 1-58.

75. K.J. Jørgensen, P.-H. Zahl and P.C. Gøtzsche, *Breast cancer mortality in organised mammography screening in Denmark: comparative study.* BMJ. **340**.

76. R.L. McKinley and M.P. Tornai, *Preliminary investigation of dose for a dedicated mammotomography system.* Proc SPIE: Physics of Medical Imaging 2006. **6142**: p. 614208.

77. R. Ning, D. Conover, Y. Yu, Y. Zhang, W. Cai, X. Lu and R. Betancourt-Benitez. *A novel cone beam breast CT scanner: Preliminary system evaluation*. Proc SPIE: Physics of Medical Imaging, 2006. **6142**: p. 614211.

78. C.C. Shaw, C. Lingyun, M.C. Altunbas, T. Shuju, W. Tian-Peng, L. Xinming, L. Chao-Jen, S.C. Kappadath and M. Yang. *Cone Beam Breast CT with a Flat Panel Detector- Simulation, Implementation and Demonstration*. Conf Proc IEEE Eng Med Biol Soc, 2005; 4:4461-4.

79. A. O'Connell, D.L. Conover, Y. Zhang, P. Seifert, W. Logan-Young, C.F. Lin, L. Sahler and R. Ning, *Cone-beam CT for breast imaging: Radiation dose, breast coverage, and image quality*. AJR Am J Roentgenol, 2010. **195**(2): p. 496-509.

80. I. Sechopoulos, S. C. J. Feng and C. J. D'Orsi, *Dosimetric characterization of a dedicated breast computed tomography clinical prototype.* Med Phys, 2010. **37**(8): p. 4110-4120.

81. D.C. Crotty, R. L. Mckinley and M. P. Tornai. *Experimental spectral measurements of heavy K-edge filtered beams for x-ray computed mammotomography*. Proc SPIE: Physics of Medical Imaging, 2006. **6142**: p. 61421V.

82. R.L. McKinley, M.P. Tornai, E. Samei and M.L. Bradshaw, *Simulation study of a quasi-monochromatic beam for x-ray computed mammotomography.* Med. Phys., 2004. **31**(4): p. 800-813.

83. A. Kwan, N. Shah, G. Burkett, J.A. Seibert, K.K. Lindfors, T.R. Nelson and J.M. Boone. *Progress in the development of a dedicated breast CT scanner*. Proc SPIE: Physics of Medical Imaging, 2004. **5368**: p. 304-310.

84. A.L. Kwan, J.M. Boone, K. Yang and S.Y. Huang, *Evaluation of the spatial resolution characteristics of a cone-beam breast CT scanner.* Med Phys, 2007. **34**(1): p. 275-81.

85. K. Yang, A.L. Kwan and J.M. Boone, *Computer modeling of the spatial resolution properties of a dedicated breast CT system.* Med Phys, 2007. **34**(6): p. 2059-69.

86. S. J. Glick, S. Thacker, X. Gong and B. Liu, *Evaluating the impact of x-ray spectral shape on image quality in flat-panel CT breast imaging.* Med Phys, 2007. **34**(1): p. 5-24.

87. S. Pani, R. Longo, D. Dreossi, F. Montanari, A. Olivo, F. Arfelli, A. Bergamaschi, P. Poropat, L. Rigon, F. Zanconati, L.D. Palma and E. Castelli, *Breast tomography with synchrotron radiation: preliminary results.* Phys Med Biol, 2004. **49**(9): p. 1739-1754.

88. V. Vinh-Hung and R. Gordon, *Quantitative target sizes for breast tumor detection prior to metastasis: a prerequisite to rational design of 4D scanners for breast screening.* Technol Cancer Res Treat, 2005. **4**(1): p. 11-21.

89. X. Gong, A.A. Vedula and S.J. Glick, *Microcalcification detection using cone-beam CT mammography with a flat-panel imager.* Phys Med Biol, 2004. **49**(11): p. 2183-95.

90. K. Chida, Y. Komatsu, M. Sai, A. Nakagami, T. Yamada, T. Yamashita, I. Mori, T. Ishibashi, S. Maruoka and M. Zuguchi, *Reduced compression mammography to reduce breast pain.* Clin Imaging, 2009. **33**(1): p. 7-10.

91. R.S. Saunders, Jr. and E. Samei, *The effect of breast compression on mass conspicuity in digital mammography.* Med Phys, 2008. **35**(10): p. 4464-73.

92. M. Elwood, B. McNoe, T. Smith, M. Bandaranayake and T.C. Doyle, *Once is enough--why some women do not continue to participate in a breast cancer screening programme.* N Z Med J, 1998. **111**(1066): p. 180-3.

93. S.C. Thacker and S.J. Glick, *Normalized glandular dose (DgN) coefficients for flat-panel CT breast imaging.* Phys Med Biol, 2004. **49**(24): p. 5433-44.

94. S. Richard and E. Samei, *Quantitative breast tomosynthesis: From detectability to estimability.* Med Phys, 2010. **37**(12): p. 6157-6165.

95. R. Samuel and S. Ehsan, *Quantitative imaging in breast tomosynthesis and CT: Comparison of detection and estimation task performance.* Med Phys, 2010. **37**(6): p. 2627-2637.

96. J.M. Boone, *Radiological interpretation 2020: toward quantitative image assessment.* Med Phys, 2007. **34**(11): p. 4173-9.

97. D.S. Anikonov, V.G. Nazarov and I.V. Prokhorov, *Poorly visible media in x-ray tomography*. Inverse and ill-posed problem series. 2002, Utrecht, The Netherlands: VSP.

98. M.C. Altunbas, C.C. Shaw, L. Chen, C. Lai, X. Liu, T. Han and T. Wang, *A post-reconstruction method to correct cupping artifacts in cone beam breast computed tomography.* Med Phys, 2007. **34**(7): p. 3109-3118.

99. B. Chen and R. Ning, *Cone-beam volume CT breast imaging: Feasibility study.* Med Phys, 2002. **29**(5): p. 755-770.

100. R.B. Benitez, R. Ning, D. Conover and S. Liu, *NPS characterization and evaluation of a cone beam CT breast imaging system.* J Xray Sci Technol, 2009. **17**(1): p. 17-40.

101. K. Yang, A. L. C. Kwan, S.-Y. Huang, N. J. Packard and J. M. Boone, *Noise power properties of a cone-beam CT system for breast cancer detection.* Med Phys, 2008. **35**(12): p. 5317-5327.

102. J. Q. Xia, J. Y. Lo, K. Yang, C. E. Floyd, Jr. and J. M. Boone, *Dedicated breast computed tomography: Volume image denoising via a partial-diffusion equation based technique.* Med Phys, 2008. **35**(5): p. 1950-1958.

103. C.-J. Lai, C.C. Shaw, L. Chen, M.C. Altunbas, X. Liu, T. Han, T. Wang, W.T. Yang, G.J. Whitman and S.-J. Tu, *Visibility of microcalcification in cone beam breast CT: Effects of x-ray tube voltage and radiation dose.* Med Phys, 2007. **34**(7): p. 2995-3004.

104. J.J. Battista, L.W. Santon and M.J. Bronskill, *Compton scatter imaging of transverse sections: corrections for multiple scatter and attenuation.* Phys Med Biol, 1977. **22**(2): p. 229-44.

105. J.J. Battista and M.J. Bronskill, *Compton-scatter tissue densitometry: calculation of single and multiple scatter photon fluences.* Phys Med Biol, 1978. **23**(1): p. 1-23.

106. T.H. Prettyman, R.P. Gardner, J.C. Russ and K. Verghese, *A combined transmission and scattering tomographic approach to composition and density imaging.* Appl Radiat Isot, 1993. **44**(10/11): p. 1327-1341.

107. F.E. Khettabi, I. Yaar and E.M. Hussein, *A three-dimensional x-ray scattering system for multi-parameter imaging of the human head.* Phys Med Biol, 2003. **48**(20): p. 3445-58.

108. H.A. Jama, E.M.A. Hussein and F.E. Khettabi, *A nonrotating multiparameter 3-D X-ray imaging system-Part II: Design and Experiments.* IEEE Trans Nucl Sci, 2004. **51**(3): p. 648-658.

109. X. Pan, E.Y. Sidky and M. Vannier, *Why do commercial CT scanners still employ traditional, filtered back-projection for image reconstruction?* Inverse Probl, 2009. **25**(12): p. 123009.

110. J. Wang, Z. Chi and Y. Wang, *Analytic reconstruction of Compton scattering tomography.* J Appl Phys, 1999. **86**(3): p. 1693-1698.

111. C.A. Carlsson, *Imaging modalities in x-ray computerized tomography and in selected volume tomography.* Phys Med Biol, 1999. **44**(3): p. R23-56.

112. J.M. Boone, J.A. Seibert, C.M. Tang and S.M. Lane, *Grid and slot scan scatter reduction in mammography: comparison by using Monte Carlo techniques.* Radiology, 2002. **222**(2): p. 519-27.

113. G.H. Glover, *Compton scatter effects in CT reconstructions.* Med Phys, 1982. **9**(6): p. 860-7.

114. P.M. Joseph and R.D. Spital, *The effects of scatter in x-ray computed tomography.* Med Phys, 1982. **9**(4): p. 464-72.

115. S.H. Evans, D.A. Bradley, D.R. Dance, J.E. Bateman and C.H. Jones, *Measurement of small-angle photon scattering for some breast tissues and tissue substitute materials.* Phys Med Biol, 1991. **36**(1): p. 7-18.

116. D.E. Peplow and K. Verghese, *Measured molecular coherent scattering form factors of animal tissues, plastics and human breast tissue.* Phys Med Biol, 1998. **43**(9): p. 2431-52.

117. G. Kidane, R.D. Speller, G.J. Royle and A.M. Hanby, *X-ray scatter signatures for normal and neoplastic breast tissues.* Phys Med Biol, 1999. **44**(7): p. 1791-1802.

118. A. Olivo, F. Arfelli, D. Dreossi, R. Longo, R.H. Menk, S. Pani, P. Poropat, L. Rigon, F. Zanconati and E. Castelli, *Preliminary study on extremely small angle x-ray scatter imaging with synchrotron radiation.* Phys Med Biol, 2002. **47**(3): p. 469-80.

119. M.E. Poletti, D. Goncalves and I. Mazzaro, *X-ray scattering from human breast tissues and breast-equivalent materials.* Phys Med Biol, 2002. **47**(1): p. 47-63.

120. R.J. LeClair, M.M. Boileau and Y. Wang, *A semianalytic model to extract differential linear scattering coefficients of breast tissue from energy dispersive x-ray diffraction measurements.* Med Phys, 2006. **33**(4): p. 959-67.

121. G. Harding, J. Kosanetzky and U. Neitzel, *X-ray diffraction computed tomography.* Med Phys, 1987. **14**(4): p. 515-25.

122. E. Van Uytven, *3D Electron Density Imaging using Single Scattered X rays with Application to Breast CT and Mammographic Screening*, Ph.D. Thesis submitted in the *Department of Physics & Astronomy*, University of Manitoba: Winnipeg. 2007.

123. F.H. Attix, *Introduction to radiological physics and radiation dosimetry*. 1986: John Wiley, p. 156.

124. R.D. Evans, *The Atomic Nucleus*. International Series in Pure and Particle Physics, ed. L.I. Schiff. 1955: McGraw-Hill Book Company, Inc., p. 695-701.

125. E.B. Podgorsak, *Radiation Physics for Medical Physicists*. 2006, Springer. p. 404-407.

126. E.B. Podgorsak, *Radiation Physics for Medical Physicists*. 2006, Springer. p. 26.

127. A. Das and T. Ferbek, *Introduction to Nuclear and Particle Physics*. 1994: John Wiley & Sons, Inc., p. 15-17.

128. E.B. Podgorsak, *Radiation Physics for Medical Physicists*. 2006, Springer. p. 322-325.

129. J.H. Hubbell, W.J. Veigele, E.A. Briggs, R.T. Brown, D.T. Cromer and R.J. Howerton, *Atomic form factors, incoherent scattering functions, and photon scattering cross sections.* J Phys Chem Ref Data, 1975. **4**(3): p. 471-538.

130. A.C. Kak and M. Slaney, *Principles of Computerized Tomographic Imaging*. 1988, New York: IEEE Press. p. 49-75.

131. A.C. Kak and M. Slaney, *Principles of Computerized Tomographic Imaging*. 1988, New York: IEEE Press. p. 177-186.

132. R.L. Siddon, *Fast calculation of the exact radiological path for a three-dimensional CT array.* Med Phys, 1985. **12**(2): p. 252-5.

133. G.F. Knoll, *Radiation detection and measurement*. Third edition ed. 2000: Wiley. p. 116-119.

134. F. Verhaegen and J. Seuntjens, *Monte Carlo modelling of external radiotherapy photon beams.* Phys Med Biol, 2003. **48**(21): p. R107-64.

135. G. Jarry, S.A. Graham, D.J. Moseley, D.J. Jaffray, J.H. Siewerdsen and F. Verhaegen, *Characterization of scattered radiation in kV CBCT images using Monte Carlo simulations.* Med Phys, 2006. **33**(11): p. 4320-9.

136. I. Kawrakow and D.W.O. Rogers, *The EGSnrc Code System: Monte Carlo Simulation of Electron and Photon Transport*, in *Ionizing Radiation Standards*. 2006, National Research Council of Canada: Ottawa, Canada.

137. B. Walters, I. Kawrakow and D.W.O. Rogers, *DOSXYZnrc Users Manual* in *Ionizing Radiation Standards*. 2007, National Research Council of Canada: Ottawa, Canada.

138. D.W.O. Rogers, I. Kawrakow, J.P. Seuntjens, B.R.B. Walters and E. Mainegra-Hing, *NRC User Codes for EGSnrc*, in *Ionizing Radiation Standards*. 2005, National Research Council of Canada: Ottawa, Canada.

139. G.-F. Rust and J. Weigelt, *X-ray fluorescent computer tomography with synchrotron radiation.* IEEE Trans Nucl Sci, 1998. **45**(1): p. 75- 88.

140. J.P.G. Hogan, R.A.; Krieger, A.S., *Fluorescent Computer Tomography: A Model For Correction Of X-ray Absorption.* IEEE Trans Nucl Sci, 1991. **38**(6): p. 1721-1727.

141. P.J. La Riviere, *Approximate analytic reconstruction in x-ray fluorescence computed tomography.* Phys Med Biol, 2004. **49**(11): p. 2391-405.

142. J.M. Boone, N. Shah and T.R. Nelson, *A comprehensive analysis of DgN(CT) coefficients for pendant-geometry cone-beam breast computed tomography.* Med Phys, 2004. **31**(2): p. 226-35.

143. J.R. Taylor, *An introduction to error analysis : the study of uncertainties in physical measurements*. 1982, Mill Valley, Calif.: University Science Books., p. 40-80.

144. J.H. Hubbell and S.M. Seltzer, *Tables of X-Ray Mass Attenuation Coefficients and Mass Energy-Absorption Coefficients (version1.4).* . 2004, National Institute of Standards and Technology (NIST), Gaithersburg, MD.

145. E.B. Podgorsak, *Radiation Physics for Medical Physicists*. 2006, Springer. p. 309-312.

146. B. Lee, H. Lee and Y.G. Shin, *Fast hybrid CPU- and GPU-based CT reconstruction algorithm using air skipping technique.* J Xray Sci Technol, 2010. **18**(3): p. 221-234.

147. G. Yan, J. Tian, S. Zhu, Y. Dai and C. Qin, *Fast cone-beam CT image reconstruction using GPU hardware.* J Xray Sci Technol, 2008. **16**(4): p. 225-234.

148. A.C. Kak and M. Slaney, *Principles of Computerized Tomographic Imaging*. 1988, New York: IEEE Press., p. 49-75.

149. R. Gordon, *A tutorial on ART (Algebraic Reconstruction Techniques).* IEEE Trans Nucl Sci, 1974. **NS-21**(3): p. 78-93.

150. K. Lange and R. Carson, *EM reconstruction algorithms for emission and transmission tomography.* J Comput Assisted Tomogr, 1984. **8**(2): p. 306-16.

151. A. Taibi, G.J. Royle and R.D. Speller, *A Monte Carlo simulation study to investigate the potential of diffraction enhanced breast imaging.* IEEE Trans Nucl Sci, 2000. **47**(4): p. 1581-86.

152. K. Cranley, B.J. Gilmore, G.W.A. Fogarty and L. Desponds, *Catalogue of Diagnostic X-ray Spectra and Other Data*, The Institue of Physics and Engineering in Medicine, 1997, York, UK.

153. P.M. Shikhaliev, *Computed tomography with energy-resolved detection: a feasibility study.* Phys Med Biol, 2008. **53**(5): p. 1475-95.

154. UWCEM, *University of Wisconsin Computational Electromagnetics, Numerical Breast Phantom Repository*. 2009. January 18, 2009, Available at: http://uwcem.ece.wisc.edu/home.htm

155. C.M. Li, W.P. Segars, G.D. Tourassi, J.M. Boone and J.T. Dobbins III, *Methodology for generating a 3D computerized breast phantom from empirical data.* Med Phys, 2009. **36**(7): p. 3122-31.

156. J.T. Bushberg, *The essential physics of medical imaging*. 2002, Philadelphia: Lippincott Williams & Wilkins. p. 262.

157. A.E. Burgess, *The Rose model, revisited.* J Opt Soc Am A Opt Image Sci Vis, 1999. **16**(3): p. 633-46.

158. D.L. Batchelar and I.A. Cunningham, *Material-specific analysis using coherent-scatter imaging.* Med Phys, 2002. **29**(8): p. 1651-60.

159. J.E. Alpuche Aviles, S. Pistorius, I.A. Elbakri, R. Gordon and B. Ahmad, *A 1st generation scatter CT algorithm for electron density breast imaging which accounts for bound incoherent, coherent and multiple scatter: A Monte Carlo study.* J Xray Sci Technol, In Press, 2011.

160. J. Hsieh, *Computed Tomography : principles, design, artifacts, and recent advances*. 2006, Bellingham, SPIE - The International Society for Optical Engineering., p. 221-30.

161. R.D. Speller and J.A. Horrocks, *A Monte Carlo study of multiple scatter effects in Compton scatter densitometry.* Med Phys, 1988. **15**(5): p. 707-12.

162. M.J. Mooney, S.S. Naga, R.D. Speller and T. Koligliatis, *Monitoring and correction of multiple scatter during clinical Compton scatter densitometry measurements.* Phys Med Biol, 1996. **41**(11): p. 2399-410.

163. M. Saito, *Quasimonochromatic x-ray computed tomography by the balanced filter method using a conventional x-ray source.* Med Phys, 2004. **31**(12): p. 3436-3443.

164. S.R. Beath and I.A. Cunningham, *Pseudomonoenergetic x-ray diffraction measurements using balanced filters for coherent-scatter computed tomography*. Med Phys, 2009. **36**(5): p. 1839-1847.

165. G. Jost, T. Mensing, S. Golfier, R. Lawaczeck, H. Pietsch, J. Hutter, L. Cibik, M. Gerlach, M. Krumrey, D. Fratzscher, V. Arkadiev, R. Wedell, M. Haschke, N. Langhoff, P. Wust and L. Ludemann, *Photoelectric-enhanced radiation therapy with quasi-monochromatic computed tomography.* Med Phys, 2009. **36**(6): p. 2107-17.

166. P.M. Joseph and R.D. Spital, *A method for correcting bone induced artifacts in computed tomography scanners.* J Comput Assist Tomogr, 1978. **2**(1): p. 100-8.

167. U. Bottigli, B. Golosio, G.L. Masala, P. Oliva, S. Stumbo, P. Delogu, M.E. Fantacci, L. Abbene, F. Fauci and G. Raso, *Comparison of two portable solid state detectors with an improved collimation and alignment device for mammographic x-ray spectroscopy.* Med Phys, 2006. **33**(9): p. 3469-77.

168. O. Alonzo-Proulx, N. Packard, J.M. Boone, A. Al-Mayah, K.K. Brock, S.Z. Shen and M.J. Yaffe, *Validation of a method for measuring the volumetric breast density from digital mammograms.* Phys Med Biol, 2010. **55**(11): p. 3027-44.

169. C. Theodorakou and M.J. Farquharson, *Human soft tissue analysis using x-ray or gamma-ray techniques.* Phys Med Biol, 2008. **53**(11): p. R111-49.